UNIVERSITÀ DEGLI STUDI DI TRIESTE

XXXII CICLO DEL DOTTORATO DI RICERCA IN

NANOTECNOLOGIE

Comprehensive characterization and effective combinatorial targeting of high-grade serous ovarian cancer by transcriptomics and biomechanical features

Settore scientifico-disciplinare: MED/08

DOTTORANDO
EROS AZZALINI

COORDINATORE
PROF. ALBERTO MORGANTE

SUPERVISORE DI TESI
PROF. SERENA BONIN

ANNO ACCADEMICO 2018/2019

TABLE OF CONTENTS

ABSTRACT

Ovarian cancer kills more than 40 000 women in Europe and more than 150 000 women globally each year. High-grade serous ovarian cancer (HGSOC) is the most common and most difficult to treat subtype of the disease. The high-grade serous tumors are highly heterogeneous, therefore, though most of the patients respond well to surgery and chemotherapy initially, more than half experience relapse.

HERCULES is a research project funded by the EU H2020 program with the target to characterize comprehensively high grade serous ovarian cancers to find novel therapeutic strategies to fight them. The aim of my PhD thesis was to validate biomarkers identified within the HERCULES project in a retrospective case study of patients affected by HGSOC, studying tumor heterogeneity and evaluating the effects of pre-analytical variables, in particular fixation, in the validation process. High grade serous ovarian cancer samples were characterized validating selected biomarkers at both RNA and protein level. Molecular analysis and in situ analysis were performed on multiple tissue biopsies in order to detect spatial heterogeneity and, moreover, biomechanical proprieties of fixed tumor tissues were measured.

Lastly, the reliability of molecular analyses on archive tissues were assessed, determining the effect of formalin and Bouin's fixation at RNA level and evaluating their impact on gene expression using different platforms.

Our results showed that detail morphological and immunophenotypical analyses, at the level of the entire tissue slide and not of TMA spots (Tissue micro array), of HGSOC tumors are paramount for the differential diagnosis as well as for both prognostication and therapy. In this view, biomechanical properties, by AFM can support the morphological findings. Among the immunohistochemical markers, Ki67 and BRCA1 have been shown their predictive value for response to first line chemotherapy and overall survival in HGSOC patients. Furthermore, neo adjuvant chemotherapy seems to have a detrimental effect on patient in our cohort.

At the RNA level, cyclin C and HLA-B biomarkers showed their prognostic value indicating longer overall survival, while AKTs isoforms have shown a different impact on patients' outcome.

Regarding the pre-analytical variables, fixation confirmed to have a deep impact on molecular analyses, especially in RNA expression. Tissues with highly fragmented RNA such those fixed in Bouin's can lead to analytical bias in both ddPCR, RT-qPCR, Nanostring and RNAscope technologies. A careful selection of samples with proper nucleic acids quality and integrity is of paramount importance before starting any molecular analysis. Also in that case, to minimize the effect of sample to sample variability a proper sample size should be used. Bouin's fixed samples because of their high level of nucleic acids fragmentation are not recommended for mRNA expression

analyses, especially for low expressed targets. Contrarily, miRNAs, giving their length, are more resistant to fixation procedures and can be used for RNA expression analyses in both formalin and Bouin's tissues after a proper method of normalization.

1 INTRODUCTION

1.1 Ovarian cancer

Despite being the 8th most common cancer among females, ovarian cancer is the 5th leading cause of cancer death among women and one of the deadliest gynecological malignancies [1]. Several advances in cancer research and clinical practice have been achieved in the last twenty years, but globally there's not been an improvement in ovarian cancer survival rate, so that almost 47% of the patients still die within five years from diagnosis [1, 2].

It is estimated that annually worldwide 295.000 women are diagnosed and 185.000 die of this disease [3]. The incidence rates have a broad geographic variation with higher values (>8 per 100.000 inhabitants) recorded in United States, Eastern and Central Europe and lower values (<3 per 100.000 inhabitants) in Africa and Asia (**Fig**.**1**). Nevertheless, recent trends have shown that geographical disparity in terms of incidence has slightly becoming less relevant compared to twenty years ago since in several countries at low incidence rate, the incidence has increased and viceversa (**Fig. 2**) [4]

.

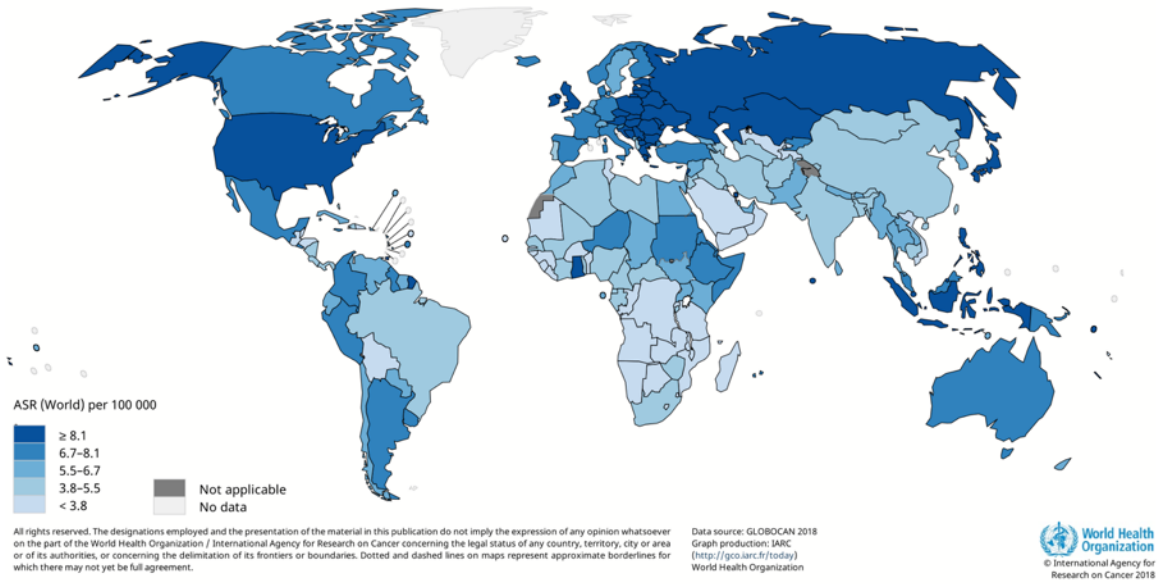

FIGURE 1. Global incidence of Ovarian cancer in 2018. ASR indicates age-standardized rates. Adapted from S.Lheureux (S.Lheureux *et al.* 2019).

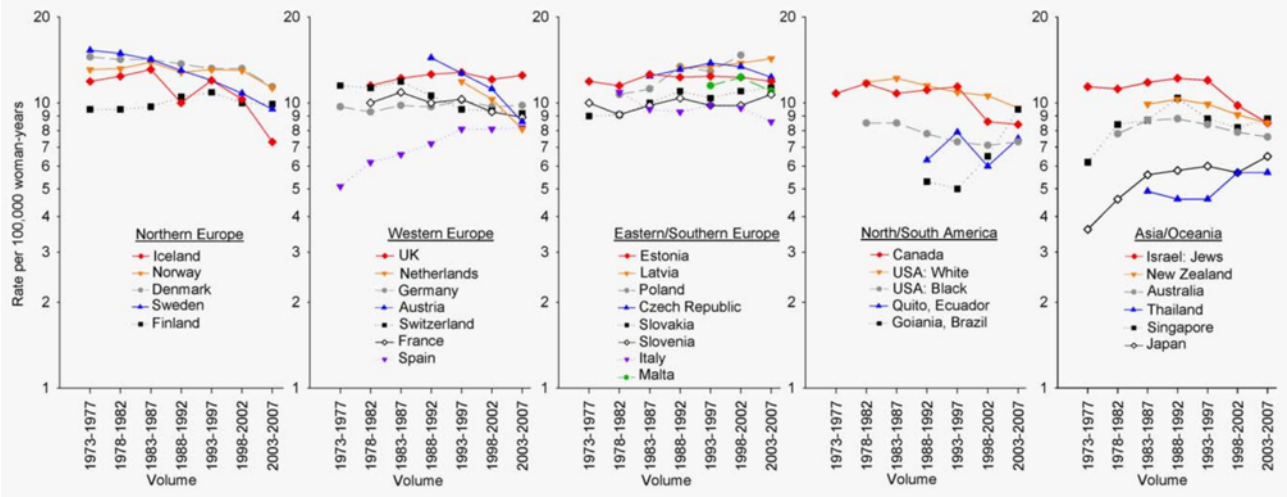

FIGURE 2. Trends in ovarian cancer age-standardized incidence rates by continent and by country from 1973-1977 to 2003-2007. Adapted from S. B. Coburn (S. B. Coburn *et al.* 2017).

The term "ovarian cancer" encompasses a wide range of neoplasms that originate in the ovaries. According to the cell of origin, the current classification divides these tumors into three groups: germ cell, sex cord–stromal and epithelial tumors, which are further divided into several subtypes based on the histology [2].

Non-epithelial ovarian tumors (germ cell and sex-cord stromal tumors) are relatively rare and they account globally for 5% of ovarian cancers. Germ cell ovarian tumors represent less than 3% of ovarian neoplasms and typically occur in young women. They origin from the oocyte and 95% of the cases appear in the form of mature cystic teratoma (dermoid cysts). Sex-cord tumors, instead, account for around 2% of ovarian neoplasms and originate from a broad range of cell types, such as granulosa cells, Leydig cells, Sertoli cells and stromal fibroblasts; nevertheless, the major part of clinical cases are granulosa cell tumors [2, 5, 6].

Almost all ovarian neoplasms (95%) are epithelial ovarian cancers (EOC). This group has been considered for a long time as a single entity, but recently several progresses in understanding ovarian cancer biology have shown that it comprises a heterogenous group of diseases with different behaviors. According to the WHO classification of 2014, epithelial ovarian cancers are divided into nine subgroups: serous (high and low grade), endometrioid, clear cell, mucinous, Brenner tumors, seromucinous, mesenchymal tumors, mixed epithelial tumors and undifferentiated carcinoma [7]. Among them the first four groups are by far the most common as five major types are frequently diagnosed in clinical practice: high grade serous carcinomas (70%), low grade serous carcinomas (<5%), endometrioid carcinomas (10%), clear cell carcinomas (10%) and mucinous carcinomas (3%). Their correct diagnosis has different implications since each subtype exhibits different histopathological, immunohistochemistry and molecular genetic profile and, more importantly, each subtype differs for the putative site of origin, the sensitivity to the current standard therapies and for

the underlying risk of hereditary cancer syndromes [8]. An overview of the morphological aspects of each EOC subtypes is depicted in **Fig. 3**, while a summary of the respective molecular features is depicted in **Fig. 4**

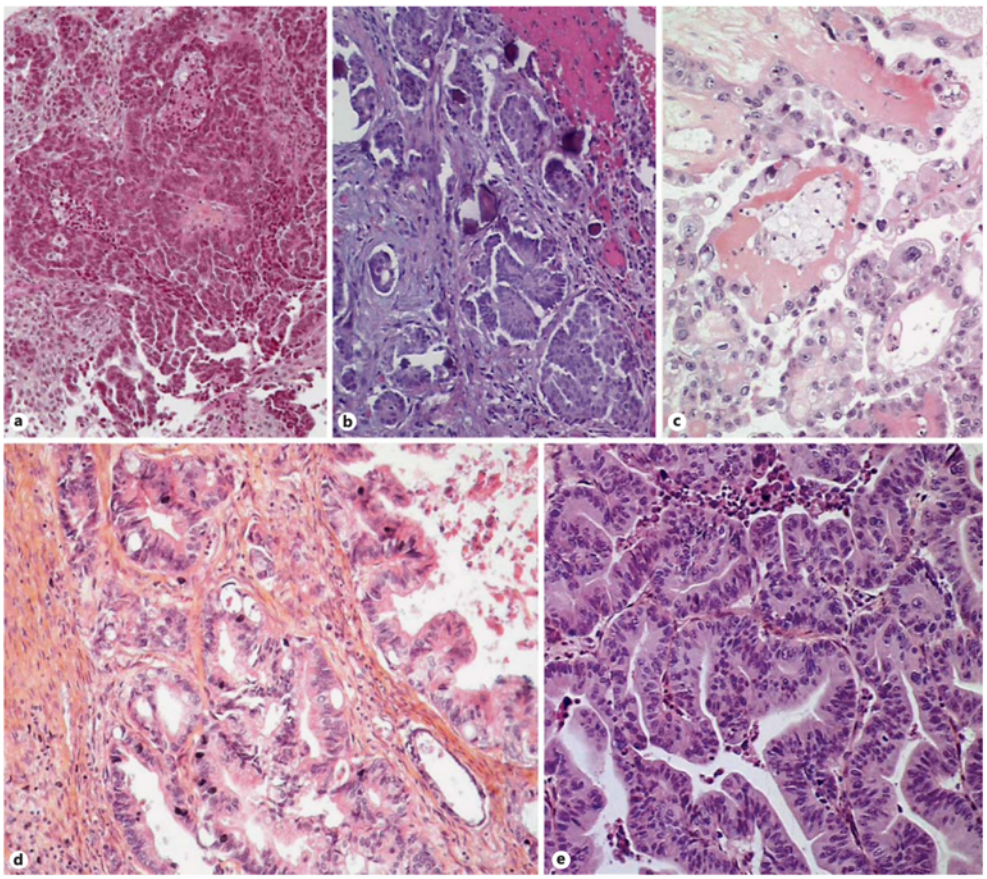

FIGURE 3. Representative histological H&E slides of the main subtypes of epithelial ovarian cancer. (A) High-grade serous carcinoma (HGSOC); (B) Low-grade serous carcinoma (LGSC); (C) Clear cell carcinoma (CC); (D) Mucinous carcinoma (MC); (E) Endometrioid carcinoma (EC). Adapted from M. Kossaï (M. Kossaï *et al.* 2016).

	Low-grade SC	High-grade SC	MC	EC	CCC
Frequency	<5%	70%	2–3%	10%	5–10%
Immunophenotype	CK7+,WT1+, ER+	CK7+, CK20, PAX8+, WT1+	CK7+, CK20–, ER–, PR–, WT1–	CK7+, PAX8+, CK20–, WT1–	napsin A+, WT1–, p53–, ER–
Precursor lesion	low-grade malignant potential lesions	STIC	borderline mucinous lesions	endometriosis	endometriosis
Molecular abnormalities	*KRAS, BRAF* [22, 23]	*TP53, BRCA1/2* [16, 17]	*KRAS, HER2* [5, 33–36]	*ARID1A, PTEN* [38]	*ARID1A, PIK3CA* [39, 51, 52]
Prognosis	intermediate	poor	good	favorable	intermediate

SC, serous carcinoma; MC, mucinous carcinoma; EC, endometrioid carcinoma; CCC, clear-cell carcinoma; STIC, serous tubal intraepithelial carcinoma; ER, estrogen receptor; PR, progesterone receptor.

FIGURE 4. Features of the five major subtypes of epithelial ovarian cancer. Adapted from M. Kossaï (M. Kossaï *et al.* 2016)

1.2 High grade serous ovarian cancer

1.2.1 Epidemiology

High grade serous carcinoma (HGSOC) is the most common type of ovarian neoplasm, accounting for 70-75% of all EOC and it's estimated that the lifetime risk for a woman of developing such disease is 1 to 70 (1,4%) [9]. Among EOC subgroups, the worldwide incident rate of high grade serous ovarian cancer is 45%, followed by mucinous carcinomas (24%), endometrioid carcinomas (13%) and clear cell carcinoma (6%). Nevertheless, the incidence rate for each subgroup in countries such as Finland, United Kingdom, Japan, Brazil and Thailand, significantly move away from those rates (**Fig. 5**) [4] .

Patients are typically diagnosed at a median age of 60 years and the median survival rate after five years from diagnosis is just of 46%. Two of the main factors contributing to this high mortality are the advanced stage at the time of diagnosis and the lack of specific symptoms, so that HGSOC has also been called "silent killer". While late stage diagnosis is relatively common (75% of the cases) and has a 5-year survival rate of just 30%, the diagnosis performed on early stage disease is much more infrequent (25% of the cases), but the 5-year survival is around 92 percent [2, 10].

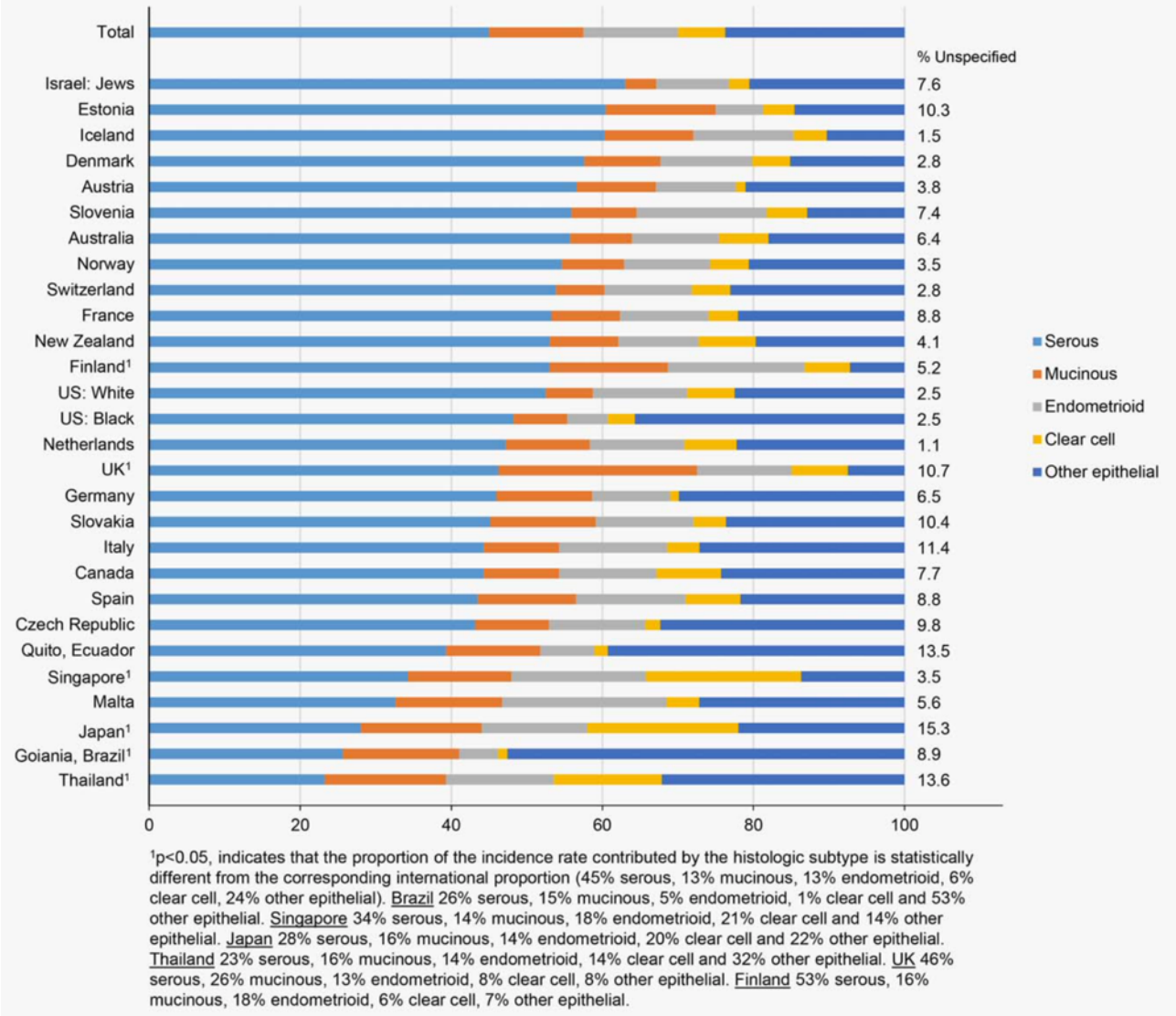

FIGURE 5. Proportion of the total epithelial ovarian cancer incidence rate by histologic subtype. Adapted from S. B. Coburn (S. B. Coburn *et al.* 2017).

1.2.2 Risk factors

A strong family history of ovarian or breast cancer is the most important risk factor, but a genomic predisposition can be identified in only 15% of affected women. Familial syndromes are mainly related to inherited mutation in BRCA1 or BRCA2 genes which are considered the putative cause of 65-75% of hereditary EOC and are mainly associated with high grade serous type [11, 12]. For this reason, a complete risk assessment should be done especially for ethnic groups, such as Ashkenazi Jews, who have a higher probability of harboring a germline BRCA1 or BRCA2 mutation [13]. In fact, women with germline mutations in these two genes are reported to have a lifetime risk of respectively 44 % and 10 % [14].

As prophylactic treatment to reduce the risk of developing HGSOC for women harboring germline BRCA1 and BRCA2 mutations, there's the possibility to undergo a bilateral salpingo-oophorectomy. Nevertheless, a persistent risk of developing a primary serous carcinoma in a peritoneal location has

been well documented in literature and this has led to several considerations regarding the effective benefit of that procedure and also regarding the controversial site of origin of HGSOCs, since the primary site usually involves the ovaries [15-17]. For patients at high risk for ovarian cancer that do not decide to undergo surgical prophylactic treatment, periodic screenings are often suggested. These include measurement of serum CA125, HE4 and p53 levels, pelvic examination and transvaginal sonography; nevertheless, several studies brought into question the efficacy of these procedures since they haven't produced a significant reduction in mortality so far [18-20]. Together with BRCA1 and BRCA2 mutations, deletion mutations in other double-strand DNA break repair genes are also associated with high grade serous ovarian cancer susceptibility [21, 22]. These genes, which are also considered for genetic testing, include CHEK2, RAD50, ATM and members of the Fanconi anemia pathway such as RAD51C, RAD51D, BRIP1, BARD1 and PALB2.

Several studies based on meta-data analyses have also identified other possible risk factors for developing high grade serous ovarian cancer, but up to now there's a lack of solid associations. These factors comprise lifetime ovulations, the use of oral contraceptives, hormone replacement therapy in post-menopausal women, smoking, obesity and use of talc powder [2, 23].

1.2.3 Clinical presentation, screening and staging

As previously mentioned, HGSOC symptoms are aspecific and they usually result in evident clinical presentation only during late stage disease. Patients may report dyspepsia, pelvic pain, abdominal bloating and shortness of breath. The latter two symptoms are usually the result of the accumulation of ascitic fluids into the abdominal cavity which causes diaphragmatic pressure, bowel obstruction and pleural effusions and are index of peritoneal carcinomatosis.

If ovarian cancer is suspected on the basis of symptoms and physical examination, computed tomography (CT) scanning or transvaginal ultrasonography are performed to evaluate the presence of pelvic masses. The finding of a solid or cystic mass is highly suggestive of ovarian cancer and CA125 blood test can further help in the diagnosis. Nevertheless, this measurement alone is nor sensitive or specific enough since elevated levels of CA125 can be associated with both benign conditions such as endometriosis, menstruation and pregnancy or other types of cancer. However, histologic confirmation is usually necessary to identify the nature of the suspected lesion and eventually identified the respective ovarian cancer histotype and staging.

Tumor staging is based on surgical assessment of the tumor at first diagnosis and is performed according to the International Federation of Gynecology and Obstetrics (FIGO) staging system that was recently revised in 2014 [24]. **Figure 6** depicts FIGO staging classification and its equivalent TNM stage of the Union for International Cancer Control (UICC).

FIGO stage	Description	Corresponding TNM stage
I	Tumour confined to ovaries or fallopian tubes	T1
IA	Tumour limited to one ovary (with ovarian capsule intact) or fallopian tube; no tumour on ovarian or fallopian tube surface; no malignant cells in the ascites or peritoneal washings	T1a
IB	Tumour limited to both ovaries (with ovarian capsules intact) or fallopian tubes; no tumour on ovarian or fallopian tube surface; no malignant cells in the ascites or peritoneal washings	T1b
IC	Tumour limited to one or both ovaries or fallopian tubes, with any of the following C substages: • IC1: surgical spill intraoperatively • IC2: capsule ruptured before surgery or tumour on ovarian or fallopian tube surface • IC3: malignant cells in the ascites or peritoneal washings	T1c
II	Tumour involves one or both ovaries, or the fallopian tubes with pelvic extension below the pelvic brim or primary peritoneal cancer (Tp)	T2
IIA	Extension and/or implants of tumour on uterus and/or fallopian tubes and/or ovaries	T2a
IIB	Extension of tumour to other pelvic intraperitoneal tissues	T2b
III	Tumour involves one or both ovaries, or the fallopian tubes, or primary peritoneal cancer with cytologically or histologically confirmed spread to the peritoneum outside the pelvis and/or metastasis to the retroperitoneal lymph nodes	T3
IIIA	Metastasis to the retroperitoneal lymph nodes with or without microscopic peritoneal involvement beyond the pelvis	T1, T2, T3aN1
	IIIA1: positive retroperitoneal lymph nodes only (pathologically proven)	
	• IIIA1(i): metastasis up to 10 mm in greatest dimension	T3a/T3aN1
	• IIIA1(ii): metastasis >10 mm in greatest dimension	
	IIIA2: microscopic extrapelvic (above the pelvic brim) peritoneal involvement with or without positive retroperitoneal lymph nodes	T3a/T3aN1
IIIB	Macroscopic peritoneal metastasis beyond the pelvis up to 2 cm in greatest dimension, with or without metastasis to the retroperitoneal lymph nodes	T3b/T3bN1
IIIC	Macroscopic peritoneal metastasis beyond the pelvis >2 cm in greatest dimension, with or without metastasis to the retroperitoneal lymph nodes (includes extension of tumour to capsule of liver and spleen without parenchymal involvement of either organ)	T3c/T3cN1
IV	Distant metastasis excluding peritoneal metastases	
	• IVA: pleural effusion with positive cytology • IVB: parenchymal metastases and metastases to extra-abdominal organs (including inguinal lymph nodes and lymph nodes outside of the abdominal cavity)	Any T, any N or M1

FIGURE 6. Staging of ovarian cancer; FIGO = Federation of Gynecology and Obstetrics; TNM = TNM classification of malignant tumor. Adapted from U. Matulonis (U. Matulonis *et al.* 2016).

1.2.4 Surgery

The primary treatment for women with newly diagnosed ovarian cancer is primary debulking surgery (PDS) whose aim is the complete macroscopic resection of cancer masses and the assessment of tumor stage. In particular, no residual tumor (R0) after PDS is one of the main prognostic factors for survival [25] . The standard surgical procedure includes a total hysterectomy and a bilateral salpingo-oophorectomy along with omentectomy, peritoneal surfaces examination and harvesting of ascitic fluids. Up to now, an additional paraaortic and pelvic lymphadenectomy was performed as well in patients with advanced disease, but one recently published clinical trial study has shown how this procedure is not associated with an improvement of the overall survival (OS) or progression free survival (PFS) [26].

After cytoreductive surgery, patients undergo a first line chemotherapy based on platinum analogs. For those patients who are too ill for sustaining the initial surgery or have a tumor burden that is too

extended for an efficient cytoreduction, a neoadjuvant chemotherapy (NACT) can be considered. This approach usually consists of three cycles of carboplatin-paclitaxel followed by an interval debulking surgery (IDS) and additional chemotherapy, for a total of six cycles. However, the use of PDS or NACT and their respective benefits is still controversial since two recent randomized clinical trials comparing the two approaches have shown similar survival [27, 28]. Moreover, only one guideline algorithm derived from the EORTC 55971 randomized trial [28] has been proposed for the selection of patients who can undergo PDS and those who can receive NACT.

1.2.5 Postoperative chemotherapy

According to tumor grade and stage, high grade serous ovarian cancer patients can be essentially divided in two subgroups. The first subgroup includes women with advanced disease (stage III and IV) or early stage disease, but at high risk of recurrence (stage I and grade 3 disease or stage II disease) for whom postoperative chemotherapy is required. The second subgroup comprises patients with early stage disease who usually have a 5-year survival rate of 90-95% after surgery. For those patients at low risk of recurrence, which essentially comprises stage 1A and 1B of grade 1 or 2, postoperative chemotherapy could be avoided.

As HGSOC is the most common among EOC, the treatment guidelines for the first line therapy of EOC have been established almost entirely on the basis of high-grade serous subtype. The standard first line chemotherapy contemplates the intravenous administration of carboplatin (75 mg/m^2) and paclitaxel (175 mg/m^2 over three hours) every three weeks for six cycles [29]. The first agent mediates its effects by crosslinking DNA strands while the second binds and stabilize tubulin polymer. Along with the standard method of chemotherapy administration, other types of administration such as intraperitoneal chemotherapy and hyper-thermic intraperitoneal chemotherapy (HIPEC) have been proposed during the past years, but several clinical trials where those methods were tested in comparison with intravenous treatment have shown discordant results [30].

In 2011, the good results of ICON7 trial [31], regarding the use of bevacizumab along with the standard first-line chemotherapy, have led to the addition of this antiangiogenetic agent in the standard of care for patients at high risk of progression. More recently, the introduction of PARP inhibitors has revolutionized HGSOC treatment, leading to a significant improvement in both OS and PFS (reference).

PARP enzymes are involved in the repair of single strand DNA breaks. Their inhibition causes the accumulation of single strand breaks that in turn determine the collapse of replication fork and the accumulation of double strand breaks in DNA. Breaks in both DNA strands are usually repaired by the homologous recombination system which is composed of different proteins including BRCA.

Ovarian cancers having mutations in BRCA1 or BRCA2 genes or in other DNA repair genes, a condition also named homologous recombination deficiency (HRD), are therefore very sensitive to PARP inhibitors because the accumulation of unrepaired DNA breaks lead to cell death [32]. Curiously, the use of PARPs has shown promising results also in patients without BRCA mutations or HDR so that those agents are now approved for women harboring germline mutations in these genes, but also as maintenance therapy for patients with tumor sensitive to first-line chemotherapy [33-35].

After first line chemotherapy patients are typically monitored with periodic physical examination, CT scanning and by measuring CA125 serum levels. In particular, the latter test is really important since an increase of CA125 biomarker is highly indicative of disease progression even in patients with asymptomatic course. A second surgery after first line treatment can be made in those patients having a disease-free interval of more than 12-24 months and in those having tumor circumscribed to one or two anatomical sites. In these women secondary cytoreduction has proven to confer several benefits [36].

Although almost 70% of patients with advance disease respond well to first line chemotherapy, only 20% never progress after it [37]. In the remaining 80% of patients the disease recurs, and after some cycles of chemotherapy followed by constant relapses, they eventually die. Recurrent disease is not curable, therefore the main goal of the second and the third line chemotherapies is to control disease, alleviate symptoms and maintain a good quality of life.

In women with recurrent disease, three groups with different prognosis and response to further treatments can be identified. The first group includes 15-20% of patients who progress during chemotherapy or within 4 weeks after the end of the treatment. This group is classified as “platinum refractory” and has a median survival shorter than 9 months. The second group comprises 20-30% of women who exhibit recurrent disease within six months after the end of chemotherapy. This group is classified as “platinum resistant” and have a median survival of about 12-18 months. The last group of patients includes those who remain free from disease for at least 6 months after first line treatment and are classified as “platinum sensitive”. For this group, a second or third line of chemotherapy with platinum derivatives in combination with paclitaxel can be attempted, while for the other two groups a non-platinum chemotherapy should be considered. Among the non-platinum agents, the most commonly used are liposomal doxorubicin, topotecan, etoposide, gemcitabine and more recently trabectedin.

1.2.6 Origin

During the past fifteen years, the site of origin of HGSOC and its evolution have been largely studied and still now they represent a matter of contention. Contrary to other types of EOC, presently a precancerous lesion for HGSOCs has not been commonly accepted by the scientific community.

Nevertheless, in the past years, two different pathogenetic theories have been firmly established. The first one states that all HGSOCs (and also other types of ovarian carcinoma) arise from the ovarian surface epithelium (OSE). According to this theory, OSE, which derives from the coelomic mesoderm, can differentiate into a Mullerian-like tissue if exposed to a chronic proinflammatory and prooxidative environment that causes alterations in DNA. The "incessant ovulation theory" proposed in 1971 [38] explains how such conditions can be achieved during normal ovulation when OSE is constantly damaged and repaired. During this process, altered OSE can invaginate and create cortical inclusion cysts (CICs) under the epithelial surface. CICs, that may contain mutated cells, exposed to ovarian growth factors can differentiate and gradually progress from metaplasia to cancer. The OSE ability of differentiating into a Mullerian phenotype can also potentially explain how cancer cells can disseminate to the mesothelium of peritoneal cavity. According to the "incessant ovulation theory", the number of ovulatory cycles is associated with the risk of developing HGSOC and therefore all factors suppressing ovulation can reduce individual risk.

The theory of an ovarian origin of HGSOCs is nevertheless losing credit nowadays in favor of a second widely accepted theory by which this type of cancer develops from the fallopian tubes [39, 40]. However, a double site of origin leading to different types of EOC through different pathogenetic processes cannot be excluded. In the last few years, the model of a fallopian tube origin of HGSOCs has gained more and more consensus also thanks to the introduction of a sampling protocol named SEE-FIM ("sectioning and extensively examining the fimbriated end") [41]. This protocol, which require the longitudinal sectioning of the distal fallopian tube at 2 mm interval, has led to an increased detection of the putative HGSOC precursors lesions, since most of them were missed before its introduction. It has been claimed that since SEE-FIM introduction, serous tubal intraepithelial carcinoma (STIC) lesions can be found in 50-60% of cases with sporadic disease and in 80% of cases with germline mutations in BRCA genes [42-44]. According to the "fallopian tubes theory", fallopian tube secretory serous epithelial cells (FTSEC) are the cells of origin of HGSOC. After genotoxic stress, a mutational event which is thought to involve p53 gene, starts the pathogenetic mechanisms that gradually lead to a precursor lesion referred to as serous tubal intraepithelial carcinoma (STIC). Cancer cells located in the fimbriated end of the fallopian tubes can then disseminate to the ovaries or directly to the peritoneal surfaces of the abdomen through exfoliation (**Fig. 7**). The sequence of carcinogenesis, starting from the normal FTSEC, involves the formation of a defined series of cell

phenotypes with different morphological and immunohistochemical features [45-47], which include different expression patterns of p53, Ki67.

It worth to mention that the classification of the precursor lesions of HGSOCs is sometimes very difficult and therefore several algorithms and guidelines have been published to help the diagnosis [48].

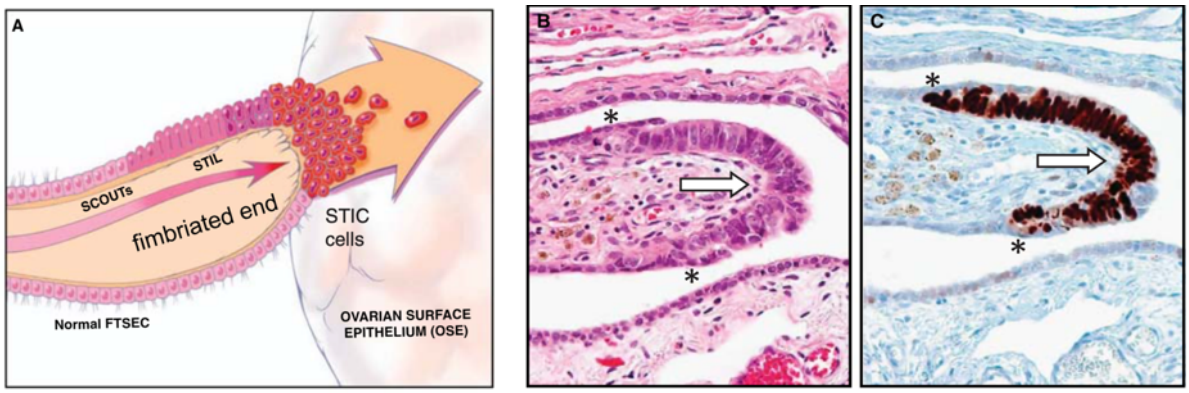

FIGURE 7. Origin of high grade serous ovarian carcinomas according to the "fallopian tubes" model. (A) Sequence of carcinogenesis leading to the formation of a serous tubal intraepithelial carcinoma (STIC) and subsequent dissemination to the ovarian surface epithelium (OSE); (B) Hematoxylin and eosin stain of a STIC; (C) Immunohistochemical staining for p53. Arrows point to STIC and asterisks define the boundaries of the lesion. Adapted from R. J. Kurman (R. J. Kurman *et al.* 2010).

At the molecular level, one model has been proposed to explain the evolution from FTSEC to STIC [49]. The primary event is the mutation of p53 gene that, although insufficient to trig the carcinogenesis, generates a special sensitivity to DNA damage. Then, the establishment of a p53 haploinsufficiency with consequent loss of function drives early molecular events in precursors lesion. Always according to this model, early p53 loss is followed by BRCA loss which in turn leads to a state of homologous recombination deficiency (HRD) with consequent chromosomal instability. Once chromosomal instability is trigged, the widespread of copy number variations (CNV) throughout the genome is the major determinant of tumor progression and its evolution (**Fig. 8**)

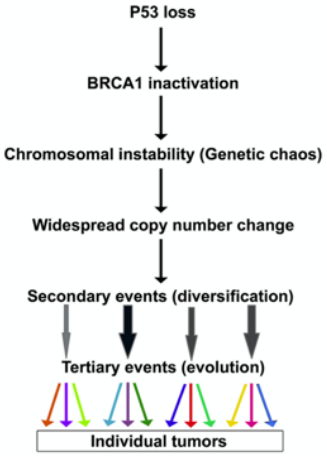

FIGURE 8. Pathogenetic model of high grade serous ovarian cancer (HGSOC). Adapted from J. Prat (J. Prat *et al.* 2018).

1.2.7 Morphological features

From a histopathological point of view, HGSOCs are highly heterogenous. They present a variety of different morphological patterns and tissue architectures. Moreover, when analyzing the hematoxylin and eosin slides at the microscope, it's quite frequent to recognize multiple morphological patterns coexisting in the same tumor specimen. At the cytological level, they usually have high grade nuclear atypia with large hyperchromic nuclei and high level of pleomorphism. Nucleoli are also large and eosinophilic. These types of tumors usually present a high mitotic index (>12 mitoses x 10 HPF) and the mitoses are frequently atypical. Moreover, it is not uncommon to see HGSOCs with multinucleate cells, giant cells and psammoma bodies, which are concentric deposits of calcium frequently associated with a papillary growth pattern [50].

As previously mentioned, high grade serous carcinoma presents a variety of architectural patterns. These patterns include solid, cribriform/pseudoendometrioid, transitional-like carcinoma, papillary, micropapillary, compressed micropapillary, infiltrative papillary and infiltrative micropapillary [51]. Recently, researches have proposed a classification of HGSOCs into two groups according to their morphological features. The first group is named "SET" and comprises tumors with solid, endometrioid-like/pseudoendometrioid and transitional patterns while the second group is named "Classic" and includes tumors with papillary and micropapillary patterns. According to the definitions proposed by Soslow and colleagues [51], solid architecture is characterized by tumor cells arranged in sheets, pseudoendometrioid by cells growing in glandular and nested pattern with punch out microlumens while transitional architecture is characterized by thick and stratified layers of tumors cells forming broad papillae usually associated with comedo necrosis. Papillary tumors instead present tumor cells arranged around a finger-like connectival axis while micropapillary

pattern are characterized by dyshesive clusters of tumor cells lacking a central vascular core and surrounded by a retraction space.

As shown in several studies, SET and classic groups can be associated to different histological components, different types of invasion patterns and to the presence or not of BRCA mutations. In particular, SET tumors have been found having higher numbers of tumor infiltrating lymphocytes (TILs), higher necrosis and higher mitotic index compared to classic tumors. Moreover, they are morphologically more homogenous throughout the tumor and are found more frequently in patients with mutations in BRCA1 gene [52]. Interesting, Howitt and colleagues have shown how SET and classic groups can be a part of a broad range of variables that could reflect a dualistic model of HGSOC pathogenesis [53] (**Fig**. **9**). In particular, histotype (SET vs classic), age, presence or not of STIC and patient outcome, allow the segregation of high grade serous ovarian cancer patients into two groups:

a) Women with BRCA mutations where the tumor has rapidly grown from a STIC or other not defined precursor lesions, leading to a clinical presentation at younger mean age. Those patients have SET features, respond well to chemotherapy and PARPs inhibitors and have a good outcome.

b) Women without BRCA mutations where tumor has slowly grown from a STIC leading to a lag phase before symptomatic metastatic disease. Those patients have classic features, older mean age, don’t respond well to chemotherapy and PARPs inhibitors and have a poor outcome.

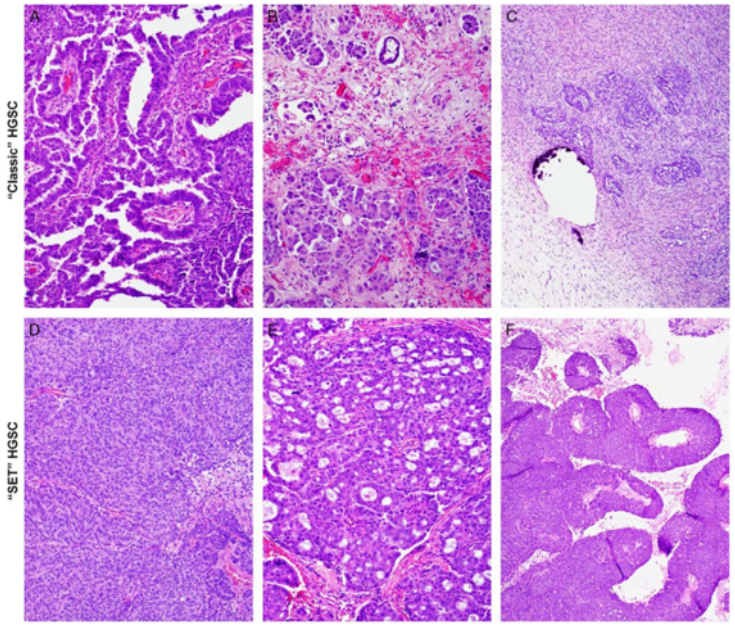

G	"SET"	Classic
Histologic pattern	Solid, endometrioid, transitional	Solid growth with slit-like glandular lumens
Age	Younger	Older
STIC	23%	67%
BRCA mutation	50%	28%
Behavior	Rapidly growing	Lag phase from STIC to symptomatic metastatic tumor
Response to chemotherapy and PARP inhibitors	More responsive	Less responsive

FIGURE 9. Histological pattern of HGSOC and their clinical features. Classic features include papillary (A), micropapillary (B) and infiltrative (C). SET features include solid (D), pseudoendometrioid/cribriform (E) and transitional (F). Summary of the dualistic model of HGSOC pathogenesis (G). Adapted from B. E. Howitt (B. E. Howitt *et al.* 2015).

1.2.8 Immunohistochemical features

As previously mentioned, epithelial ovarian cancer is not a single entity, but it's composed of five major subgroups: high grade serous carcinoma (HGSOC), low grade serous carcinoma (LGSC), endometrioid carcinoma (EC), mucinous carcinoma (MC) and clear cell carcinoma (CC). Each subgroup has its own immunophenotypical and molecular features as well as specific prognosis and therapy response. Moreover, due to the high level of morphological heterogeneity, the classical diagnosis on hematoxylin and eosin slide can be very challenging since several HGSOCs can mimic the architecture of other EOC subgroups or viceversa. It's quite challenging, for instance, to distinguish high grade serous carcinomas with endometrial-like pattern from high grade endometrial

carcinomas without an immunophenotypical charcterization. It's therefore clinically relevant correctly diagnosing EOC subgroups and being able to identify them reproducibly, especially in the case of high grade serous carcinoma since it's the most lethal type. To this regard, in the past years several biomarkers have been discovered for identifying each EOC subgroup and different algorithms based on immunohistochemistry have been proposed to help pathologists in the diagnosis. Among algorithms, the one proposed by Kobel and colleagues have found a broad consensus [54]. It is based on the use of six biomarkers that must be associated with the appropriate morphological context. These biomarkers are p53, p16, WT1 (Wilm's tumor protein), PR (progesterone receptor), HNF1β (hepatocyte nuclear factor 1 β) and ARID1A (at-rich interaction domain 1 a). According to the algorithm, following a hierarchical approach, high grade serous ovarian carcinomas are characterized by WT1 positivity (although 10% of HGSOC can be negative), aberrant p53 and diffuse or patchy p16 (CDKN2A) expression. If WT1 is negative, PR expression suggests an endometrioid carcinoma while HNF1B expression suggests a clear cell carcinoma. If both biomarkers are negative and also ARID1A is negative, the suggested diagnosis is mucinous carcinoma (**Fig.10**).

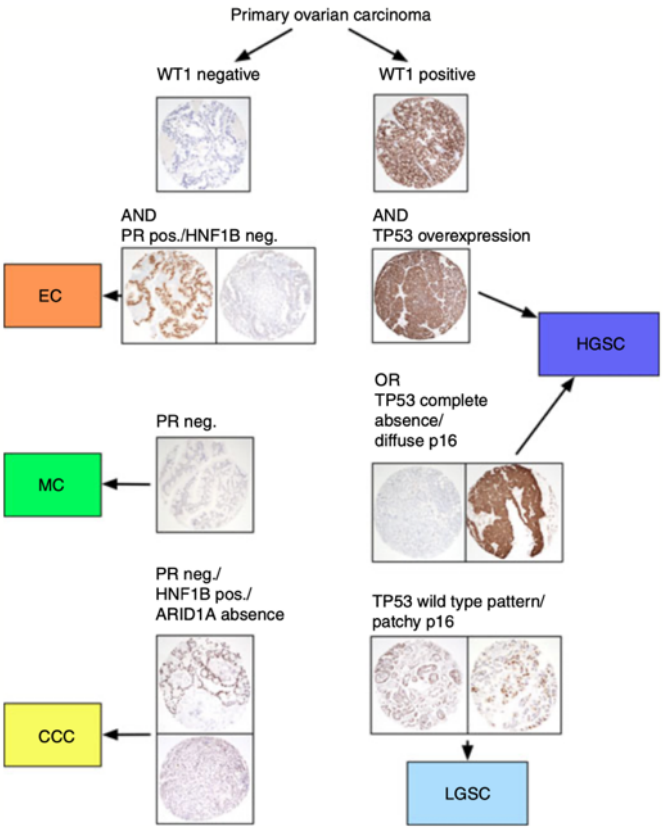

FIGURE 10. Algorithm for the interpretation of immunohistochemistry in EOC. HGSOC, high grade serous carcinoma; LGSC, low grade serous carcinoma; EC, endometrioid carcinoma; MC, mucinous carcinoma; CCC, clear cell carcinoma. Adapted from M. Kobel (M. Kobel *et al.* 2013).

1.2.9 Molecular features

The Cancer Genome Atlas (TCGA) published in 2011 the results derived from the whole genome sequencing of more than 400 HGSOC patients, providing the first global view of the genetic features of high grade serous ovarian cancers [55]. The study showed that HGSOCs are not characterized by recurrent mutations, but by a multitude of genomic structural variants, making this cancer an extreme example of chromosomally instable and aggressive disease. Structural changes, indeed, play an important role in the inactivation of oncosuppressor genes through the loss of heterozygosis (LOH), facilitating cancer progression and evolution.

The most frequent molecular alteration in HGSOC is TP53 mutation which is present in all cases and is considered one of the earliest events in the pathogenesis for its presence even in STIC lesions [56]. Besides TP53, BRCA1 and BRCA2 are the only two genes that are frequently mutated in HGSOC. BRCA1 mutations are present in about 12.5% of patients (9% germline and 3.5% somatic) while BRCA2 mutations accounts for almost 11.5% of the cases (8% germline and 3.5% somatic). In addition, around 11% of patients present also BRCA1 inactivation due to gene hypermethylation [55]. According to the genetic features, the global tendency is to divide HGSOC patients in two groups: those with a deficiency in the homologous recombination DNA repair system (HRR deficient) and those with a proficient homologous recombination system (HRR proficient) (**Fig**. **11**). The latter group accounts for about 51% of HGSOC affected women and has been associated with a better response to treatments and better outcomes compared to first one. Besides BRCA1 and BRCA2 mutations, HRR deficient group is characterized by alterations in RAD genes (RAD50, RAD51, RAD51C), CDK12, Fanconi anemia genes (PALB2, FANCA, FANCI, FANCC) and DNA damage response genes involved in the homologous recombination pathway such as ATM, ATR, CHEK1 and CHEK2 [32, 55]. In addition, other common alterations include genes that indirectly modulate HR pathway such as PTEN and EMSY, but their role in developing HR deficiency is still controversial [57, 58].

The molecular characteristics of HRR proficient group instead are relatively poorly defined, but a significant proportion of the cases, around 15%, displays amplification of CCNE1. This cyclin protein regulates the transition of cell cycle from G1 to S phase by forming a complex with cyclin dependent kinases 2 (CDK2) which constitutes a possible target for therapy. CCNE1 amplification, that has been associated with platinum therapy resistance, often coexists with strongly activation of AKT pathway, therefore the combinatorial inhibition of CDK2 and AKT is a potential target therapy for these resistant HGSOCs [59]. Intriguingly, CCNE1 amplification is also mutually exclusive with BRCA mutations and several studies have identified its alteration as an early event in carcinogenesis [60].

This suggests two possible different pathways driving the pathogenesis of HGSOC reflecting also patient's heterogeneity.

For several genes the association with HRR pathway and consequently their attribution to HRR proficient or HRR deficient subgroups is still controversial, but these genes present alterations in around 28% of HGSOC patients. The group of genes with ambiguous classification includes those belonging to the non-homologous recombination repair system, which is usually divided in two pathways, namely the non-homologous end-joining (NHEJ) and the micro-homology-mediate end-joining (MMEJ). Interestingly, CCNE1 amplification is a feature of HGSOCs that mostly exploit MMEJ system to repair DNA double strand breaks [61]. HGSOC patients with those types of tumors have usually a worse prognosis but are candidates for target therapy against polymerase θ (POLQ) since it's the main mediator of MMEJ.

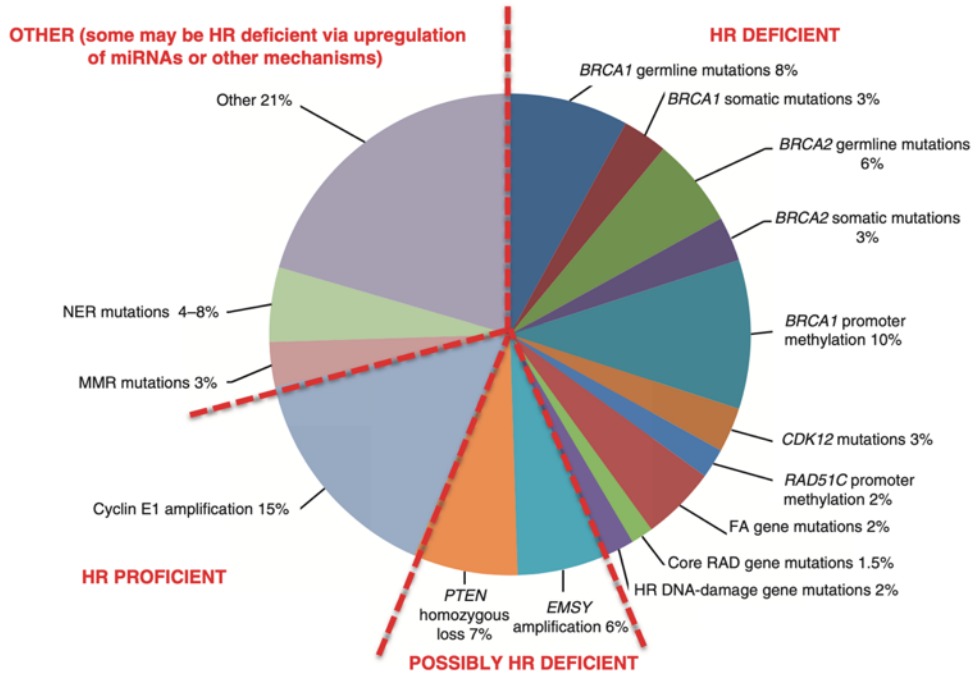

FIGURE 11. Frequency of genetic and epigenetic alterations involving HR-deficient HGSOCs or HR proficient HGSOCs. Adapted from P. A. Kostantinopoulos (P. A. Kostantinopoulos *et al.* 2015).

The TCGA study of 2011 and other subsequent studies have found alterations at genomic and transcriptomic level in several known cancer-associated pathways. Retinoblastoma (RB) pathway is altered in around 67% of the cases, mainly through CDKN2A downregulation, RB1 deletion, CCND2 upregulation and CCNE1 amplification. The second commonly altered pathway is PI3K/RAS, accounting for 45% of the cases. Alterations include deletion of PTEN and NF1 genes, KRAS mutations or amplification, amplification of PIK3CA and amplification of AKT gene. Another frequently altered pathway is NOTCH signaling, which is overactivated in 22% of cases mainly

through alterations in NOTCH3 gene. Lastly, FOXM1 and its target genes are altered in 87% of patients, but alterations include only gene overexpression and no modification by copy number changes [55].

Since HGSOC is characterized by a broad molecular heterogeneity, several groups have also tried to identify prognostic signatures or discrete molecular subgroups using clustering algorithms at both genomic and transcriptomic level. Using gene expression analyses, in 2008 Tothill and colleagues identified for the first time six classes of HGSOC samples that were correlated with different histopathological features and prognosis [62] . Later, several studies implemented and improved this classification using refined methodologies and currently five HGSOC subgroups have been identified and accepted with broad consensus. These subgroups are named mesenchymal, immunoreactive, proliferative, differentiated and anti-mesenchymal [63]. Despite their potential utility in determining patient prognosis, these gene expression signatures have not been yet implemented in clinical routine since they are technically complex and quite expensive to perform. A list of gene expression subgroups with their respective peculiar features is depicted in **Fig 12**.

Subtype	Main Features	Genes Expressed	Main Pathways	Clinical Outcome
C1/Mesenchymal (28%)	Extensive myofibroblast infiltration (desmoplasia). Mesenchymal gene expression signature	↑ COLL11A1, CXCL14, POSTN, SNAIL2, VCAN, ZEB1	Focal adhesion ECM receptor interaction JAK-STAT signaling TGF-β signaling VEGF signaling Fibroblast signature EMT/Stem cell	Negative prognosis
C2/Immunoreactive (21.5%)	Extensive intratumoral T lymphocyte infiltration	↑ CXCL10, CXCL11, PSMB8, PSMB9, TAP1	T-cell receptor signaling Toll-like receptor Antigen presentation machinery	Better prognosis
C5/Proliferative (20.5%)	Low expression of differentiation markers, limited inflammatory infiltration, activation of signaling pathways involving oncogenic and stem cell factors Lower BRCA1-2 mutation rate	↑ HMGA2, SALL2, SOX11, TCF7L1	Cell cycle NOTCH signaling	Negative prognosis
C4/Differentiated (17.5%)	Gene signature resembling serous borderline tumors	↑ COLEC11, DEFB1, ITGB4, MGLL, MLPH, STAR	Ribosome Metabolism Cytochrome p450	Intermediate prognosis
C4/Anti-mesenchymal (12.5%)	Downregulation of the genes typically upregulated in the mesenchymal subtype Lower BRCA1-2 mutation rate	↓ COLL11A1, DCN, FAP, POSTN, VCAN, ZEB1	Oxidative phosphorylation Peroxisome Butanoate metabolism	Better Prognosis

FIGURE 12. Gene expression classification of HGSOC. Adapted from U. Testa (U. Testa *et al.* 2018).

Recently, an interesting work has tried to identify ovarian cancer subgroups at the DNA level by integrating data from point mutations, copy number variations (CNV) and rearrangement features. Authors have shown how ovarian cancer histotypes can be stratified into seven subgroups according to the genomic consequence of their DNA repair [61]. In particular HGSOC can be subdivided into two signatures with different genomic alterations and prognosis: the homologous recombination deficient (HDR) signature, present in 53% patients, and the foldback inversion (FBI) signature, present in 41% patients. Accordingly, FBI dominant signature is mutually exclusive with HDR signature and it is associated with poor response to chemotherapy. At the genomic level it's characterized by few mutational events and high number of amplifications and foldback rearrangements. Importantly, this subgroup displays frequent amplification of CCNE1 and focal

deletion of PTEN. HDR signature instead is characterized by a good response to chemotherapy and alterations in BRCA genes and genes related to the homologous recombination system. Frequent alterations include amplification in MECOM, CCND1, MYC and focal deletion in RB gene.

Following those results, another group has been able to derive seven copy number signatures by performing shallow whole genome sequencing on 117 HGSOC cases [64] showing that HGSOC genomes are shaped by different mutational processes resulting in seven different patterns of genomic aberrations. Moreover, the majority of samples exhibited multiple signatures, suggesting that multiple mutational processes occur simultaneously in HGSOC patients, creating an extraordinary genomic complexity. To define each single signature, authors looked at the genome wide distribution of six fundamental copy number features and subsequently associated them with reported genomic aberrations such as breakage-fusion-bridge (BFB) cycles, chemotripsis and tandem duplication (**Fig 13**).

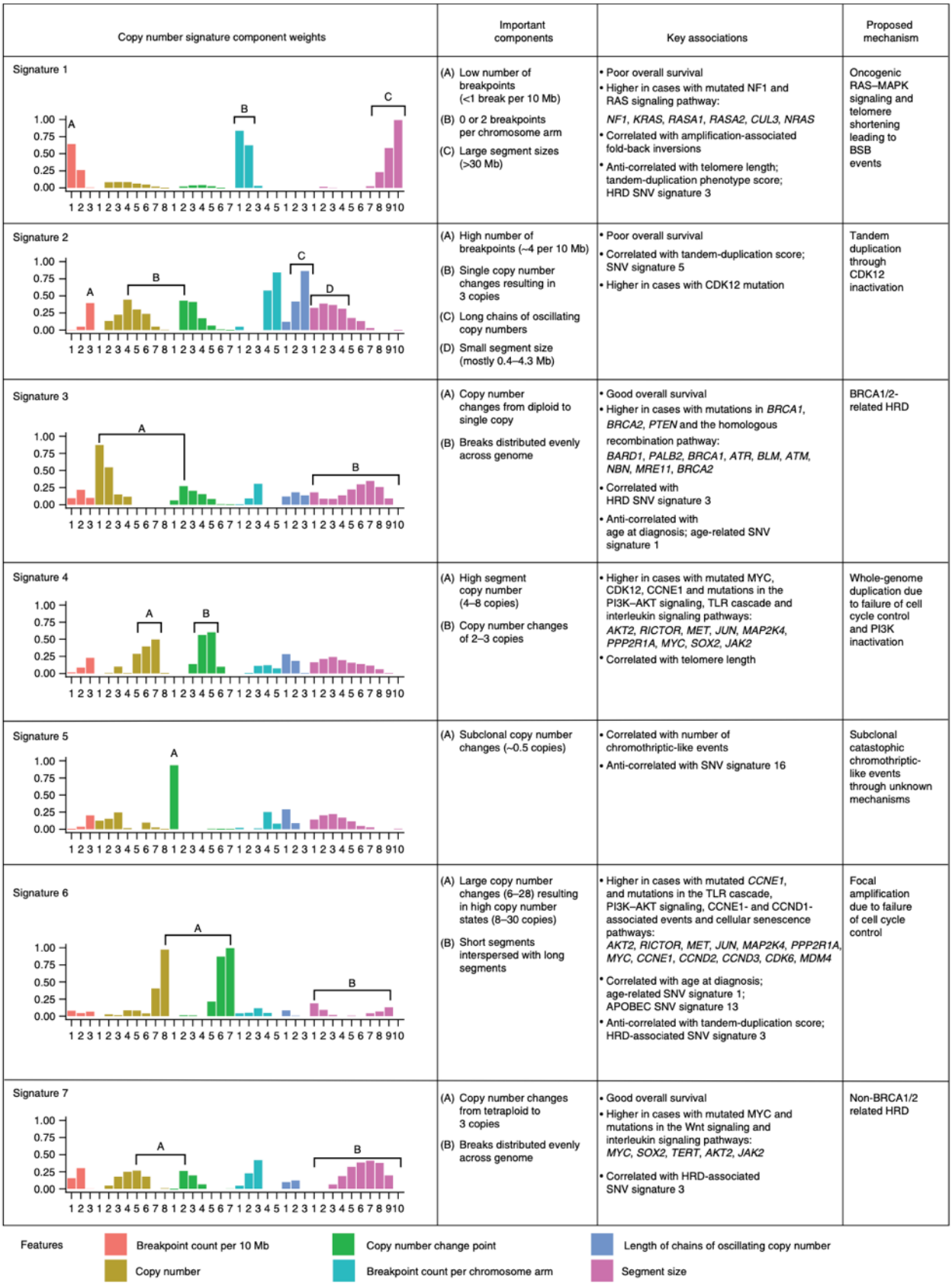

FIGURE 13. The seven copy number signatures of HGSOC. Weighted distribution and description of the six fundamental copy number features, key associations and proposed mechanism of the seven copy number signatures. Adapted from G. Macintyre (G. Macintyre *et al.* 2018).

1.2.10 Tumor heterogeneity

For almost a century, tumor diagnosis and prognosis have been made by looking at tumor morphology on H&E slides, leading to the common awareness of how histological appearance of tumors can broadly change among patients, but also within patients. The advent of molecular medicine at the end of 20th century allowed studying and classifying tumors by looking at their DNA and RNA, introducing a new level of complexity in understating how and how much tumors can variate between patients and also within individual patient. In diagnostic pathology, this complexity is commonly referred as tumor heterogeneity and is usually divided in inter-tumor heterogeneity (heterogeneity between patients) and intra-tumor heterogeneity (heterogeneity within patient). In the last decades, intratumor heterogeneity has become more and more important in oncology since it represents the basis of acquired resistance to chemotherapy and also one of the main factors leading to the irreproducibility of data in clinical research [65, 66]. Classifying intratumor heterogeneity is very challenging since it occurs at morphologic, genomic and epigenomic level both in tissues and at the single cell level. Moreover, intratumor heterogeneity occurs both at temporal (tumor evolution) and spatial level since it's dynamically shaped by changes in tumor microenvironment or by response to treatments [67, 68]. Several authors have tried to classify tumor heterogeneity [69, 70] and a proposed classification is depicted in **Fig 14**.

Microscopic tissue heterogeneity	Methods
Morphological heterogeneity	
Histology (e.g., histotype, tissue reaction, differentiation, tissue composition) Different functional areas (e.g., tumor center and borders)	Microdissection
Molecular heterogeneity	
Clonal heterogeneity Genetic evolution Epigenetic evolution	Next generation sequencing, FISH, single cell sequencing
Nonclonal heterogeneity: Phenotypic functional plasticity (autocrine/paracrine microenvironment interaction also related to different functional areas) Stochastic plasticity (single cell)	Single cell RNA sequencing, in situ methods, immunohistochemistry, proteomics

FIGURE 14. Proposed classification of tumor heterogeneity and possible methods of investigations. Adapted from G. Stanta and S. Bonin (G. Stanta and S. Bonin 2018).

Due to the high level of chromosomal instability and genomic abnormalities, HGSOC is a highly heterogenous type of cancer both at morphological and molecular level. Many studies have tried to analyze its heterogeneity reconstructing tumor evolution in different groups of patients and the resulting data have shown how mixed tumor populations have been already present at early stage

disease. As tumor evolves, it gives rise to different evolutionary trajectories, resulting in a variety of tumor cells with different genomic alterations (**Fig 15.**) [71-73]. These trajectories are highly modulated by chemotherapy so that there's a huge variability between primary and recurrent tumors, in which clonal selection still occurs [74]. Moreover, different tumor microenvironments with different proprieties co-exist within each patient and this can also account for the heterogeneity observed in the immune response, in the response to chemotherapy and in the differential progression of metastasis after treatment [75, 76]. It's therefore very important to study and identify both tumor and tumor microenvironment heterogeneities in HGSOC patients, going from tissues to single cell level and considering spatial and temporal changes.

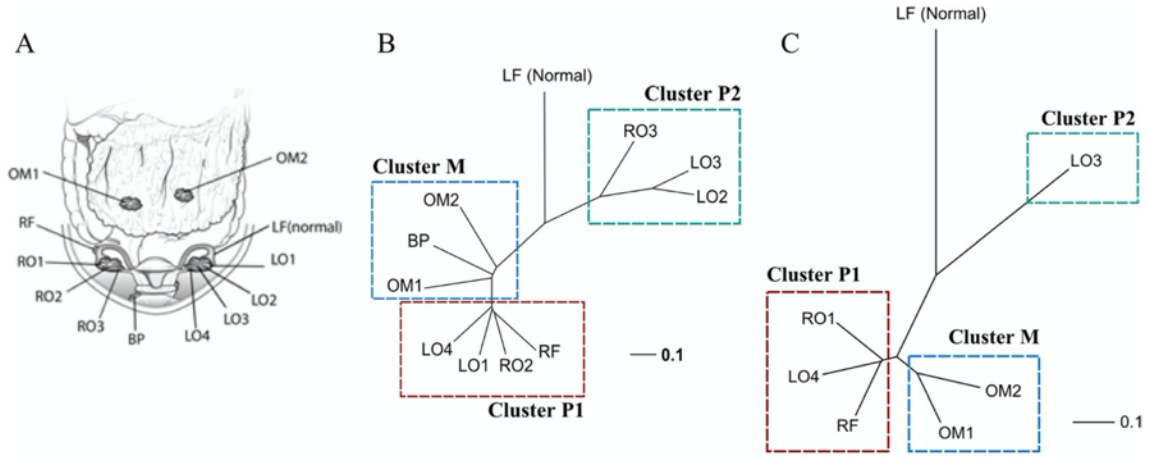

FIGURE 15. Example of intra-tumoral mutational profiles of HGSOC. (A) Sampling site of tumor and normal control tissue. (B) Phylogenetic tree of somatic mutations. (C) Phylogenetic tree of somatic copy number variations. OM = omentum, RO = right ovary, RF = right fimbriae, LO = left ovary, LF = left fimbriae, BP = bladder peritoneum. P1 = primary sites 1, P2 = primary sites 2, M = metastatic sites. Adapted from J. Y. Lee (J. Y. Lee *et al.* 2015).

1.3 The HERCULES project

In 2012 Globocan estimated there were 65.000 cases of ovarian cancer and almost 43.000 deaths for this disease in Europe [3]. Due to the lack of effective treatments, the mortality rate of the most common subtype, high grade serous carcinoma, hasn't changed during the past decades so that more than 50% of affected women still die within five years from diagnosis. Nonetheless, there's a small percentage of patients where the first line treatments are effective in eradicating the disease, resulting in a long-term survival. Several groups have tried to study the characteristics of those patients, but up to now a defined profile hasn't emerged, because factors determining outcome and response to chemotherapy are actually heterogeneous and comprise a variety of clinical and genomic features [77-79]. As previously described, the standard treatment includes cytoreductive surgery followed by chemotherapy with carboplatin and paclitaxel, and usually patients respond well to it, but soon after

they relapse and eventually die. HGSOC is highly heterogenous and composed of genetically distinct subpopulations that are dynamically generated and evolve during disease progression or after treatments [71, 72, 80]. Several of them can develop resistance against chemotherapy and being already present at the time of diagnosis, rendering the efficacy of the first line treatments very challenging. Therefore, there's an urgent need to discover new prognostic and predictive biomarkers and new treatment strategies to identify the most aggressive tumor subpopulations, eradicate them and also try to characterize those patients who have a long-term survival after therapy. For these reasons, in 2015, a European project named HERCULES ("Compre**he**nsive cha**r**acterization and effe**c**tive combinatorial targeting of high grade sero**u**s ovarian cancer via sing**le** cell analysi**s**") has been established [81]. The project, depicted in **Fig 16**, involves several participating groups and has four main goals:

- Comprehensive characterize and modelling the spatial and temporal landscape of tumor cell subpopulations during disease progression and therapy.
- Identify genetic and transcriptomic biomarkers for tumor cell subpopulations, in particular drug resistant subpopulations.
- Develop and apply integrative computational tools that are able to predict efficient combinatorial therapies able to identify and kill tumor subpopulations.
- Develop and validate a marketable prototype biomarker kit for predicting HGSOC patient response to combinatorial treatments based on formalin fixed and paraffin embedded (FFPE) sample from a tumor.

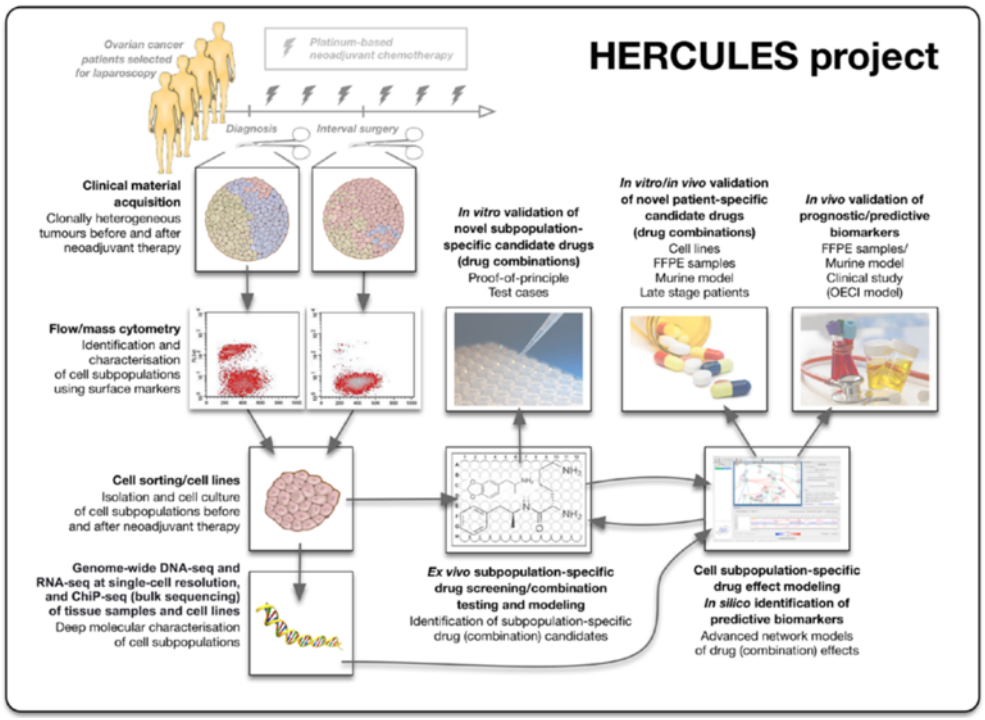

FIGURE 16. Overview of the HERCULES project

In order to achieve these goals, the project has been divided into six working packages (WP), each one with specific objectives:

- *WP1*: clinical material acquirement, management, processing and shipping
- *WP2*: identification of subpopulations in HGSOC tumors
- *WP3*: single cell capture and sequencing of HGSOC cell subpopulations
- *WP4*: deep sequencing data and network analysis
- *WP5*: ex vivo drug testing and response modelling
- *WP6*: in vitro, in vivo and clinical validation

As partner of the HERCULES project, our group is involved in WP6. In particular, our goal is to validate in a retrospective cohort of HGSOC archive tissue samples the candidate biomarkers emerged in the project, determining their sensitivity and specificity. Lastly, our results will be compared with those of a Scandinavian cohort of study in order to detect potential differences at population level, since Finland and other North European countries exhibit a higher incidence of HGSOC compared to Southern Europe.

1.4 Pre-analytical factors affecting fixed and paraffin embedded samples molecular analysis

Fixation is a fundamental step in pathology since it prevents tissue degradation and autolysis that naturally occur after tissue excision. After fixation, tissues are usually embedded in paraffin blocks in order to be cut for diagnostic purposes and/or research and then conserved. Over a century, several fixatives with different chemical compositions and different mechanisms of fixation have been produced (**Fig. 17**). Some of them, such as formalin and Bouin's solution (BS), have been routinely used in hospitals and surgical settings [82, 83]. As a result, a huge amount of fixed and paraffin embedded tissues have been collected in hospital archives and repositories all over the world. Most of them are formalin fixed, but in the early past also Bouin's solution was used. Those types of tissues represent an incredible resource, especially for cancer research, since they comprise a variety of cancers of different type and stage.

Fixative	Method of fixation	Contents
B5	Denaturing	5.4% Mercuric Chloride (w/v), 1.1% Sodium Acetate (w/v), 4% Formaldehyde (v/v), Water
Bouin's	Denaturing, cross-linking	25% of 37% formaldehyde solution, 70% picric acid, 5% acetic acid
Carnoy's	Denaturing	60% ethanol, 30% chloroform, 10% Glacial acetic acid
Glutaraldehyde	Cross-linking	Generally, 2% v/v of glutaraldehyde to water/PBS
Methacarn	Denaturing	60% methanol, 30% chloroform, 10% Glacial acetic acid
Neutral buffered formalin (NBF)	Cross-linking	10% of 37% formaldehyde solution, in a neutral pH
Paraformaldehyde (PFA)	Cross-linking	Generally, 4% w/v of paraformaldehyde to Water/PBS
Zenker's	Denaturing	5% Mercuric Chloride (w/v), 2.5% Potassium Dichromate (w/v), 5% Glacial acetic acid (v/v), Water

FIGURE 17. Fixatives used in pathology. Adapted from W. J. Howat (W. J. Howat and B. A. Wilson 2014).

Many studies have already shown that archive tissues can be used for immunophenotypical and molecular analyses [84-87], however, several variables can affect the preservation of proteins, DNA and RNA in each single tissue block, including the fixative. These variables are part of the so called "pre-analytical conditions" that include three main steps: surgery and tissue transport, tissue processing in the surgical pathology unit and tissue storage [88] (**Fig. 18**).

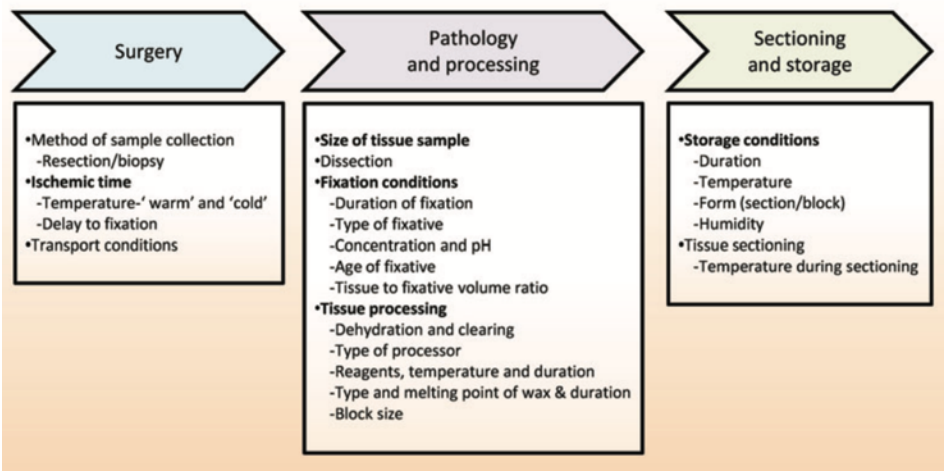

FIGURE 18. Pre-analytical factors during surgery pathology and processing and section and storage that may affect analyses in fixed and paraffin embedded tissues. Adapted from S. M. Thompson (S. M. Thompson *et al.* 2013).

During surgery, blood vessels are clamped and the decrease of blood supply results in tissue ischemia, hypoxia and alteration of cellular processes, such as RNA expression, protein degradation and metabolism. The time by which tissue remains at body temperature after blood supply interruption is called "Warm ischemia" and it is the first variable that alters and limits following tissue analyses. After surgical excision, tissue is usually chilled on ice or at room temperature and then fixed in the operating theatre or transported to the surgical pathology laboratory and then fixed. The time between the tissue body removal to fixation is referred as "Cold ischemia" and it is another source of variables in the analyses. Pre-analytical variables to take into consideration in this step are essentially transport conditions, including temperature and the duration of transport that can further exacerbate the alterations already established during surgery.

Following transport, tissue reaches the pathology laboratory for grossing, fixation and paraffin embedding. Fixation is one of the major variables affecting tissue analyses and during this process several factors such as the size of biospecimens, pH and composition of the fixative, temperature and duration of fixation must be carefully taken into consideration to prevent deterioration of biomolecules. Although fixatives such as Bouin's solution and formalin preserve tissue morphology, they alter nucleic acids and proteins due to the intrinsic action of the fixative components. In particular, the presence in both fixatives of formaldehyde induces to a variable extent the crosslinking between nucleic acids and proteins and also their chemical modification. One consequence at the protein level is, for example, the modification of antigens and their epitopes which in turn affects immunohistochemical (IHC) detection requiring to unmask epitopes and restore antigenicity [88-90]. With regard to nucleic acids, the effects of fixatives are even worse when considering molecular analyses. Both DNA and RNA are degraded in Bouin's and formalin fixed samples. Furthermore they are also chemically modified by the addition of mono-methylol groups to the nitrogenous bases,

especially adenine [91-93]. As a result, nucleic acids extraction and analyses are challenging in fixed and paraffin embedded tissues, leading also to a difficult reproducibility of the results.

After processing, fixed and embedded tissues can be stored as bulk tissue block, cut sections or as cores in tissue microarray (TMA) blocks. Samples may be stored for long periods, but particular care must be taken about the storage conditions. Several studies have shown that storage at room temperature can result in a gradual degradation of nucleic acids and, partially of proteins, while storage at 4°C or even lower temperatures can result in higher nucleic acids preservation [94]. Residual water from incomplete tissue processing or storage humidity has been reported as the possible cause of loss of antigenicity [87].

As previously mentioned, the huge amounts of variables affecting tissue during the pre-analytical phase limits the availability of biomolecules for the following immunophenotypical and molecular analyses. As a consequence, the results obtained in laboratory can be strictly dependent by sample, reference material, reagents and protocol used to perform the analysis. In the past decades, the lack of a proper standardization procedure as well as internal and external quality control have led to the problem of irreproducibility of the results in clinical research, especially with fixed and embedded biospecimens, also giving rise to a public concern regarding biomedical science publications [95]. Therefore, when performing a study, it is important to consider the influence of pre-analytical variables and determine their possible effects on samples for a correct interpretation of the results, especially for molecular analyses.

2 AIM OF THE STUDY

Within the HERCULES project, biomarkers characteristic of different HGSOC subpopulations will be identified in order to dissect tumor heterogeneity, accurately stratify patients and discover efficient therapeutic approaches. The aim of this thesis is to validate those biomarkers in a retrospective case study of patients affected by HGSOC, studying tumor heterogeneity and evaluating the effects of pre-analytical variables, in particular fixation, on the validation process. To achieve these goals and characterize HGSOC at high resolution level, several nanotools were used, going from tissue to single cell analysis. High grade serous ovarian cancer samples were characterized validating selected biomarkers at both RNA and protein level. Molecular analysis and in situ analysis were performed on multiple tissue biopsies in order to detect spatial heterogeneity and, moreover, biomechanical proprieties of fixed tumor tissues were measured.

Lastly, the reliability of molecular analyses on archive tissues were assessed, determining the effect of formalin and Bouin's fixation at RNA level and evaluating their impact on gene expression using different platforms.

3 MATERIALS AND METHODS

3.1 Patients and samples collection

Samples were collected at the National Cancer Institute of Aviano (C. R. O). All patients gave informed consent before enrollment in the study and the approval from the hospital's institutional review board was obtained to allow the use of patient's samples. The criteria for patient's selection were: i) women who had a stage IIIC or IV high grade serous ovarian cancer, ii) partial or complete follow-up information available. In total, 302 patients who underwent cytoreductive surgery between December 1998 and April 2017 were enrolled. Patients without tissue block availability, but with hematoxylin and eosin (H&E) slides available for morphologic analyses were enrolled as well. In order to assess intratumor heterogeneity, samples from different anatomical sites were collected if available. Sites included left and right ovaries, lymph nodes and peritoneal implants. Clinical information such as surgical intervention, tumor stage, TNM classification, hematologic parameters, treatment modalities, patient's status and outcome were obtained from medical records.

Since our cohort of study was composed of paraffin blocks with tissues fixed in both formalin and Bouin's solution (BS), for the validation of the biomarkers identified within the HERCULES project only FFPE tissues were considered, while for studying the reliability of molecular analyses on archive tissues, 30 matched samples fixed in formalin and BS were selected from the cohort.

The case study comprised 301 patients with HGSOC who underwent surgery at National Cancer Institute of Aviano between December 1998 and April 2017. Among them, seven patients were excluded after histological and immunophenotypical revision as they were not HGSOC. A summary of the clinicopathological features of the cohort is reported in **Table 6**. The median age of the 294 patients included in the study was 59 years (range, 30–82 years). All patients had advanced-stage disease; 63% had FIGO stage III, 25% stage IV, while in 12% of the cases information were missing. The primary treatment for almost 70% of the enrolled women was primary debulking surgery (PDS) while 25% received neoadjuvant chemotherapy (NACT) prior to cytoreduction procedure. For twenty-one patients, information was not available. Optimal cytoreduction was achieved in 28% of the patients. First line treatment was performed using multiple chemotherapy agents in 186 women, with single agent in 44; for 64 women data were not available. After first line chemotherapy, 37 patients (13%) never progressed, 102 (35%) were sensitive to treatment while 80 (27%) were resistant. Data were missing in 26% of the cases. Ultimately, 188 patients (64 %) experienced recurrence during follow-up.

TABLE 6. Clinicopathologic Features of Patients of This Study

	N = 294, n (%), Mean
Age at diagnosis	59
FIGO stage	
IIIC	185 (63)
IV	73 (25)
NA's	36 (12)
Second surgery	
Yes	49 (17)
No	193 (66)
NA's	51 (17)
Survival	
Dead	191(65)
Alive	70 (24)
NA's	33 (11)
Progression after primary therapy	
Yes	188 (64)
No	34 (12)
NA's	72 (24)
Surgical strategy	
PDS	200 (68)
NACT	73 (25)
NA's	21 (7)
Primary platinum response	
Never progressed	37 (13)
Sensitive	102 (35)
Resistant	80 (27)
NA's	75 (25)
Residual tumor after surgery	
Yes	169 (57)
No	81 (28)
NA's	44 (15)
Lymphocytes to monocytes ratios	4,16
Neutrophils to monocytes ratios	3.02
First line agents	
Single	44 (15)
Multiple	186 (63)
NA's	64 (22)
Bevacizumab	
Yes	25 (8)
No	202 (69)
NA's	67 (23)
BMI categories	
Normal	134 (46)
Obese	16 (5)
Overweight	43 (15)
Underweight	18 (6)
NA's	81 (28)

* NA's indicates not available data, PDS primary debulking surgery, NACT neoadjuvant chemotherapy

3.2 Histological revision

Hematoxylin and eosin slides of 2.5 μm-thickness were stained according to the Institute's standard processing protocol. Histological revision was performed to confirm HGSOC diagnosis and tumor grade. Where possible, slides with the highest tumor purity where chosen and the respective tissue blocks where retrieved from Institute's archives.

3.3 Microdissection

Samples with an amount of perilesional tissue higher than 20% of the total tissue area were manually microdissected to isolate the lesion. The areas of interest were visually assessed on H&E slides and then mechanically microdissected on the respective paraffin block.

3.4 Tissue microarray (TMA)

Tissue microarrays were constructed in order to perform RNAscope®/BaseScope® and AFM analyses, using FFPE tissue blocks of the peritoneal implants present in our cohort. For each block, one to three representative spots of the lesion were taken, using as reference the respective spots marked on H&E slides. Tissue cores of 1.2 mm diameter were taken from the selected spots of the donor paraffin blocks and punched into a recipient block using an Arraymold tissue Microarrayer (Riverton, Utah, USA). In total, 5 tissue microarrays of 65 spots taken from 86 patients were built. Once prepared, TMA was placed upside-down into a glass slide at 40°C overnight to allow incorporation of tissue cores into the paraffin block. After cooling, 4 μm thick sections were cut and mounted on Superfrost® Plus (Thermo Scientific) or TOMO® (Matsunami Glass, USA) microscope slides and heated at 60° C 1 hour.

3.5 Morphological analysis

Morphological analyses were performed on H&E slides derived from both formalin and Bouin's fixed tissues. The following histological features were recorded in the cases examined: (1) pattern of tumor infiltrating lymphocyte (TILs), namely if TILs were present in both tumor epithelium and stroma (ES) or just in the stroma (S); (2) number of TILs; (3) presence of vascular invasion (4); presence of necrosis; (5) number of mitoses x 10 HPF; (6) presence of psammoma bodies; (7) presence of giant cells and typical mitoses (when their amount was such to be reported). Detailed histomorphologic review was performed on all available H&E slides for each case, considering lesions from ovaries, peritoneal implants and lymph nodes (mean number of slides per case 3).

Tumors were classified as previously described [51] in two groups:

- Classic predominant HGSOC histology: < 40% of the tumor demonstrates papillary, micropapillary, or infiltrative architecture.
- Solid, endometrioid, or transitional patterns ('SET') predominant HGSOC histology: > 40% of the tumor displays one or more variant features, including solid growth, pseudo-gland formation, and transitional cell-like patterns.

Tumors with ambiguous HGSOC morphology where revaluated considering IHC analysis, using the biomarker panel modified from Kobel *et al* described in this thesis; tumors presenting also ambiguous IHC biomarkers expression were discarded. TILs pattern and number of TILs were assessed in selected areas, at 20X magnification, after scanning all slide. Vascular invasion and necrosis were measured using a four-level score from 0 (absence) to 3. The percentage of each tumor containing SET vs classic histology was estimated in each case in increment of 10%. When more than one SET pattern was identified, the percentage values were added together. For example, if a tumor showed 20% solid architecture, 10% pseudoendometrioid architecture and 70% papillary architecture, the SET value was 30% and the case was coded as Classic. In order to correlated SET percentage with clinicopathological features, in patients having multiple slides derived from different anatomical sites, the mean SET percentage was calculated.

3.6 Immunohistochemical (IHC) analysis

To achieve intra-tumor heterogeneity, the IHC staining was performed on the entire tissue section of 2.5 μm of thickness, using a panel of seven biomarkers modified from Kobel et al. and selected within the HERCULES project [54]. The antibodies used, along with the corresponding experimental conditions are reported in **Table 1**. The immunostaining procedures were performed with the automated XT iVIEW DAB V.1 protocol on the BenchMark ULTRA IHC/ISH Staining Module, Ventana. Stainings were detected using the I-View DAB detection system.

TABLE 1. Antibodies used for IHC analysis. WT1 = Wilm's tumor protein 1; PR = Progesterone receptor; HNF1β = Hepatocyte nuclear factor 1- β

Antibody	clone	localization	incubation
p53	DO-7 Ventana	nuclear	16 min 37° C
p16	E6H4 Ventana	nuclear/citoplasm	16 min 36° C
WT1	6F-H2 Ventana	nuclear	40 min 37° C
Ki67	30-9 Ventana	nuclear	16 min 37° C
PR	1E2 Ventana	nuclear	16 min 36° C
HNF1β	HPA002083- Sigma	nuclear	32 min RT

BRCA1	MS110 Abcam	nuclear/citoplasm	36 min RT

Immunostaining was evaluated using standard light microscopy by two expert pathologists. Semi-quantitative evaluation of each antibody staining was performed using a three-levels score of signal intensity (+, ++, +++) and by assessing the percentage of immunoreactive tumor cells in one HPF over the total number of tumor cells visualized. In determining tumor cells positivity and signal intensity, both nuclear and cytoplasmatic staining were considered. An average estimation of the number of positive cells for each intensity level was then performed considering several HPFs at 40X magnification. Immunoreactivity was evaluated by use of the H-score method (3 x % of cells with (+++) intensity + 2 x % of cells with (++) intensity + % cells with (+) intensity) in both nuclear and cytoplasmatic compartments, giving a range of 0-300 [96]. Moreover, the staining pattern of each biomarker was evaluated and classified as homogenous, heterogeneous, negative or stochastic by using scoring cut-offs and visual estimation (**Table 2**).

TABLE 2. Antibodies scoring cut-offs.

	Homogenous	**Heterogenous**	**Negative**	**Stochasthic**	**Positivity**
p53	% positive cells > 80	0 > % positive cells < 80	% positive cells = 0	/	>1% any intensity
p16	% positive cells > 80	0 > % positive cells < 80	% positive cells = 0	/	>1% any intensity
WT1	% positive cells > 80	0 > % positive cells < 80	% positive cells = 0	/	>1% any intensity
Ki67	/	/	% positive cells = 0	% positive cells > 0%	>5% any intensity
PR	% positive cells > 80	10 > % positive cells < 80	% positive cells = 0	0 >% positive cells< 10	>5% any intensity
HNF1β	% positive cells > 80	10 > % positive cells < 80	% positive cells = 0	0 >% positive cells< 10	>5% any intensity
BRCA1	% positive cells > 80	10 > % positive cells < 80	% positive cells = 0	0 >% positive cells< 10	>5% any intensity

The H-score and staining pattern of each biomarker were compared between the two ovaries and between the two ovaries and the peritoneal implants to look for possible anatomy-related differences in protein expression. Cases with different staining pattern between the two anatomical sites were defined “discordant” otherwise “concordant”. The relationship between clinico-morphological parameters and H-score or staining pattern was evaluated for each biomarker, considering each anatomical site separately. In addition, for samples having multiple tissue biopsies, a further analysis

was performed calculating the average H-score along with the average value of each morphological feature having a continuous distribution and then correlating them.

3.7 Molecular analyses at RNA level - validation of HERCULES biomarkers

3.7.1 Nanostring®

In 2008 Geiss and colleagues developed a new gene expression technology, named Nanostring nCounter®, that significantly improved the ability of performing RNA studies in terms of sensitivity and multiplexing. Since then, lots of studies have successfully applied this system to investigate on RNA expression in different biological samples including fresh tissues, blood, urine and also fixed and paraffin embedded tissue [97-102]. Thanks to its high multiplexing capability Nanostring nCounter® has proven to be a valuable tool in cancer research to identify gene expression signatures, so that it has been introduced in clinical setting as a complementary instrument for the diagnosis and prognosis of different types of cancers [102, 103].

Nanostring® chemistry is based on a solution-phase hybridization reaction where target RNAs are captured by a complementary nucleic acids probe. Each probe has barcode with a unique combination of different fluorophores that are used to identify target RNAs. Globally, the workflow consists of three steps:

- Hybridization: a population of RNAs is mixed with capture and reporter probes in solution, forming a tripartite complex during hybridization. The reporter probe is composed by a unique labeled barcode, specific for each RNA, while the capture probe allows bounding of hybridized complexes to a cartridge surface.
- Purification and immobilization: after hybridization, tripartite complexes are bound and immobilized to the cartridge surface of a flow cell covered with biotin.
- Counting and analysis: a digital Analyzer instrument images up to 600 fields of view (FOV) per flow cell. Following, images are processed, and each barcode is selected according to several inclusion criteria; in particular, each fluorophore spot must have a length of around 300 nm, the spot-to-spot spacing must be of 200 nm and barcodes must have a proper orientation. After the selection, each single barcode is counted, returning RNA expression of up to 800 targets (**Fig 19.**)

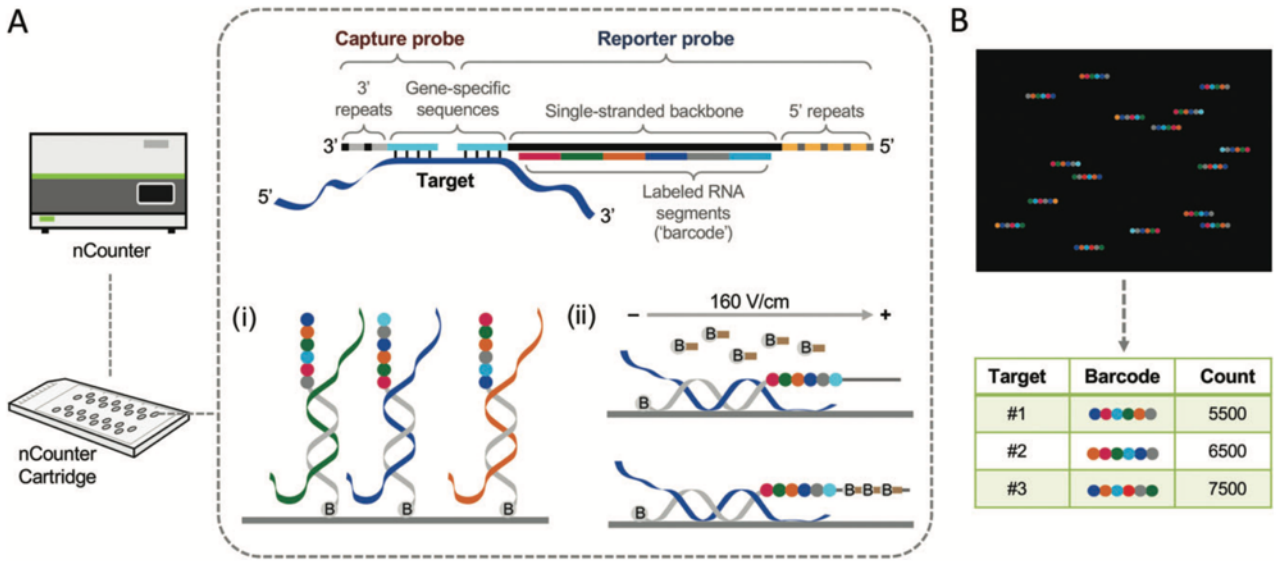

FIGURE 19. Nanostring® workflow. A) Target RNA is mixed in solution with capture and reporter probes. Capture probe is composed of a 50-base target specific sequence attached in the 3′ end to an oligonucleotide of two 15-base repeats linked with a biotin molecule. The reporter probe consists of linearized ssDNA annealed to six fluorescent labeled RNA segments (barcode). (i) During purification unbound probes are removed and target complexes are immobilized to the surface of a Nanostring cartridge. (ii) Thanks to the addition of biotin molecules, immobilized reporter probes are stretched and aligned along the bottom of the flow cell by applying 160 V/cm current. B) After immobilization, barcodes are imaged and selected according to several inclusion criteria. Selected barcodes are then counted and associated with the respective target are Adapted from J. Decalf (J. Decalf *et al.* 2019).

It's worth to mention that Nanostring® doesn't rely on the reverse transcription of RNA to cDNA, but it works with bare RNA. This is a peculiar aspect of this technology, since it avoids all the biases that can be introduced during reverse transcription, which in turn affect cDNA amplification in highly fragmented and modified samples such those from fixed and paraffin embedded tissues. Moreover, Nanostring® exhibits a high level of sensitivity that reaches 0.1-0.5 fM of target RNA rendering this system highly indicated for archive tissue samples with low abundant targets [104].

A custom nCounter® assay (Nanostring Technologies, Seattle, WA) was designed for quantitative assessment of expression of 71 gene elements. Gene elements were identified within the HERCULES project and were partially included in one published signature [105]. Along with these genes we also added AKT1, AKT2 and AKT3 isoforms to our custom assay since AKT pathway is altered in almost 45% of HGSOCs.

In order to compare our results on Nanostring® platform with those obtained from a Scandinavian group involved in the HERCULES project, 32 samples matched for number and clinical features were selected. A list with the selected features is reported in **Table 3.**

TABLE 3. Clinical characteristics of the 32 cases included in the study for cohort comparisons

Clinical characteristics	N° (%) or median
Age	60.9
Primary therapy outcome	
Complete response	15 (47%)
Partial response	7 (22%)
Progressive disease	8 (25%)
NA	2 (6%)
Residual tumor after surgery	
0 mm	7 (22%)
1-10 mm	13 (40%)
>10 mm	12 (38%)
Surgical strategy	
Primary debulking surgery (PDS)	23 (72%)
Neoadjuvant chemotherapy (NACT)	9 (28%)
FIGO STAGE	
IIIC	15 (47%)
IV	17 (53%)

Samples preparation and hybridization were carried out according to the manufacturer's instructions. Briefly, 300 ng of input RNA was hybridized to a Nanostring 48-plex Custom Probes Codeset, consisting of 71 target sequences, at 65°C for 18 hr.

The hybridization products were then processed on the nCounter® Prep Station in order to wash off unbound capture and reporter probes and immobilize the hybridized complexes on a streptavidin-coated cartridge. Barcoded signals were acquired using the nCounter® Digital Analyzer and data analyzed using the Nanostring® software, nSolver 4.0.

To correct biases generated by assay efficiency, such as hybridization, purification or binding, data were normalized to exogenous positive controls and to the internal levels of 11 housekeeping genes (ACTB, GAPDH, GUSB, HPRT1, RPL19, PPIA, TBP, B2M, HMBS, CALM2, PGK1), using the software default settings.

The hybridization background was then subtracted using the spiked-in negative controls that were below the mean background plus 2 standard deviations.

3.7.2 RNAscope®

RNA biomarkers or gene expression signatures have gained more and more importance in clinical oncology, also due to the introduction of gene expression profiling technologies in clinical settings [106]. Nevertheless, most of these techniques rely on the extraction of RNA that causes partial loss

of material and complete loss of morphology. Furthermore, these assays suffer for the interference of other cellular components or tissue elements present within or around the tumor. To this regard, several RNA in situ hybridization (ISH) techniques have been produced but they lack sensitivity, preventing the detection of low expressed transcripts [107]. RNAscope® is a novel RNA ISH method that allows the visualization of single RNA molecules in individual cells directly on fixed and paraffin embedded tissue slides. Moreover, in order to directly target and visualize specific RNA locus, a complementary RNAscope® assay named BaseScope™ is available. The system is a hybridization-based amplification of RNA signal that use a novel probe design strategy called "double-Z". A schematic summary of RNAscope® assay procedure is depicted and described in **Fig. 20.**

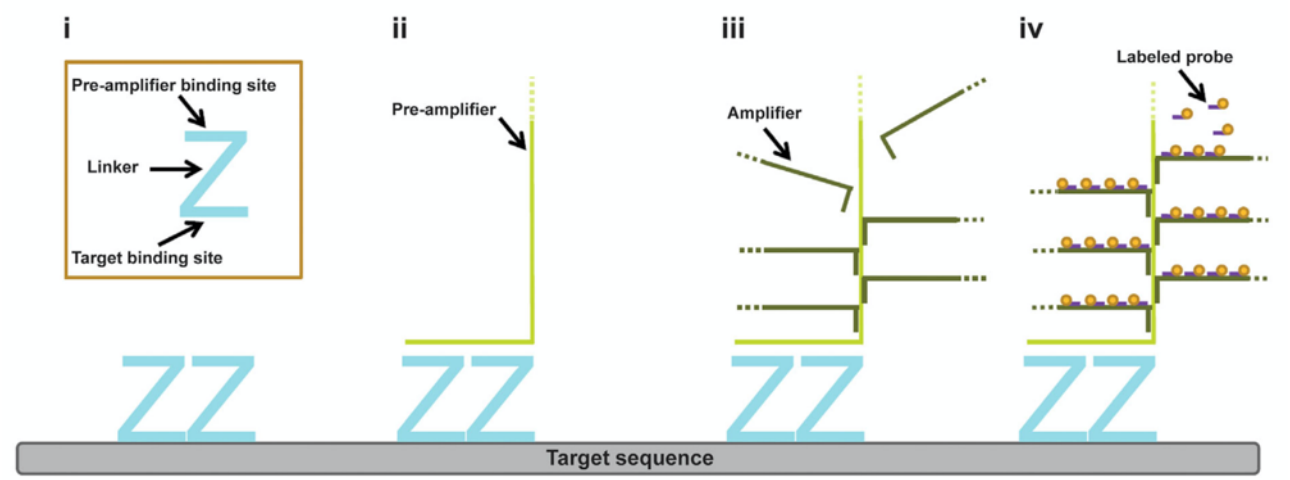

FIGURE 20. Automated RNAscope technology overview. (A) RNAscope probe design. (i) A standard target probe consists of a pool of 20 double Z probes targeting a region of 1000 bases. Each Z target probe contains three elements: the lower region is complementary to the target RNA and is selected for target specific hybridization and uniform hybridization properties; a spacer sequence links the lower region to an upper region; the two adjacent upper regions from a double Z target probe form a 28 base binding site for the pre-amplifier. (ii) Once the Z probe pairs hybridize to the RNA target the pre-amplifier binds to the upper regions of the Z probe pairs. (iii) Hybridization of multiple amplifiers per pre-amplifier. (iv) Hybridization of multiple labeled probes per amplifier. Labeled probes contain a chromogenic enzyme to generate one punctate dot per RNA target. The size of the dot is directly proportional to the number of Z probe pairs hybridized onto the RNA target. Hybridization of only three Z probe pairs is sufficient to obtain a detectable signal by brightfield microscopy. Adapted from C. M. Anderson (C. M. Anderson et al. 2016).

Within the HERCULES project, seven mRNA biomarkers of prognostic and predictive significance were retrieved by single cell sequencing analysis, performed on a series of HGSOC peritoneal implants. We then validated those biomarkers in selected FFPE peritoneal implants of our cohort of samples using RNAscope® and Basescope™ assays (Advanced Cell Diagnostics, Newark, CA) in order to detect RNA expression in a spatial context and exclude potential contribution from other cell types out of tumor cells. Tissue slices cut from TMA blocks were prepared as previously described and then submitted to RNAscope® assay.

Following the manufacturer's instructions, 4-µm sections were deparaffinized and processed with pretreatment reagents (Advanced Cell Diagnostics, Newark, CA). Tissue sections were hybridized with probes Hs-CCNC, BA-Hs-HLA-B, Hs-CCNE1, Hs-WFDC2 (Advanced Cell Diagnostics, Newark, CA) at 40 °C for 2 h. Hybridization signals were amplified and visualized with RNAscope® 2.5 HD detection kit and BaseScope™ Reagent Kit v2-RED (Advanced Cell Diagnostics, Newark, CA). Positive control probes targeting the PPIB housekeeping gene (Advanced Cell Diagnostics, Newark, CA) and negative control probes targeting the bacterial DapB gene (Advanced Cell Diagnostics, Newark, CA) were used as positive and negative controls in order to verify tissue integrity and check for unspecific stain. Data analysis was performed according to the semi-quantitative histological scoring based on manufacturer's criteria.

3.8 Atomic force microscopy

Cancer cells proliferate and differentiate in highly dynamic way. One of the main factors determining cells behaviors is their interaction with the surrounding microenvironment, the extracellular matrix (ECM). Although cancer cells can respond to chemical signals coming from the ECM, one of the main interactions between the two components is represented by the development of mechanical forces [108] . The transformation from normal cell to cancer cell is accompanied, indeed, by a progressive loss of the normal biomechanical proprieties of both cancer and stromal cells [109] . Compressive forces at tumor border can modify ECM while compressive forces within the tumor can decrease cells' proliferation, but at the same time increase also the metastatic potential of tumor clones [110]. Therefore, understanding mechanical alterations can provide information on cancer biology and subsequently on diagnosis and prognosis.

The atomic force microscopy (AFM) is a technology belonging to the family of scanning probes microscopy which allows the characterization of the biomechanical proprieties of cells and tissues [111, 112]. AFM is composed of a micrometer sized probe (a tip or a bead) mounted at the distal end of a cantilever which moves on a sample's surface across XYZ positions, thanks to piezoelectric elements. Then, a laser source emits a beam toward the cantilever which in turn is reflected to a photodiode. The photodiode, usually composed of four quadrants, records the movements of the cantilever based on laser beam deflection. The deflection of the cantilever is converted into force by multiplying it by the spring constant of the cantilever according to Hooke's law (**Fig. 21**)

AFM can operate under different conditions (vacuum, air, liquid) and in three different modes:

- *Contact mode*: the tip is in contact with sample's surface.
- *Intermitted contact mode*: the tip intermittently touches sample's surface.
- *No-contact mode*: the tip oscillates at a certain distance from the surface.

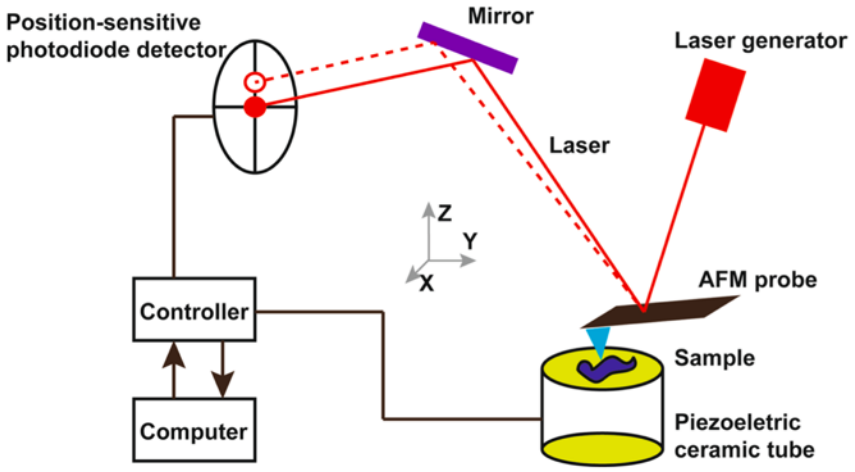

FIGURE 21. Schematic diagram of AFM working principles. Adapted from X. Deng (X. Deng *et al.* 2018).

One of the most interesting characteristic of cancer cells and tissues is their stiffness. Several studies have already shown how there's a correlation between cancer cells stiffness and their ability to induce metastasis [113]. Thus, it's of big interest to determine cancer stiffness in the context of cancer related progression. In order to measure cancer cell stiffness with AFM, a nanoindentation can be performed in specific points of the sample. Cantilever's deflection is then measured as a function of tip's *z* position. The indentation procedure provides force-indentation curves which can be used to calculate the elastic modulus (Young's modulus) of the sample by fitting them with the Hertzian model (**Fig 22.**). In general, if the slope of the curve is linear and with an angle of about 45°, this indicates a very hard sample, otherwise, if the curves is more parabolic, the sample is soft.

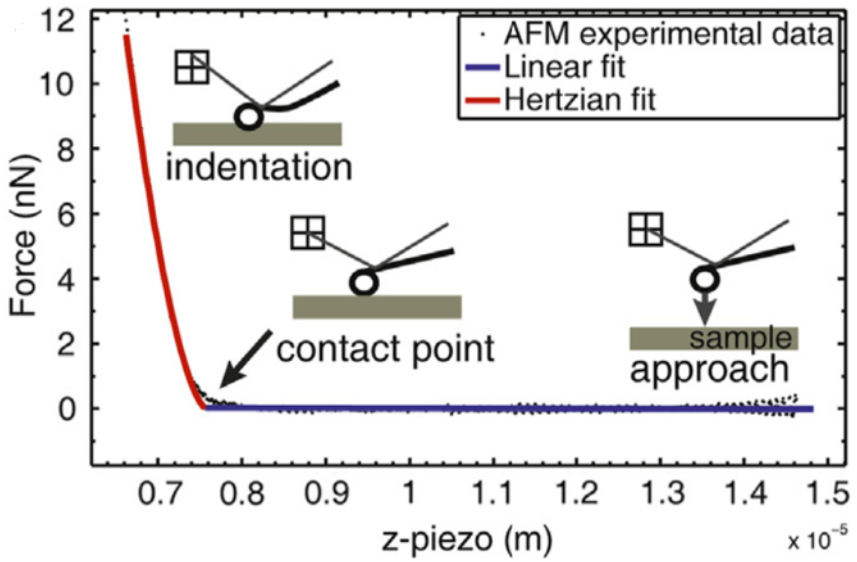

FIGURE 22. Typical AFM force-distance curve collected during sample indentation. The linear curve (blue line) is fitted to the non-contact portion of the force curve. Here the cantilever approaches the sample and there's no deflection. A non-linear curve (red line) is fitted to the indentation (i.e contact) part of the curve. The. cantilever deflection increases while the distance (z-piezo) decreases. Adapted from H. O. B. Gautier (H. O. B. Gautier *et al.* 2015).

In order to measure biomechanical proprieties of cancer cells by means of atomic force microscopy, the same TMAs blocks used for RNAscope® assay were cut and stained with H&E. In total 26 spots derived from 19 samples were measured. Samples and respective spots were chosen according to the architectural pattern described by Soslow *et al*. The architectural patterns selected for AFM analysis include papillary, micropapillary, solid, transitional and endometrioid-like. Only samples with pure morphological architecture were taken into consideration. The stiffness of tissues sections was studied evaluating the Young's modulus of the cells inside the tissue. Measurements were made directly on TMA slides in the liquid environment, using a Smena AFM (NT-MDT Co., Moscow, Russia) mounted on an inverted microscope (Nikon Eclipse Ti-U). Slide was placed in a 60-ml petri dish above the AFM stage for positioning the indentation locations during the experiments. Optical images were acquired on the inverted microscope using the software ImageJ. Following, the slide was pasted on a plate and immobilized by applying a two components fast drying glue (Reprorubber® Thin Pour). After that, petri dish was placed on the microscope stage within the plate and filled with PBS solution at room temperature (**Fig. 23**).

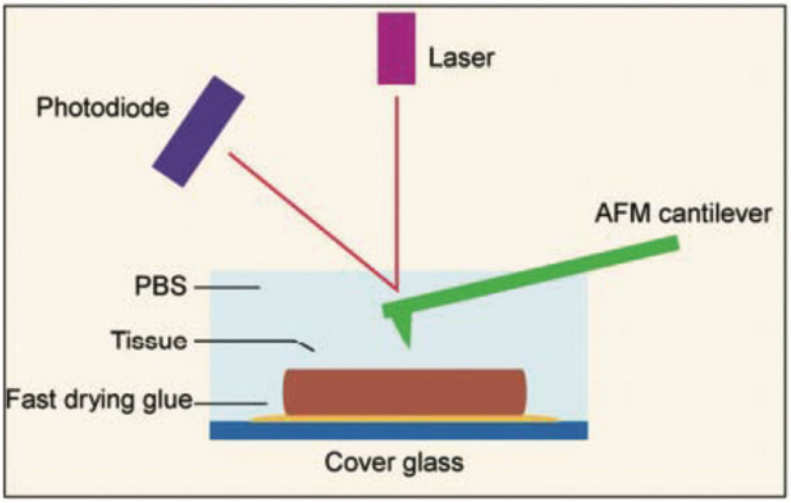

FIGURE 23. Example of AFM setup for measuring tissue biomechanical proprieties under liquid conditions. Adapted from A. Stylianou (A. Stylianou *et al.* 2018).

Mechanical characterization tests were performed using AFM cantilever (Etalon HA-NC) with normal spring constant of 3.5 N/m and a spherical bead of 20 µm diameter. In order to characterize the spring constant of the cantilever, thermo-stiffness method was used while the sensitivity was measured over the rigid surface of the glass slide at the end on each experiment to make sure that only the elasticity of the cantilever was involved. In order to perform the indentation, the cantilever was lowered in contact with the surface of the sample followed by applying an electrical current of setpoint 0.5 nA. The force–displacement curves were recorded accordingly using NOVA-Px 3.4 control and analysis software (NT- MDT Co., Moscow, Russia). In each sample's spot, one to three locations were selected, and in each location, over 40 points in a square of the dimensions of 300 x 400 μm^2 were measured. Young's modulus values, in kPa, were determined by fitting obtained force-displacement curves with an Hertzian model, taking advantage of the software AtomicJ. All steps of the experiment, from the preparation of the samples up to the measurement of the mechanical characteristics, were carried out within a few hours to prevent biochemical changes in the tissue.

3.9 Molecular analyses at RNA level – effect of fixation

One of the main pre-analytical variables affecting molecular analyses in archive tissues is fixation. As previously mentioned, our cohort of study is composed of archive tissues fixed with two different types of solutions, formalin and Bouin's solution (BS), as up to 2010 at the cancer institute of Aviano Boui's solution was the fixative used in routine. Neutral buffered formalin is the fixative of choice for archive tissues in pathology, but for special purposes or historical reasons, other fixatives such as

Bouin's solution (BS) has been used in several European countries [114]. In particular, BS has been preferred over formalin in diagnostic for its better preservation of some morphological features, especially for biopsies requiring excellent nuclear details, such as testis and lymphoma [115]. BS fixative is a mixture of formalin, picric acid and acetic acid, three components that exert a prolonged damage to tissue components, altering both nucleic acids and proteins. Formalin leads to the crosslinks between proteins themselves and between proteins and nucleic acids through the formation of methylene bridges; picric acid, instead, causes protein coagulation while acetic acid allows a faster penetration of the other two compounds within the tissue. As a consequence, nucleic acids and proteins are hardly analyzed since isolated biomolecules for molecular analysis are usually scarce and/or degraded. In the past decades, several studies have already shown that Bouin fixed samples are amenable for nucleic acids and proteins analyses, but only to a certain extent [116]. In recent years the development of new cutting-edge technologies has allowed assessing mRNA expression from archive tissues with high sensitivity and low amount of input material, overcoming several drawbacks and limitations linked to the use of fixed specimens. Moreover, in the last decade micro RNAs (miRNAs), have gained more and more importance in research and clinical settings as a new generation of prognostic and predictive biomarkers for monitoring cancer progression and for identifying molecular classes or subgroups in different types of cancers [117-120]. Furthermore, they have been demonstrated to be more resistant to degradation compared to mRNA, especially in formalin-fixed paraffin-embedding tissues, so that they can be analyzed in retrospective studies [121, 122]. Therefore, it's important to assess the effect of formalin and Bouin's fixation in both mRNA and miRNAs specimens and define the reliability of molecular analyses in light of the most recent available technologies. In order to compare the effect of formalin and Bouin's fixation, 30 primary tumors fixed in formalin and their respective matched tissues fixed in BS were selected and retrieved from our retrospective cohort. RNA expression was then investigated using two cutting edge technologies such as droplet digital PCR (ddPCR) and Nanostring® that are gradually entering the clinical settings, and a gold standard method such as quantitative real-time PCR.

3.9.1 RNA extraction

From each paraffin-embedded block, one 10-µm-thick section was cut and collected into 1.5-ml microcentrifuge sterile tubes. RNA isolation was carried out by the use of the Maxwell RSC® extractor (Promega, Madison, WI 53711-5399, USA) using two different purification protocols, one for RNA extraction and one specific for miRNA isolation from fixed tissues, as suggested by the manufacturer. In detail, tissue de-waxing was carried out by the use of 300 µL of mineral oil as provided by the Maxwell® RSC RNA FFPE kit (Promega, Madison, WI 53711-5399, USA; code

AS1440). Procedures of the abovementioned kits were strictly followed for protein digestion by proteinase K and the DNAse digestion step. Afterwards, the aqueous solution of digested samples was transferred into the cartridge of the Maxwell® RSC miRNA tissue kit or Maxwell® RSC RNA tissue kit (Promega, Madison, WI 53711-5399, USA; code AS1460), for RNA isolation. Elution of the samples was done in 30 μL of nuclease-free water (Promega, Madison, WI 53711-5399, USA) for miRNA extraction protocol and 50 μL for RNA extraction protocol.

3.9.2 Yield and purity

RNA concentration and purity were measured by Nanodrop ND 1000 spectrophotometer (Thermo Scientific) using 1μl of RNA solution. The A280/260 and A260/230 absorbance ratios were used to assess purity, considering a ratio between 1.8 and 2.0 to be pure.

3.9.3 Integrity

RNA integrity and the extent of RNA fragmentation was estimated by microcapillary electrophoresis in an Agilent 2100 Bioanalyzer using RNA 6000 Nano kit (Agilent Technology) following manufacturer's instructions. For miRNA analysis, sample aliquots were diluted at 10 ng/μL just before use and measured using Small RNA kit (Agilent Technology, Santa Clara, CA 95051, USA). The integrity of miRNA was calculated as the relative abundance of miRNA species (10–40 nt) in comparison to the total amount of small RNA fraction (10–150 nt).

RNA smear analysis, included in the Agilent Bioanalyzer 2100 Expert software, was used to analyze the fragments' size distribution of RNA. The range of fragments' size analysis was manually set between 1 and 600 bp and divided in 5 smear regions (1-59, 60-149, 150-299, 300-449, 450-600 nucleotides).

3.9.4 Reverse Transcription

mRNA

Reverse transcription (RT) PCR reactions were performed using a two-step protocol. RT was carried out as already described [123]. Briefly, 360 ng of RNA were primed with random hexamers and reverse transcribed into cDNA in a 20 μl final volume using 250 U of M-MLV (Thermoscript RT-PCR System - Invitrogen). The reverse transcription was carried out at 37 °C for 60 min, afterwards the enzyme was inactivated by heating at 70 °C for 10 min. Samples were aliquoted and stored at -80°C.

microRNA

For miRNA analyses, twenty nanograms of RNA was reverse transcribed into cDNA in 10 μL final volume, using the miRCURY LNA RT (Qiagen, Hilden, Germany) according to manufacturer's instructions. The cDNA was then split into aliquots of 2 μL and stored at −80 ◦C until use.

3.9.5 Real-time PCR

mRNA

Real-time PCR assays were carried out on Mastercycler® ep Realplex (Eppendorf, Hamburg, Germany). Amplification was made using JumpStartTM Taq ReadyMixTM (Sigma-Aldrich, USA) and a mix of unlabeled PCR primers together with TaqMan probes for the following target genes: glyceraldehyde-3-phosphate dehydrogenase (GAPDH), β actin (ACTB), Endogenous RNAse Resistant (ERR) Marker, AKT1 and Kruppel Like Factor 16 (KLF16). To assess the integrity of targeted mRNA species the differential amplification ($\Delta Amp=Cq_{amp1}-Cq_{amp2}$) of each gene with different amplicon lengths was measured as described by Björkman *et al* [124]. For GAPDH we analyzed 3 amplicons with increasing lengths (60, 100 and 140 bp), while for β actin (66, 95 bp) and ERR marker (100 and 200 bp) two stretches were analyzed. With respect to AKT1 and KLF16, only one stretch at 77 bp for both genes were analyzed without applying the differential amplicon method. A summary of the primers sequences and amplicon lengths are shown in **Table 4**.

TABLE 4. Amplification primers used for RT-qPCR

Gene	Primer	Length
Glyceraldehyde-3-phosphate dehydrogenase	Rev- 5'-CAT CGC CCC ACT TGA TTT TG-3'	60
	Fw- 5'-AAT GGA AAT CCC ATC CAC CAT CT-3'	
	Rev- 5'-CAT CGC CCC ACT TGA TTT TG-3'	100
	Fw- 5'-GCA CCG TCAA GGC TGA GAA C-3'	
	Rev- 5'-CAT CGC CCC ACT TGA TTT TG-3'	140
	Fw -5'-ATG GTT TAC ATG TTC CAA TAT GAT TCC-3'	
β actin	Fw -5'-CGG CCC CCT CCA TCG T-3'	66
	Rev- 5'-AAA GGG TGT AAC GCA ACT AAGTCAT-3'	
	Fw- 5'-GTG GAT CAG CAA GCA GGA GT-3'	95
	Rev- 5'-AGG GTG TAA CGC AAC TAA GTC-3'	
AKT1	Fw- 5'- CCA CTG TCA TCG AAC GCA CCT-3'	77
	Rev – 5'-CAC AGT CTG GAT GGC GGT TGT-3'	
Endogenous RNAse Resistant Marker	S	100
	M	
	M	200
	L	
KLF16	Fw – 5'- GTC AGA CCC AGA AAG GTG GA–3'	77
	Rev – 5' – GGACGGTTCTGGAACAAAAG-3'	

For GAPDH, AKT1, ACTB and KLF16, PCR was carried out in 21 µl final volume. Every reaction included 24 ng (GAPDH, ACTB, KLF16) or 65 ng (AKT1) of cDNA, 15 pmol of each primer, 4.5 mM MgCl2 and 4.2 pmol of TaqMan probe. For ERR marker PCR was performed in 10 µl final volume following manufacturer's instructions. Amplification programs are reported in **Table 5**. All reactions were run in triplicate. A no template control of sterile water instead of cDNA was used as negative control in each run.

TABLE 5. Real-time PCR conditions for target genes

Gene	Length (bp)	n° cycles	Denaturation	Annealing	Extension
GAPDH	65	40	20 sec at 95°C	30 sec at 59°C	30 sec at 72°C
	100	40	20 sec at 95°C	30 sec at 57.5°C	45 sec at 72°C
	140	45	20 sec at 95°C	30 sec at 59°C	30 sec at 72°C
ACTB	65	40	1 min at 95°C	1 min at at 60°C	
	95	40	15 sec at 95°C	1 min at at 60°C	
ERR Marker	100	40	20 sec at 95°C	1 min at at 60.3°C	
	200	40	20 sec at 95°C	1 min at at 60.3°C	
AKT1	77	40	15 sec at 95°C	1 min at at 60°C	
KLF16	77	45	15 sec at 95°C	1 min at at 56°C	

microRNA

For miRNA analyses by real-time PCR, the following miRNA were selected: miRNA let-7e-5p (MIMAT0000066), miR-423-3p (MIMAT0001340), miR-92a-1-5p (MIMAT0004507), miR-30d-5p (MIMAT0000245), miR-155-5p (MIMAT0000646), miR-200a-3p (MIMAT0000682), and miR-429 (MIMAT0001536). In particular, miR-423-3p and let-7e-5p were chosen as they have been reported to be stably expressed in high grade serous ovarian cancer [125] while the remaining ones were chosen for their content in GC and their expression in ovarian cancers [125-128]. Reverse transcribed samples were diluted 40x just before use, and real-time PCR was run using 4 µL of diluted cDNA corresponding to 0.4 ng of cDNA in a total reaction volume of 10 µL. The reaction mixture was composed of 1 µL of the specific miRCURY miRNA Assay primer set (Qiagen, Hilden, Germany) and 5 µL of Fast EVA Green qPCR mastermix (Biotium, Fremont, CA 94538, USA). All reactions were run in duplicate, and a negative control without cDNA was added in each run. Samples were amplified on a Mastercycler® ep Realplex (Eppendorf, Hamburg, Germany) using the following cycling conditions: 95°C for 10 min, 40 cycles of 95 °C for 10 s and 60 °C for 1 min. For mi-92a-1-5p and miR-30d-5p, an annealing-extension temperature of 56 °C was applied; for miR-200a-3p and miR-429, it was of 58°C. For every miRNA tested by real-time PCR, a standardization curve was created using a pool of cDNA from Bouin's and FFPE samples. Standard curve was generated for three points using the following dilutions: 10x (0.4 ng/µL); 40X (0.1 ng/µL); 160x (0.025 ng/µL) for all the analyzed miRNAs. Standard curves were generated in duplicate for each miRNA and each

pool of cDNA using 4 μL of diluted cDNA per replica. Cases with differences of Ct ≥ 0.5 cycle were repeated in triplicate.

3.9.6 Droplet digital PCR

By now it's common in oncology and other fields of medicine to diagnose acquired and inherited disorders by determining the presence or the expression level of specific nucleotide sequences. However, the concentration of nucleic acids in clinical samples such as blood, urine and archive tissues can be too low for being detected or reliably quantified, also for gold standard methods such as real-time PCR [129]. In order to overcome this problem, in the past years digital PCR (dPCR) has been develop as a technique able to detect nucleic acids with unparallel sensitivity [130-132]. In dPCR, sample is partitioned and diluted into several partitions so that each partition contains a discrete number of target molecules. Diluting and partitioning has several advantages: the first is that, having the partitions a small reaction volume, the concentration of target molecules is subsequently increased, improving also the limit of detection (LOD). The second is that target molecules are purified by interfering compounds (the ratio between target molecules and background is higher), resulting in higher resilience to PCR inhibition [133]. Lastly, contrary to other PCR methods where there's a necessity of using a reference to perform target quantification, dPCR measures each single molecule, returning an absolute quantification of the target. In fact, while in standard analog PCR the concentration of the sample is proportional to the fluorescence amplitude, in dPCR sample's concentration is proportional to the number of empty partitions; the resulting quantification is therefore digital since the counting of partions is binary: the target is present (1) or not (0). A comparison between analog assay and digital assay is depicted in **Figure 24.**

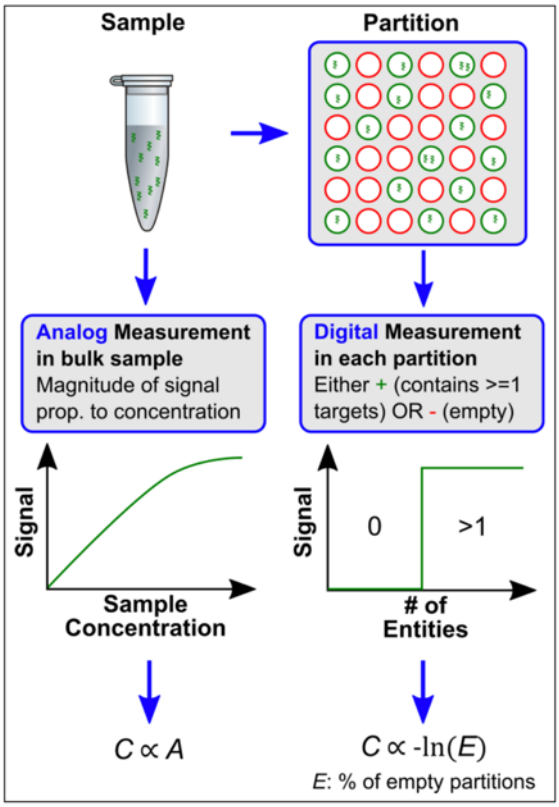

FIGURE 24. Comparison of dPCR assay with analog PCR assay. Adapted from A. S. Basu (A. S. Basu 2017).

Partitioning can be made using two different approaches: by building an array of physically isolated wells or by creating droplets emulsion where each droplet represents a single partition. The latter method, named also droplet digital PCR (ddPCR), has become very popular and has been notably improved since its introduction. In recent years, Bio-Rad has commercialized the QX200 digital PCR system which allows sample partitioning in up to 20.000 water-in-oil droplets of 1 nL volume, resulting in high level of sensitivity. When performing the assay, samples are loaded in a multichannel cartridge together with a mineral oil containing surfactant, and then put into a droplet generator. Thanks to the creation of a vacuum in the cartridge outlet microcapillary, a negative pressure is produced, and the resulting force drives droplets generation at the water-oil interface. After partitioning, samples are loaded into the droplet reader where the fluorescence of each droplet is detected and counted (**Fig. 25**)

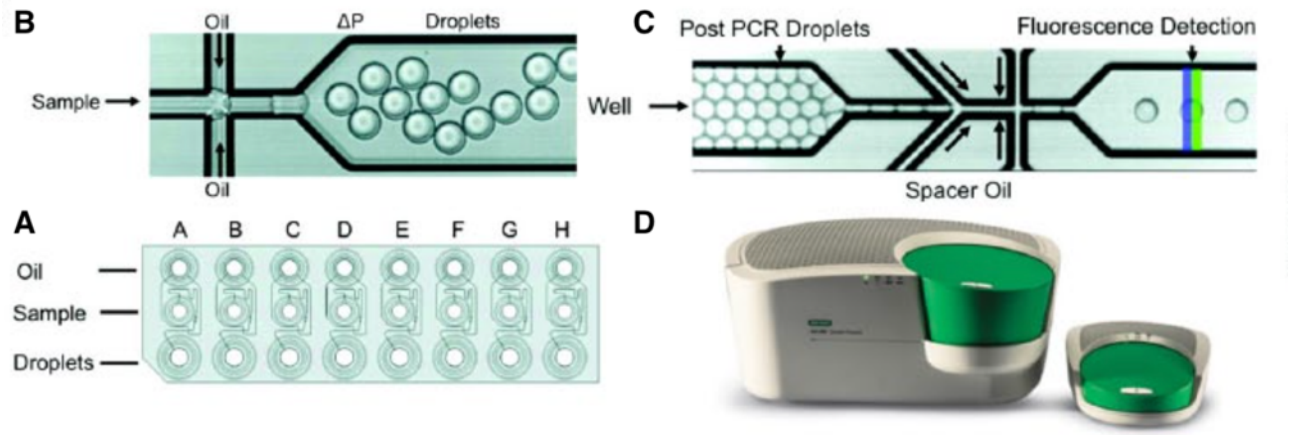

FIGURE 25. Schematic view of Bio-Rad QX200 ddPCR workflow. The system is composed of two instruments, the droplet generator and the droplet reader (D). Samples and mineral oil are loaded into a multichannel cartridge and put into the droplet generator (A). A negative pressure is applied on the microcapillary allowing droplets generation. Partitioned sample is then amplified in a classical thermocycler (B). After PCR, amplified samples are loaded into the droplet reader which counts positive and negative droplets by detecting the fluorescence. Adapted from A. S. Basu (A. S. Basu 2017).

mRNA

The gene expression of ACTB (95 bp), GAPDH (100 bp), KLF16 (77bp) and AKT1 (77bp) were assessed using droplet digital PCR reader according to manufacturer's instructions. To relate ddPCR data with platforms working at different dynamic range, such as qRT-PCR and Nanostring, a standard curve for each sample was run by plotting the log2 of cDNA starting quantity against the obtained log2 copies/µl. Each standard curve was run in duplicate using a two-fold dilution series over four points, ranging from 18 ng to 2 ng. For samples having a sub-optimal concentration, a different range was used. The log2 nominal copies at the cDNA amount used on qRT-PCR and Nanostring assays were then interpolated from the standard curve for cross-platform comparisons.

Reactions were performed in 20 µl final volume using 1× ddPCR Supermix for Probes (no dUTP, Bio-Rad), 18 pmol of each GAPDH (100 bp length), ACTB (95 bp length), AKT1 (77 bp length) and KLF16 (77 bp length) primer and 5 pmol of TaqMan probe. A no template control was run in each assay as negative control. Droplet generation was performed in a QX200TM Droplet Generator (BioRad, USA). Droplets' emulsion was transferred to a 96-well semi-skirted plate (Eppendorf, Germany), foil-sealed twice at 179 ◦C for 3 s and PCR was run in a thermocycler (iCycler, BioRad, USA) as follows: denaturation at 95 °C for 10 min; 40 cycles of 94°C for 30s and 54°C (KLF16), 56°C (GAPDH) or 58°C (ACTB and AKT1) for 1 min; enzyme inactivation at 98 °C for 10min. After amplification, droplets' fluorescence was read in the QX200TM Droplet Reader (BioRad, USA). ddPCR data were analyzed using QuantaSoftTM software and droplets' count was fitted to a Poisson distribution to obtain the absolute concentration (copies/µl) of the target sequence.

microRNA

Four microliters of 40x diluted cDNAs was used in each ddPCR reaction for a direct comparison with real-time PCR. The reaction mixture contained 1x final of QX200TM EvaGreen ddPCR Supermix (BioRad, Hercules, CA 94547, USA) and the miRCURY LNA PCR primer set at the appropriate concentration, which was set up experimentally for each miRNA investigated in the present study. A non-template control of deionized water was used instead of cDNA samples in each reaction. Droplet generation was performed in a QX200TM Droplet Generator (BioRad, Hercules, CA 94547, USA). The droplets' emulsion was transferred onto a 96-well plate (Eppendorf, Hamburg, Germany), which was foil-sealed twice at 179 °C for 3 s in a PX1 PCR Plate Sealer (BioRad, Hercules, CA 94547, USA) and PCR was run in a iCycler thermocycler (BioRad, Hercules, CA 94547 USA) as follows: 95 °C for 5 min; 40 cycles of 95 °C for 30 s and 56 °C for 1 min; signal stabilization at 4 °C for 5 min and 90 °C for 5 min, and final hold at 4 °C. The annealing/extension temperature for miR-155-5p, miR-200a-3p, and miR-429 was 57 °C. After amplification, the fluorescence of each droplet was read in the QX200TM Droplet Reader (BioRad, Hercules, CA 94547, USA). Droplet digital PCR data were analyzed using QuantaSoftTM software and droplets' count was fitted to a Poisson distribution to obtain the absolute concentration (copies/μL) of the target sequence.

3.9.7 Nanostring®

mRNA

Nanostring® platform was used to quantify RNA isolated by Maxwell® RNA FFPE kit in 8 matched formalin/Bouin pairs. Seven pairs were selected for their good quality showed on BioAnalyzer, Nanodrop and RT-qPCR analyses, while one pair (385) was selected as it exhibited good quality on Nanodrop and Bioanalyzer platforms, but not on RT-qPCR. The same Nanostring CodeSet composed of 71 gene elements, previously used for the validation of HERCULES biomarkers, was also used in this analysis. Samples preparation and hybridization were carried out according to the manufacturer's instructions as previously described in this thesis.

3.9.8 Data normalization

mRNA

The AKT1 and KLF16 expression levels obtained by RT-qPCR, Nanostring and ddPCR were normalized using ACTB and GAPDH housekeeping genes. For RT-qPCR, normalization was calculated according to the relative quantification method proposed by Livak [134]. The geometric mean of ACTB and GAPDH Cts was used as reference gene while the mean of all formalin and

Bouin's samples Cts was used as calibrator. For ddPCR and Nanostring, AKT1 and KLF16 log2 copies/µl were normalized using as reference gene the geometric mean of ACTB and GAPDH log2 copies/µl.

microRNA

miRNA expression levels obtained by real-time qPCR were normalized using let-7e-5p and miR-423-3p as normalizing miRNAs, as returned by Bestkeeper software. In normalizing data, the geometric mean of let-7e-5p and miR-423-3p Cts was used as reference gene, while the mean of formalin and Bouin's pooled samples was used as calibrator in the relative quantification method proposed by Livak et al. [134].

3.9.9 Measurement of RT efficiency

cDNA generated from five representative matched samples was used to assess the efficiency of reverse transcription by fluorometric measurement using the QuantiFluor® ssDNA System (Promega). Measurements were performed according to the manufacturer's instructions using the low standard calibration protocol. Briefly, five matched samples along with two aliquots of RT mixture without RNA were submitted to reverse transcription as previously described. The first aliquot was used as "Blank sample" while the second one was added with one ng of 1:100 QuantiFluor® ssDNA standard (provided with the kit) and used as "Standard sample". Ten µl of "Blank" and "Standard" samples were then added to 200 µl of working solution containing 1:2000 QuantiFluor® ssDNA dye and used to calibrate the instrument. After calibration, 10 µl of each sample were measured in 200 µl of working solution and the concentration (ng/µl) extrapolated from the relative fluorescence.

3.10 Statistical analyses

3.10.1 Immunohistochemistry (IHC), AFM and morphological analyses

Contingency analysis and Fisher's test were used to test the changes in the expression of categorical variables in ovarian versus omental sites. The paired t-test was used to compare H-scores and clinical variables with continuous distribution of ovarian versus omental sites. H-scores, gene expressions and clinical parameters were also dichotomized for subsequent analysis with respect to their median value of expression. Levels lower or higher than the median value were classified as "low" or "high" status respectively. Overall survival (OS) was defined as the time of HGSOC diagnosis to death or end of follow-up information, whichever came first. Progression free-survival (PFS) was defined as the time from the starting point of first line chemotherapy to the progression of the disease, while platinum free-interval (PFI) was defined as the time from the end of first line chemotherapy to the appearance of first progressive disease. Primary platinum response was classified in "never progressed" for patients without progression after first line chemotherapy, "platinum sensitive" for patients with PFI > 6 months and "platinum resistant" for patients with PFI < 6 months. The log-rank test and Kaplan-Meier curves were used to estimate and compare the dependence of HGSOC OS and PFS on single variables such as morphological features, immunohistochemical biomarkers, and clinical parameters. All p-values were calculated on two-sided and values <0.05 were considered statistically significant.

3.10.2 Molecular analyses

Data distribution was assessed by D'Agostino-Pearson and Shapiro-Wilk tests, for normal distribution, parametric tests were run, while non-parametric analyses were carried out for data distribution deviating from normality. For normally distributed variables paired t-test was run, while Wilcoxon signed rank test was used in case of data without normal distribution. Similarly, pairwise correlation analyses were carried out using Pearson r or Spearman r test according to data distribution, while linear regression analysis was used in cross-platform comparisons. For multiple t-test comparisons, the p-value correction with Holm-Sidak method was applied. Survival curves and comparisons between categorical variables in RNAscope® and Nanostring® assays were analyzed as described for IHC, AFM and morphological analyses. All p-values were calculated on two-sided and values <0.05 were considered statistically significant.

Statistical analyses were carried out using GraphPad Prism 8 software (GraphPad Software, Inc., San Diego, CA, USA) and R 3.4.4.

4 RESULTS

4.1 Clinicopathological features of the cohort

Overall, median progression-free and overall survival were 12 months (range, 1 to 189) and 35 months (range, 0 to 231), respectively. Significant associations between clinical parameters and OS and PFS are reported in **Fig. 26** and **Fig. 27**. In detail, optimal primary cytoreduction, secondary debulking surgery and low levels of CA125 and LDH before first line chemotherapy were associated with both longer OS and PFS. On the contrary, patients with late stage disease and those receiving neoadjuvant chemotherapy had significant lower OS, but not PFS. No significant association were found between overall or progression free survival and the other clinical features.

A total of 889 tissue fragments were retrieved from the 294 patients included in the study. Among them, 457 were fixed with standard buffered formalin while 432 were fixed in Bouin's solution (BS). Tumor specimens included 294 primary ovarian tumors, 172 tumor lesions of the contralateral ovary, 305 peritoneal implants and 119 lymph-node metastases. Tumor implants were mainly taken from omental sites (71%) while a minor part was taken from colon, Douglas peritoneum and sigma-rectum location.

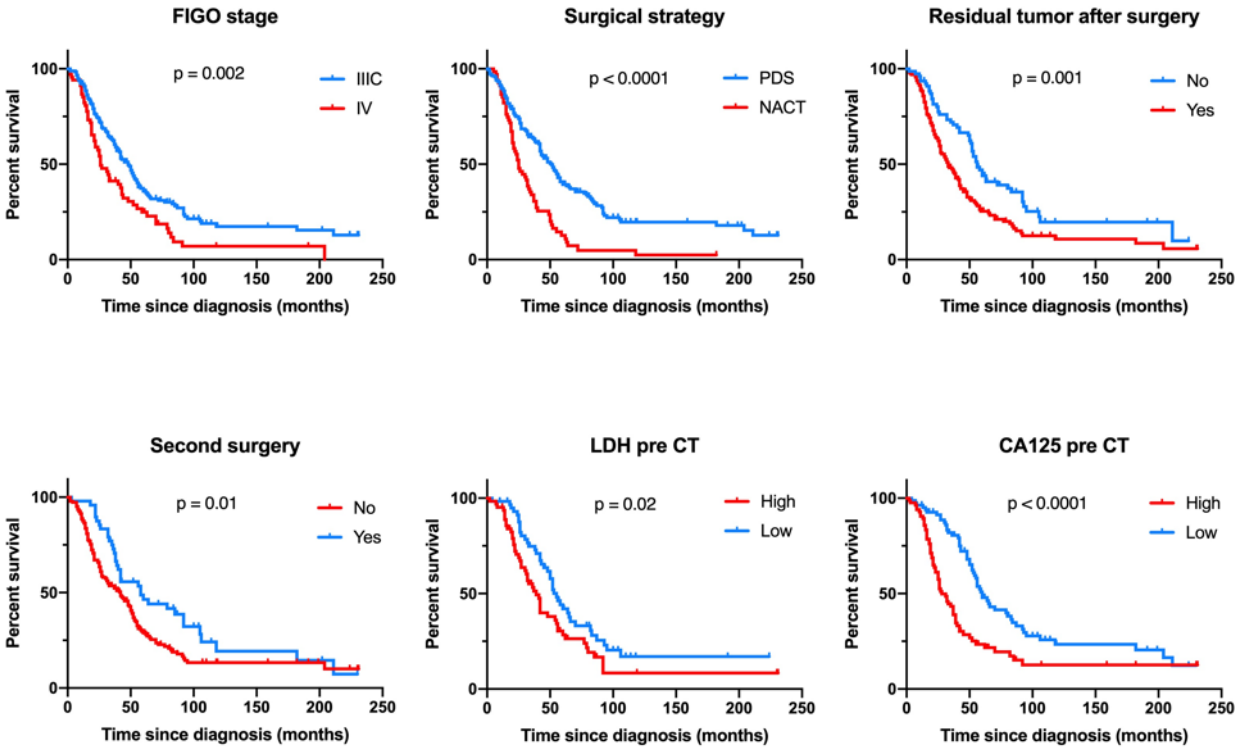

FIGURE 26. Clinical parameters significantly associated with overall survival (OS). PDS = primary debulking surgery; NACT = neoadjuvant chemotherapy; CA125 = cancer antigen 125; LDH = lactate dehydrogenase; CT = chemotherapy

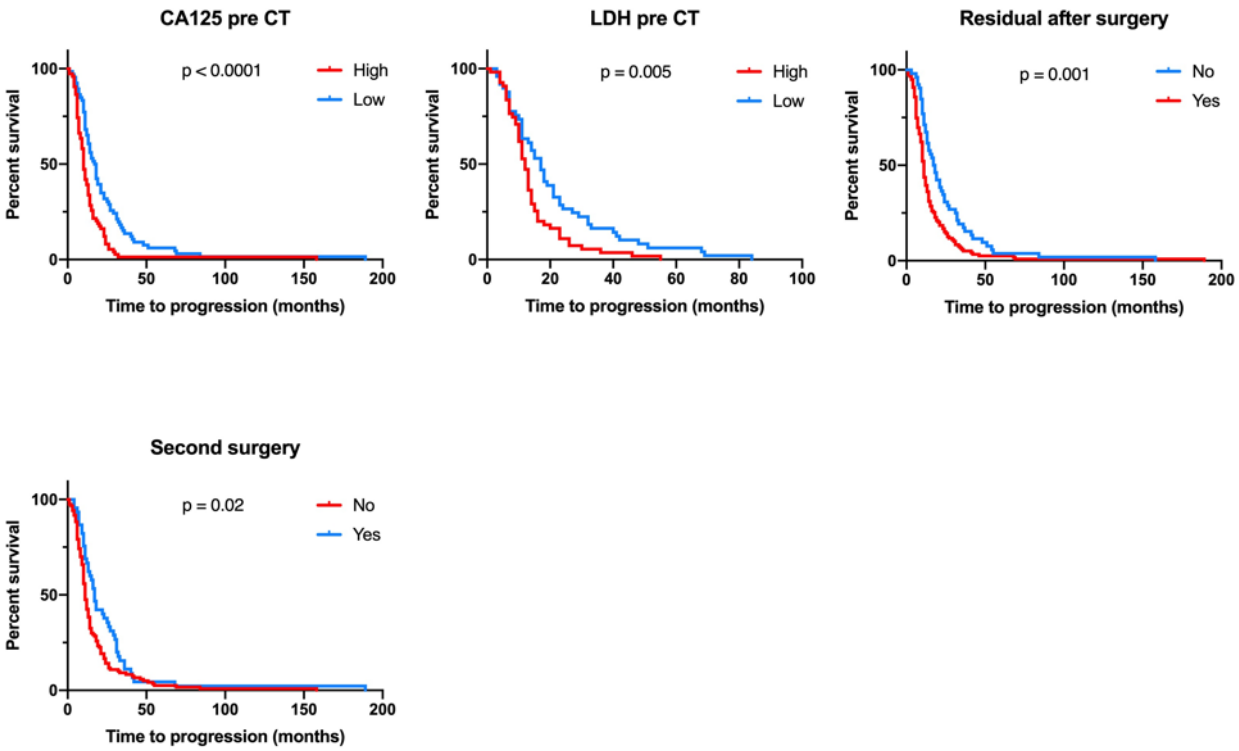

FIGURE 27. Clinical parameters significantly associated with progression free survival (PFS). CA125 = cancer antigen 125; LDH = lactate dehydrogenase; CT = chemotherapy

4.2 Morphological analyses

Morphological analysis was carried out in 884 H&E slides of ovarian tissues, peritoneal implants and lymph nodes obtained from 291 patients. Architectural pattern and "Classic" or "SET" classification were performed as previously described [51]. In total, 6 different patterns, present in tumor tissue as single entity or mixed, were observed: solid, papillary, endometrioid, microcystic, transitional and micropapillary. The most represented morphological architectures were papillary (34%), papillary solid (26%) and solid (18%) while the other patterns were less frequent. Among them, micropapillary pattern, pure or mixed with other architectures, was observed in 8% of the cases followed by microcystic (7%), transitional (5%) and endometrioid (2%). A summary of the architectural pattern distribution is depicted in **Fig. 28**.

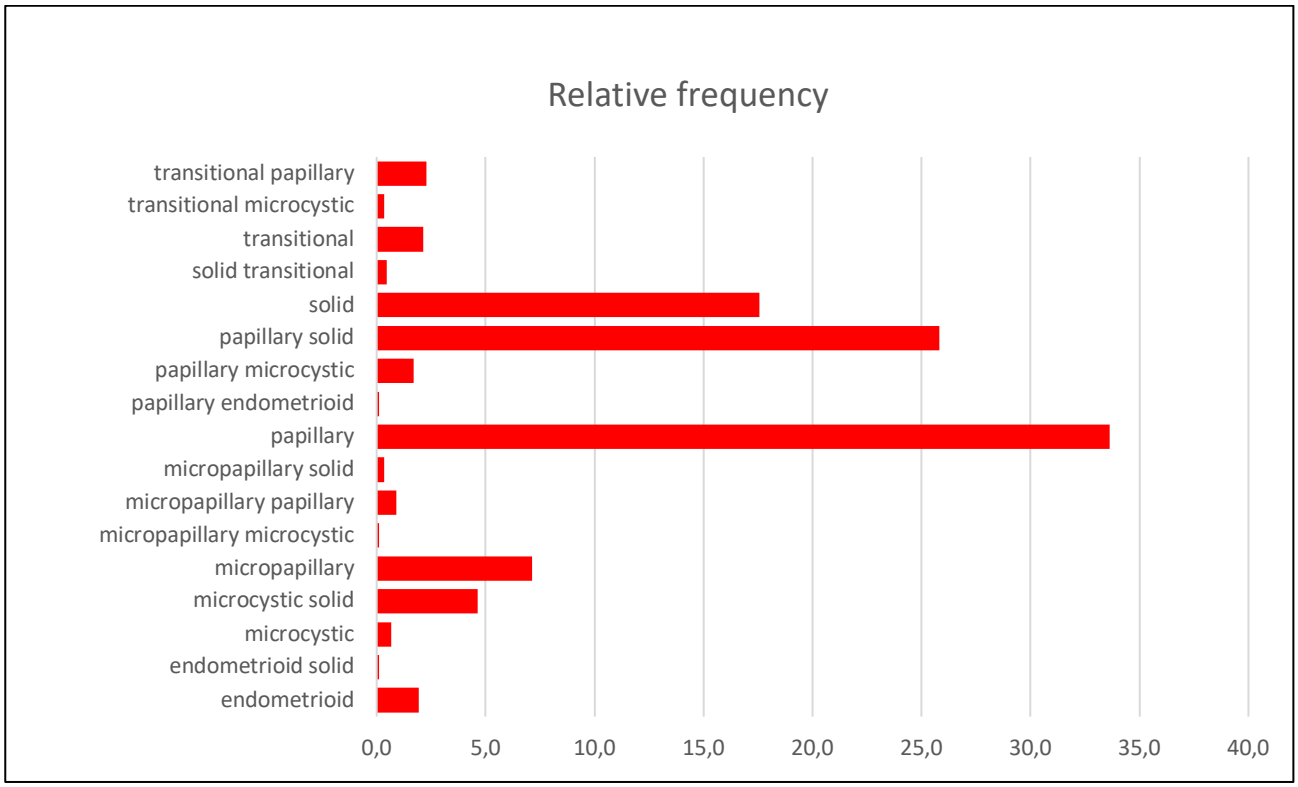

FIGURE 28. Relative frequency of HGSOC morphological patterns observed in this study

Tumors were then divided in "SET" (N = 403) and "Classic" (N = 481) and related to the other morphological variables in order to detect peculiar features of the two groups. The t-test comparisons between SET and Classic tumors showed that the first group had a significant higher number of mitoses ($P = 0.003$) and lymphocytes ($P < 0.0001$). These two features were also observed in tumors with relevant number of atypical mitoses ($P = 0.02$) and absence of psammoma bodies ($P < 0.0001$) indicating a possible relationship between these four cytological features and SET pattern. To support this hypothesis, we found also that tumors with higher percentage of SET features had relevant

number of atypical mitoses ($p < 0.0001$) and absence of psammoma bodies ($p = 0.0005$). Furthermore, in SET group the percentage of cases having tumor infiltrating lymphocytes into tumor epithelium and not just in the stroma, was much higher compared to classic group ($P = 7 *10^{-6}$).

As micropapillary pattern has been associated with a more aggressive behavior in different types of cancers, especially in breast cancer [135], we made a t-test comparison considering it as a separate entity from SET and Classic groups. Our results showed that micropapillary pattern is characterized by a lower number of mitoses and by a mean number of lymphocytes similar to those of SET tumors (**Fig 29)**. Nevertheless, it was significantly associated with shorter OS, compared to Classic and SET features, only when the pattern was detected in implants of patients submitted to PDS and not in those treated with NACT ($P = 0.004$).

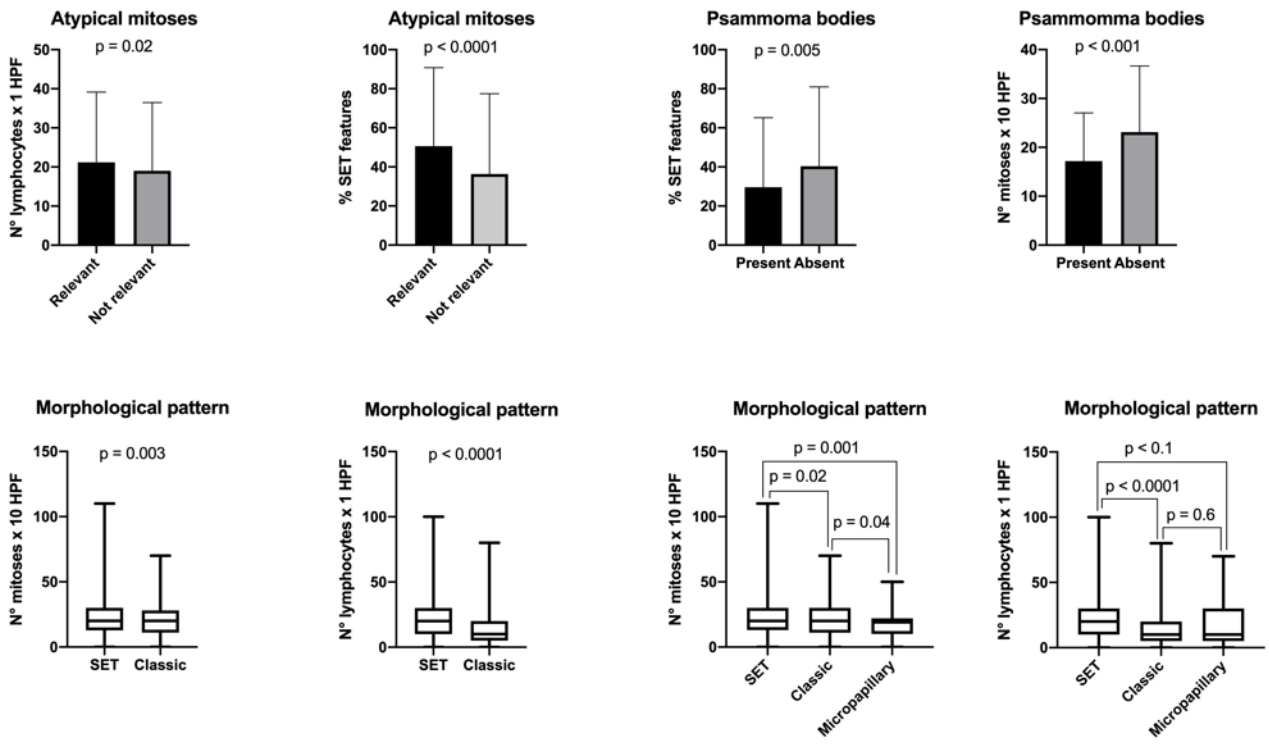

FIGURE 29. Morphological features significantly associated with SET and Classic groups. SET = solid endometrioid transitional.

In order to relate morphological features with clinicopathological variables, for each patient the mean value from ovarian sites, implants and lymph nodes was calculated. Subdivision in SET and Classic groups was then computed according to the new average value. Statistical analyses reconfirmed that patients with prevalent SET pattern have significantly higher number of lymphocytes (≥ 17 lymphocytes x 1 HPF) ($P = 0.0002$) compared to Classic, while only a trend toward higher number of mitoses was found ($P = 0.08$). Interestingly, t-test comparison showed that patients with higher percentage of SET features and higher number of mitoses didn't progress after first line chemotherapy

(P = 0.0002 and P = 0.0006 respectively). Moreover, both the number of mitoses and percentages of SET were significantly lower in patients sensitive or resistant to first line chemotherapy compared to those who never progressed (**Fig 30**).

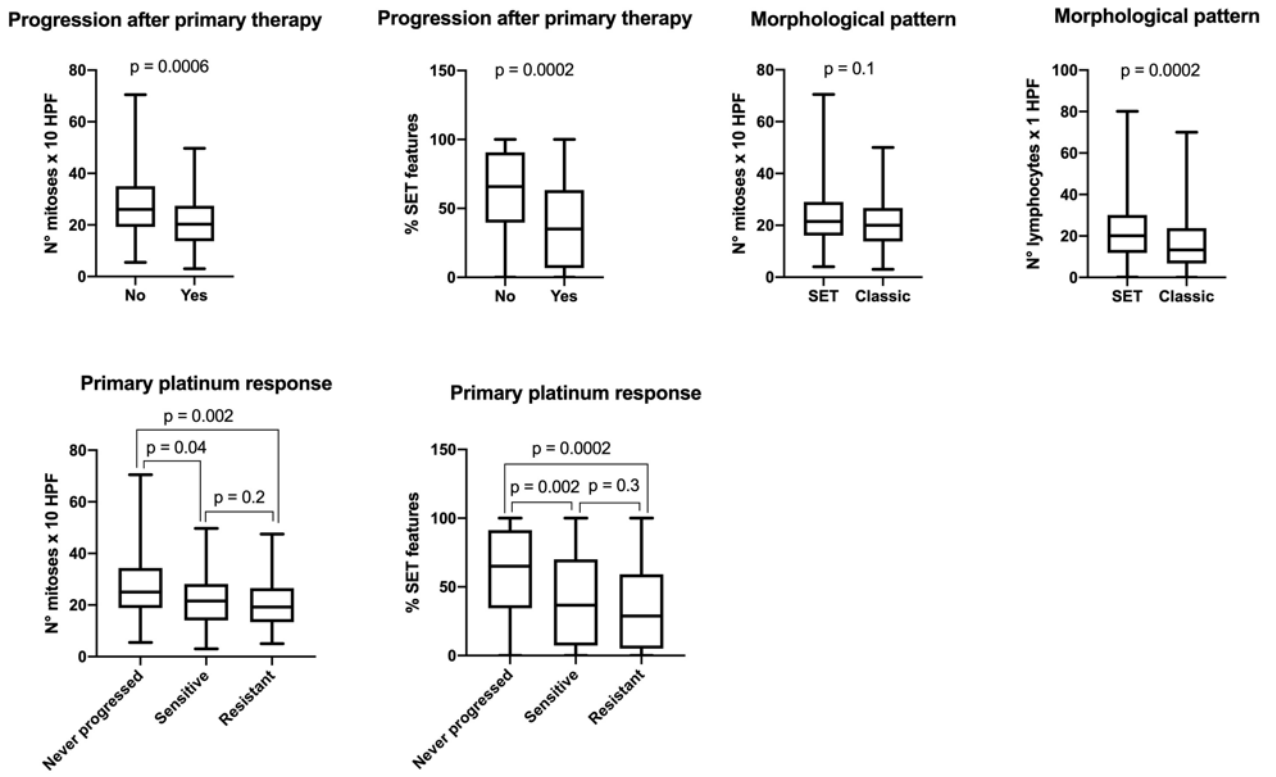

FIGURE 30. Morphological features significantly associated with SET/Classic groups or with clinicopathological variables.

With regard to patient's outcome, our analyses clearly showed that morphological features have a different impact on the prognosis of patients submitted to neoadjuvant chemotherapy and those receiving primary cytoreduction. In detail, the presence of a high number of lymphocytes (≥ 17 lymphocytes x 1 HPF) (P =0.05) (**Fig. 32**) and SET features (P = 0.03) (**Fig. 31**) are associated with longer overall survival, but only in patients treated with primary debulking surgery and not in those submitted to neoadjuvant chemotherapy. All other morphological variables were not associated with both OS and PFS.

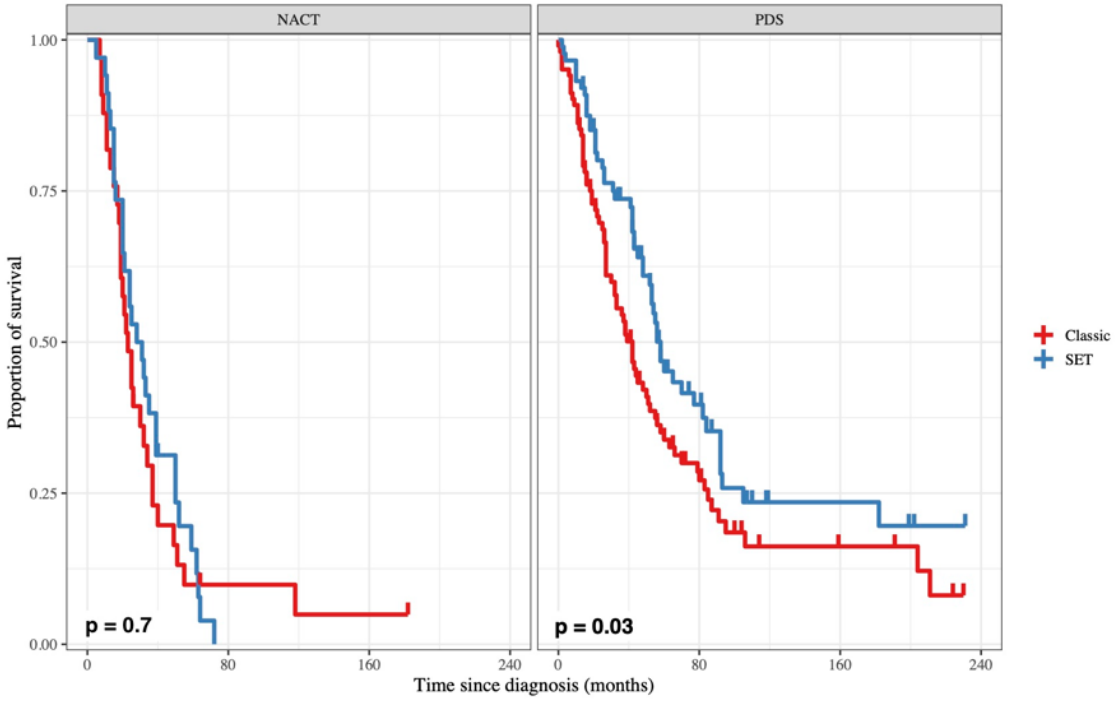

FIGURE 31. Association between Classic/SET features and overall survival in patients submitted to neoadjuvant chemotherapy (NACT) or primary debulking surgery (PDS).

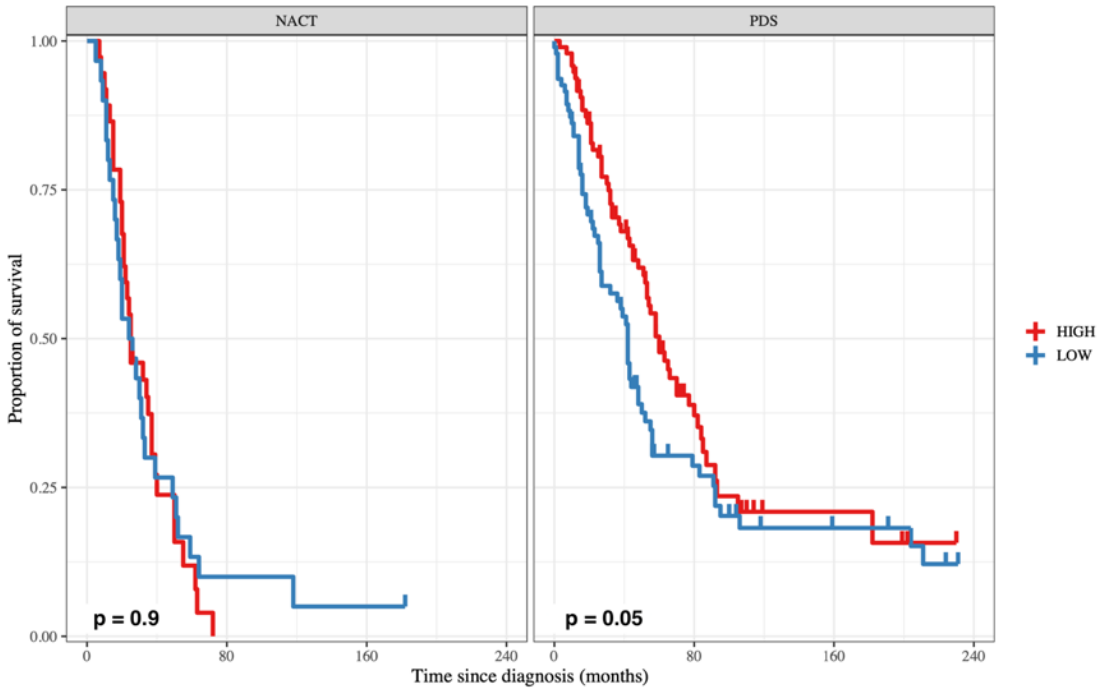

FIGURE 32. Association between number of lymphocytes and overall survival in patients submitted to neoadjuvant chemotherapy (NACT) or primary debulking surgery (PDS).

4.3 Immunohistochemical analyses

IHC analysis was carried out in 373 FFPE tissues obtained from 187 patients. Among the 373 tissues analyzed, 239 were primary tumors from the two ovaries (N = 169 “ovary1” and N = 70 “ovary2”), while 134 were implants from peritoneal sites. Of the 169 patients with primary tumors (“ovary1”), 64 had a tumor lesion in the contralateral ovary (“ovary2”) while 115 presented a peritoneal implant. When considering “ovary2”, among the 70 patients, 50 had also a peritoneal implant. In total, 57 patients had a tumor lesion in all three anatomical sites (“ovary1”, “ovary2” and peritoneal implant). Considering all 373 tissues, the overall expression pattern of the seven biomarkers (p53, p16, WT1, Ki67, PR, HNF1β and BRCA1) confirmed the diagnosis of HGSOC for almost all patients of our cohort as profiles were concordant with those reported by Kobel *et al*. HGSOC were characterized by high p53, p16, WT1 and Ki67 H-score levels, but lower rates of PR, HNF1β and BRCA1. The mean H-score for each biomarker is depicted in **Fig 33**. Tissue biopsies of eight patients displayed a different pattern of expression and were reclassified as mucinous carcinoma (N°=1), clear cell carcinoma (N°=1) and low-grade serous carcinoma (N°=5) confirming the specificity of the panel used. These cases were excluded from the study. Tissue samples showed positive staining in >81% of cases for WT1, p16, Ki67 and BRCA1. The positivity rate of p53 and PR was 67% and 55% respectively, while HNF1β was positive in 7% of the cases.

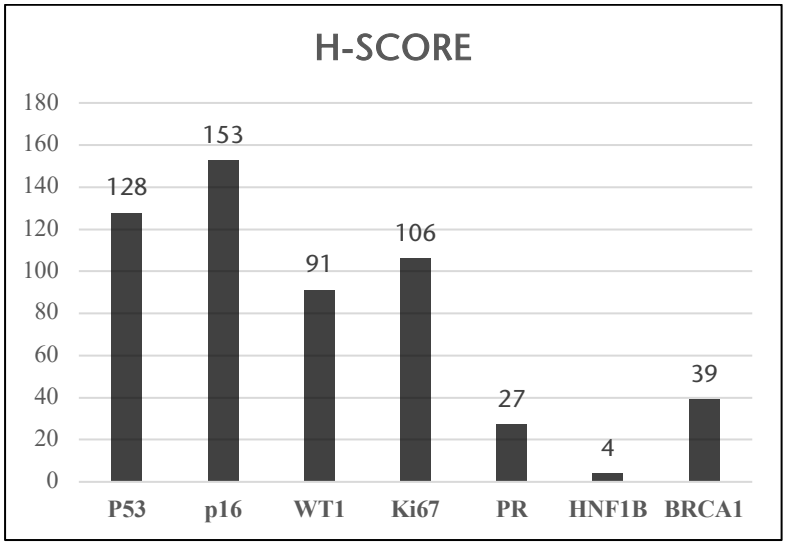

FIGURE 33. Mean nuclear H-score levels for each biomarker in the entire cohort of samples. Column numbers identify the specific H score of the biomarker.

We then look for potential differences in immunostaining between the two ovaries and peritoneal sites by comparing the nuclear H-score of each biomarker in 57 patients having tumor lesions in all

three sites. H-score levels of the biomarkers at the ovarian and peritoneal sites are shown in the heatmap in **Figure 34**, with representative immunostaining shown in **Figure 35**.

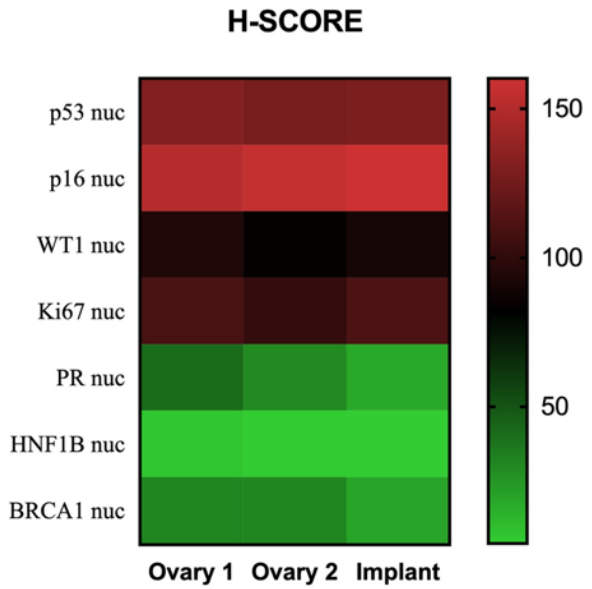

FIGURE 34. Heatmap of H-score levels for each biomarker in ovarian and implant sites. nuc = nuclear staining.

Overall, the mean H-scores of all biomarkers were similar between the two ovaries and the implants except progesterone receptor (PR) and BRCA1. The mean H-score of PR was similar in the two ovarian sites ($P = 0.55$), but it was significantly higher in ovaries when compared to the peritoneal site ($P < 0.0001$ and $P = 0.04$ respectively). In the same way, the mean BRCA1 H-score was higher in ovaries compared to implant sites ($P = 0.03$ and $P = 0.02$), without any difference in the two ovaries ($P = 0.69$). The same results were obtained when comparing 115 “ovary 1” tumors with the corresponding implants, 50 “ovary 2” tumors with the corresponding implants and 60 “ovary 1” with their “ovary 2” tumors.

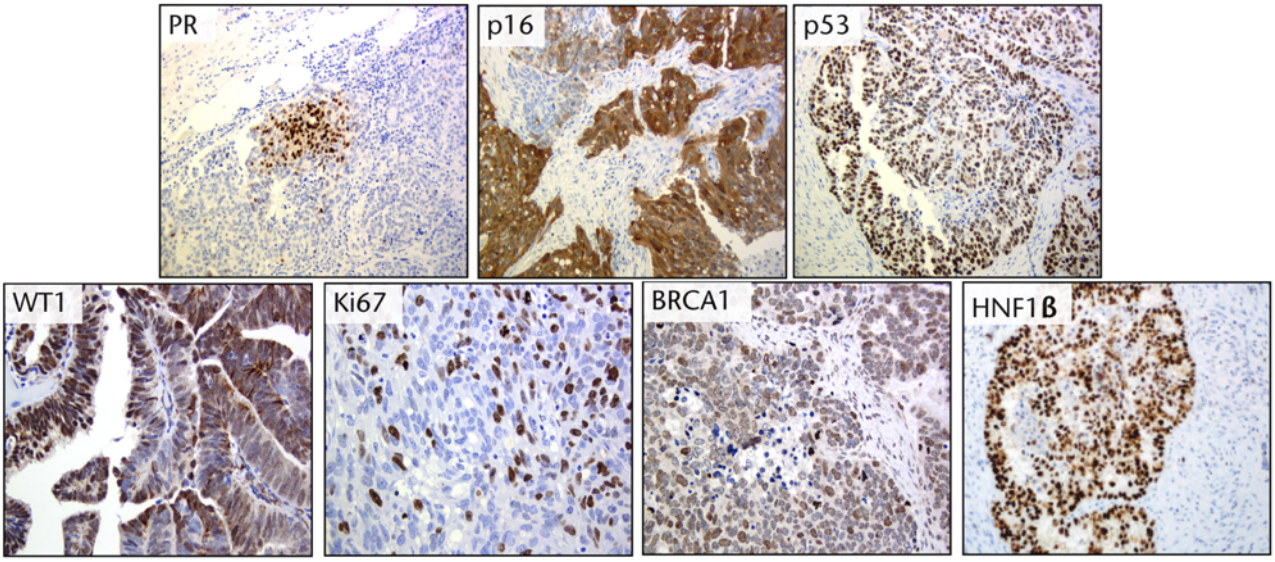

FIGURE 35. Representative IHC staining pattern of the biomarkers of our panel at 20X magnification. PR = progesterone receptor; WT1 = Wilm's tumor protein 1; HNF1β = hepatocyte nuclear factor 1- β; BRCA1 = breast cancer type1 susceptibility protein.

Among the 373 tissues analyzed, staining pattern varied broadly across the biomarkers studied. The frequency distribution of staining patterns for each biomarker is depicted in **Fig. 36.** P53 expression was mostly homogeneous (49%) or negative (32%) with 19% of cases exhibiting a heterogenous pattern. According to literature [136, 137] p53 staining patterns are related with p53 mutational status. Homogenous pattern is associated with the presence of a missense p53 mutation, negative pattern with a non-sense mutation or gene deletion while heterogeneous pattern can be associated with both wild type condition and gene-splicing variants. The prevalent expression patterns of p16 were homogeneous (66%) and heterogeneous (32%), while negativity was observed in only 2% of the cases. Wilm's tumor protein 1 staining pattern was mostly heterogeneous (56%), followed by homogenous (30%) and negative (14%). With regard to Ki67, its expression was exclusively stochastic (94%), with 20 cases (5%) having a homogeneous pattern and only one case with complete absence of expression. Contrarily, progesterone receptor was negative in 43% of cases, with a equal distribution of stochastic (29%) and heterogeneous (26%) patterns and only 4 cases (1%) with homogeneous expression. Similar to progesterone receptor, HNF1β staining was negative in most cases (79%) with an equal distribution of stochastic (10%) and heterogeneous (10%) patterns, without cases with homogeneous expression. Lastly, BRCA1 expression pattern was mostly stochastic (54%) or heterogeneous (34%), with 6% of cases having homogeneous or negative staining.

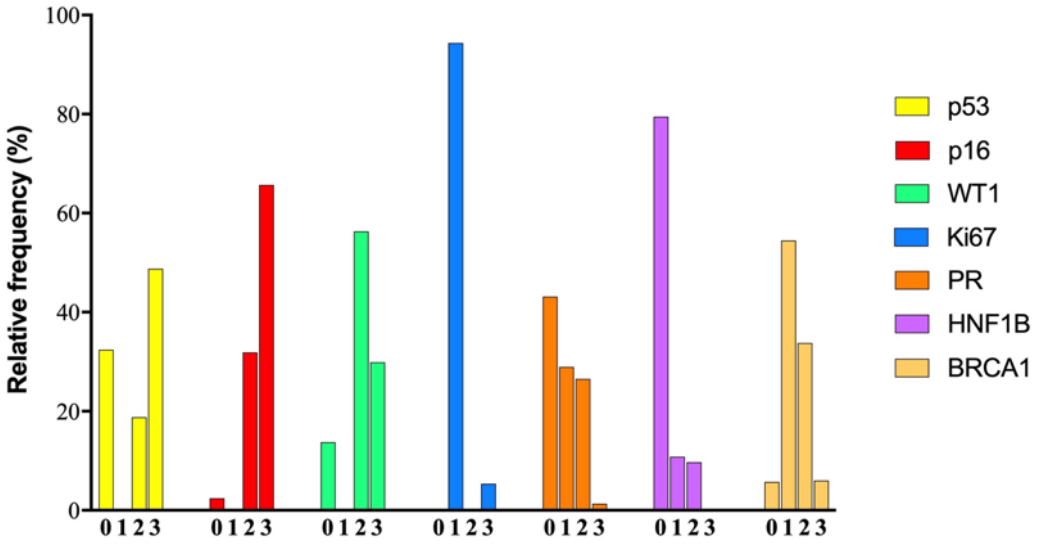

FIGURE 36. Distribution frequency of staining patterns among the biomarkers analyzed. Staining patterns: 0 = negative; 1 = stochastic; 2 = heterogenous; 3 = homogeneous. PR = progesterone receptor; WT1 = Wilm's tumor protein 1; HNF1β = hepatocyte nuclear factor 1-β; BRCA1 = breast cancer type1 susceptibility protein.

BRCA1 staining pattern in both ovaries (Ovary 1, N° = 169 cases; Ovary 2, N° = 64 cases), but not in peritoneal implants was significantly associated with overall survival (OS), while no association was found for progression free survival (PFS) (**Fig. 37**). All other biomarkers did not influence OS or PFS in any of the anatomical sites considered and for any pattern of staining.

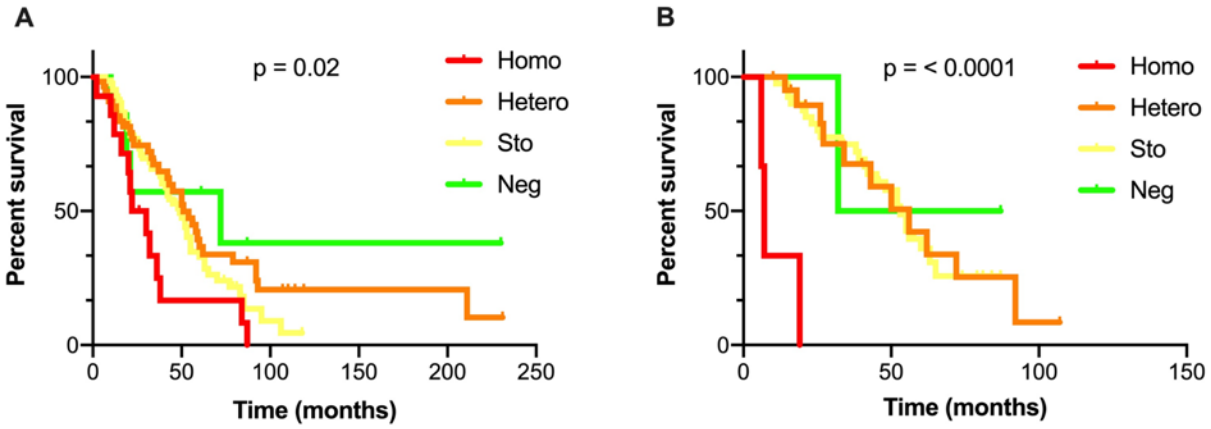

FIGURE 37. Overall survival of HGSOC patients according to BRCA1 IHC staining pattern in ovary1 (A) and ovary2 samples (B). Staining patterns: Neg = negative; Sto = stochastic; Hetero = heterogenous; Homo = homogeneous.

We next examined the concordance between ovarian and peritoneal staining patterns in individual cases (**Table 7**). On average, the proliferation marker Ki67 was the most stable among the biomarkers analyzed, showing a discordance in staining pattern between ovarian and omental sites in only 5% of cases, whereas p53, p16 and HNF1β immunostaining were discordant in 12%, 10%

and 13% of cases, respectively. Contrarily, WT1, PR and BRCA1 were highly variable with different staining pattern at ovarian and omental sites in 34%, 44% and 30% of cases respectively.

TABLE 7. Discordance of IHC Staining Pattern (Homogenous, Heterogeneous, Negative, Stochastic) Comparing Ovarian and Omental Sites

Antibody	% of discordant cases			
	Ovary1 vs Ovary2 (N=64)	**Ovary1 vs implant (N=115)**	**Ovary2 vs implant (N=50)**	**Mean**
p53	12%	14%	10%	12%
p16	8%	14%	7%	10%
WT1	41%	37%	25%	34%
Ki67	3%	6%	7%	5%
PR	50%	44%	37%	44%
HNF1β	16%	13%	10%	13%
BRCA1	29%	36%	25%	30%

Discordance in staining patterns in any site did not influence patients' OS and PFS for any of the biomarkers analyzed.

In order to correlate biomarkers' expression with clinicopathological variables, for patients having tissues available in both ovaries and implant locations, the mean H-scores derived from the three anatomical sites was calculated for each biomarker. According to univariate analysis (**Table 8**), BRCA1 H-score was significantly lower in patients sensitive to first line chemotherapy compared to resistant ones ($P = 0.02$) and in patients having higher number of tumor infiltrating lymphocytes ($P = 0.04$). Moreover, a trend towards lower levels of expression in patients with prevalent SET histology ($P = 0.06$) was found. This result was also supported by Spearman's analysis between BRCA1 H-score and SET percentage, (Spearman's rho = - 0.21; $P = 0.004$). Higher Ki67 expression was significantly associated to higher number of mitoses ($P < 0.001$). In addition, Ki67 H-score was found significantly higher in patients who didn't progress after primary therapy ($P = 0.04$) and in those with higher ratio lymphocytes - monocytes (LMR) ($P = 0.04$). Accordingly, log-rank test returned longer PFS in patients with higher Ki67 expression ($P = 0.04$), even excluding NATC patients ($P = 0.04$). With respect to p16, it was inversely associated to FIGO stage ($P < 0.0001$). Ki67 and p16 expression were also related to chemotherapy: Ki67 H-score was significantly lower in patients submitted to NACT compared to PDS, but p16 H-score was higher in NACT patients.

TABLE 8. Correlation between clinical/histo-morphological features and the mean H-score for each biomarker. PDS = primary debulking surgery; NACT = neoadjuvant chemotherapy; LMR = lymphocytes to monocytes ratio; NLR = neutrophils to lymphocytes ratio; SET = solid endometrioid transitional.

		***P* value**						
	n (%)	**BRCA 1**	**HNF1β**	**Ki67**	**p16**	**p53**	**PR**	**WT**
Age at diagnosis		0.1	0.02	0.9	0.8	0.3	0.1	0.9
Younger	94 (51)							
Older	89 (49)							
FIGO stage		0.5	1.0	0.6	**<0.01**	0.05	0.8	0.6
IIIC	132 (75)							
IV	43 (25)							
N° mitoses x 10 HPF		0.3	0.3	**<0.01**	0.8	0.7	0.06	0.7
High	93 (50)							
Low	93 (50)							
N° lymphocytes		**0.03**	1	0.8	0.52	0.8	0.4	0.3
High	93 (50)							
Low	93 (50)							
Progression after primary therapy		0.3	0.04	**0.04**	0.5	0.6	0.8	0.7
Yes	120 (80)							
No	30 (20)							
Surgical strategy		0.5	0.9	**<0.01**	**<0.01**	0.6	0.2	0.3
PDS	133 (73)							
NACT	49 (27)							
Primary platinum response		**0.04**	0.4	0.2	0.9	0.6	0.5	0.8
Never progressed	32 (22)							
Sensitive	66 (45)							
Resistant	50 (33)							
Residual tumor after surgery		0.8	0.9	0.3	0.3	0.9	0.2	0.2
Yes	112 (65)							
No	61 (35)							
% Morphological pattern		0.06	0.8	0.7	0.4	0.3	0.8	0.4
SET	100 (54)							
Classic	86 (46)							
LMR		0.6	0.6	**0.04**	0.3	0.8	0.6	0.2
High	54 (49)							
Low	57 (51)							
NLR		0.7	0.8	0.06	0.5	0.3	0.4	0.6
High	59 (53)							
Low	52 (47)							

* p-value < 0.05 was not considered significant when the number of cases after groups stratification was too low for t-test comparisons or median H-score was 0.

4.4 Molecular analyses – validation of HERCULES biomarkers

4.4.1 Nanostring®

Conclusive results were obtained from all 32 FFPE samples, that comprised 28 primary tumors and 4 peritoneal implants. Overall, samples exhibited almost the same expression profile. Heatmaps generated by unsupervised clustering approximately divided samples in four subgroups, but none of those signatures was associated with OS or PFS (**Fig 38**)

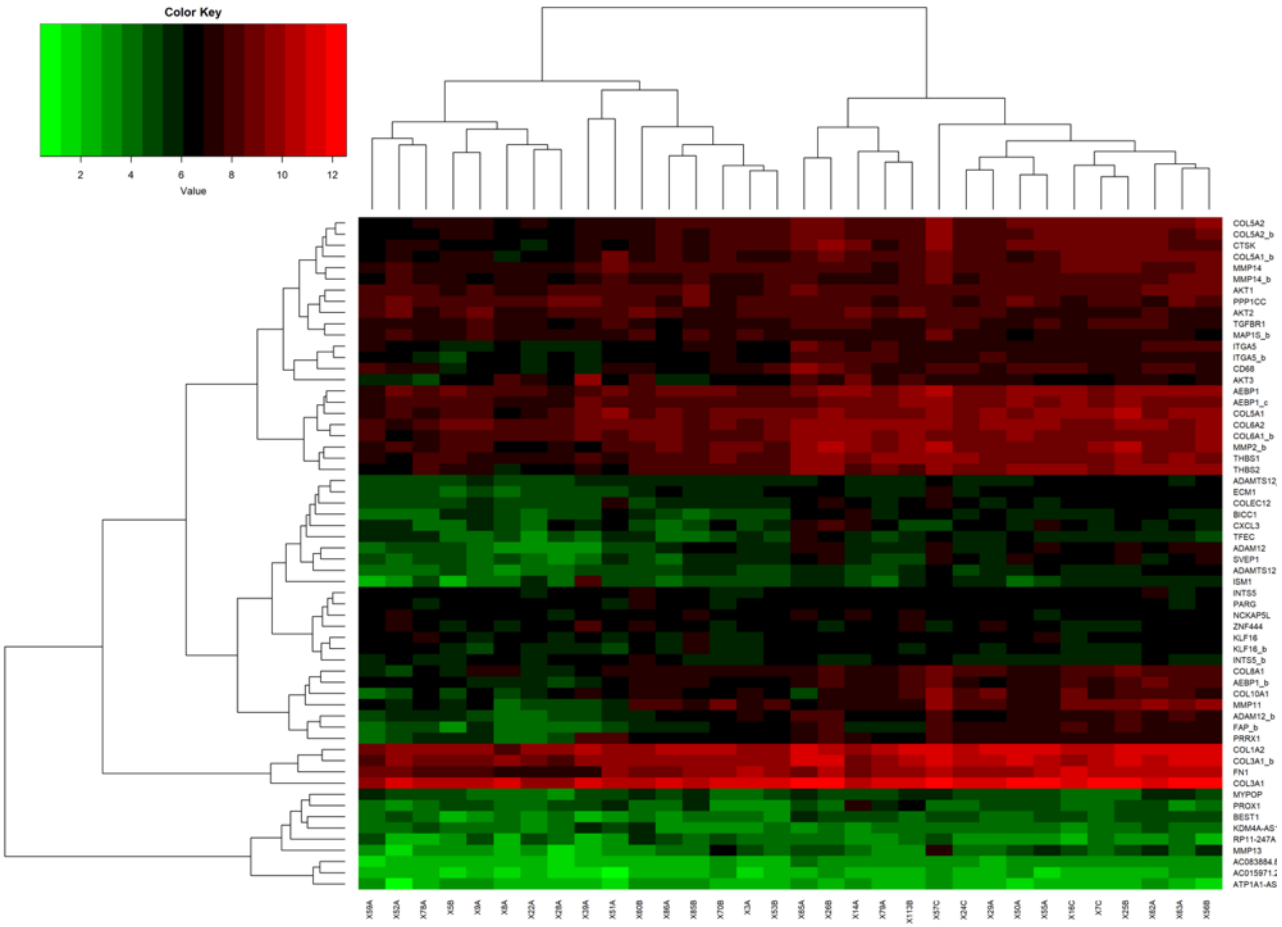

FIGURE 38. Unsupervised Hierarchical Clustering Heatmap of the 32 HGSOC samples. Gene expression values are expressed as log2 Nanostring counts.

In total, seven genes were found associated with clinicopathological variables (**Fig. 39**). In patients who received neoadjuvant chemotherapy, BEST1 and TFEC genes were significantly highly expressed compared to those who underwent primary debulking surgery only (P = 0.02 and P = 0.04, respectively), while PPP1CC had lower expression levels in NACT group (P =0.04). Two genes resulted related to primary platinum response: HGSOC patients who never progressed after first line treatments had lower levels of the lncRNA AC083884.8 compared to sensitive and resistant ones (P

= 0.04 and P = 0.05, respectively) and the expression was higher in sensitive group compared to resistant (P = 0.01), and compared to women who never progressed after treatment (P = 0.04) as shown in Figure .

Lastly, AKT2 expression was significantly lower in patients with FIGO stage IV if compared to lower FIGO stage. Furthermore, AKT2 expression seemed to influence positively both overall and progression free survival (P = 0.02 and P = 0.001 respectively). Interestingly, our results showed that AKT isoforms are differently related to patients' outcome: patients with highly expression of AKT1 had the shortest OS, but those with higher AKT2 had the longest (**Fig 40**).

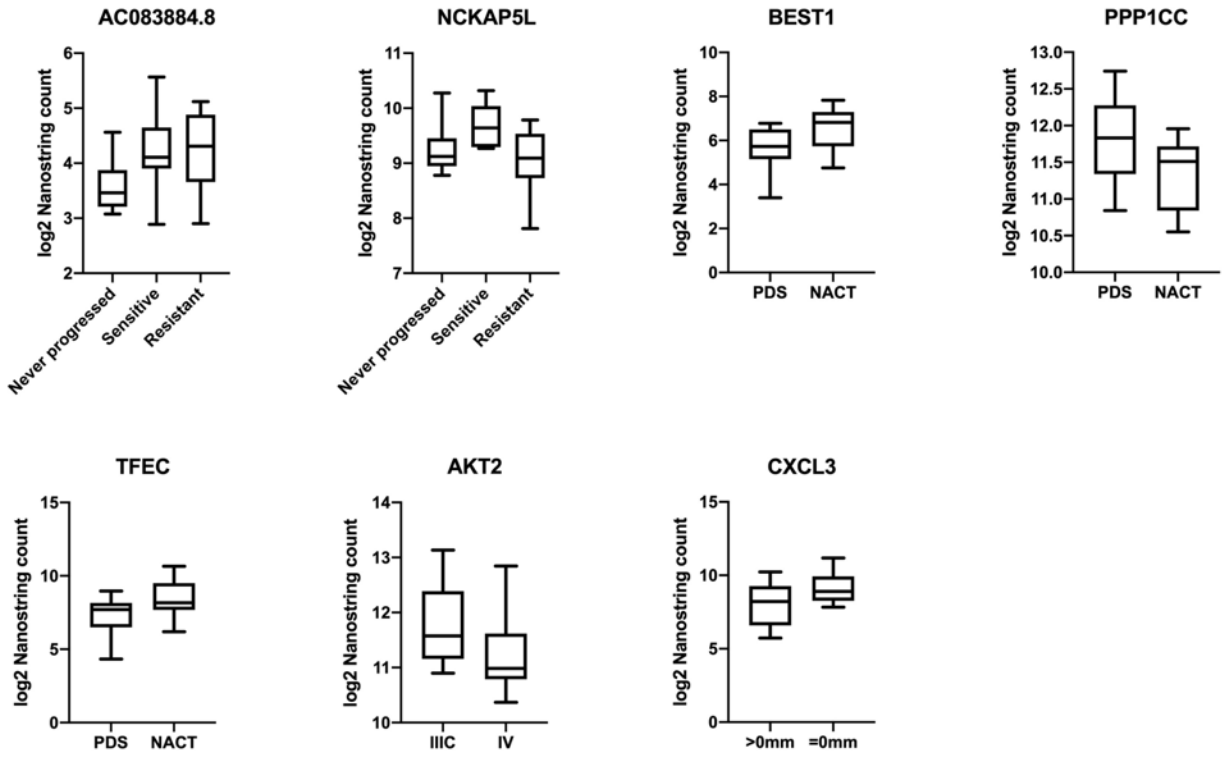

FIGURE 39. Boxplots of genes significantly associated with clinicopathological parameters. PDS = primary debulking surgery; NACT = neoadjuvant chemotherapy; IIIC and IV refer to FIGO stage; >0 mm and 0 mm indicate the extent of residual tumor after first cytoreductive surgery.

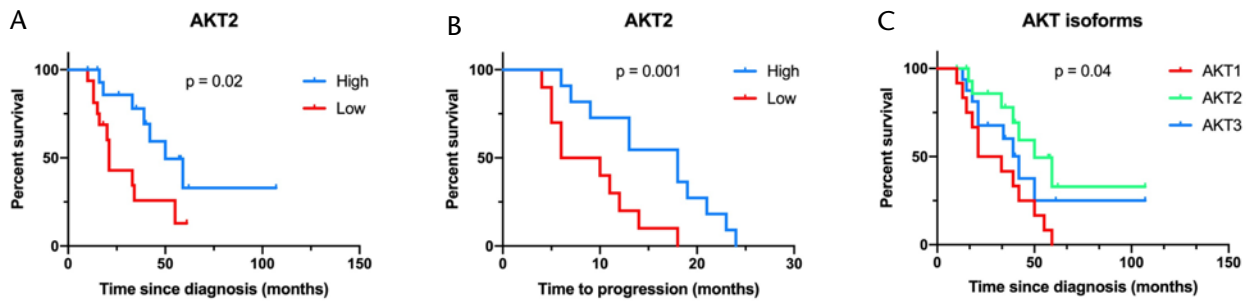

FIGURE 40. AKT2-related OS (A) and PFS (B). AKT isoforms-related OS (C)

4.4.2 RNAscope®

Eighty-seven FFPE peritoneal implants from HGSOC were analyzed by RNAScope. For each implant, RNA expression was evaluated in one to three selected spots in order to detect more accurately tumor heterogeneity. The expression of Cyclin C (CCNC), Cyclin E (CCNE1), human leucocyte antigen B (HLA-B) and WAP Four-Disulfide Core Domain 2 (WFDC2) genes were assessed using the five-level score previously described. Positive expression was detected in 60% of cases for CCNC, 66% for CCNE1, 95% for WFDC2 and 90% of the cases for HLA-B. On average, Cyclins-C and E had lower expression levels in HGSOC, with mean scores of 0.43 and 0.52, respectively, while HLA-B and WFDC2 had higher expression levels (mean value 0.83 and 1.81, respectively). Statistical analysis comparing mean expression of target RNAs with clinicopathological variables showed CCNC scores significantly associated with primary therapy response to platinum agents. Higher expression levels of CCNC were related to patients who never progressed after first line treatments compared to both sensitive (P = 0.007) and resistant groups (P = 0.04). HLA-B expression was significantly higher in patients with FIGO stage IIIC compared to IV (P = 0.02). For WFDC2 a trend toward higher score levels in implants with classic morphology compared to SET was found (P = 0.06) (**Fig. 41**). CCNE1 was not associated to any of the variables considered.

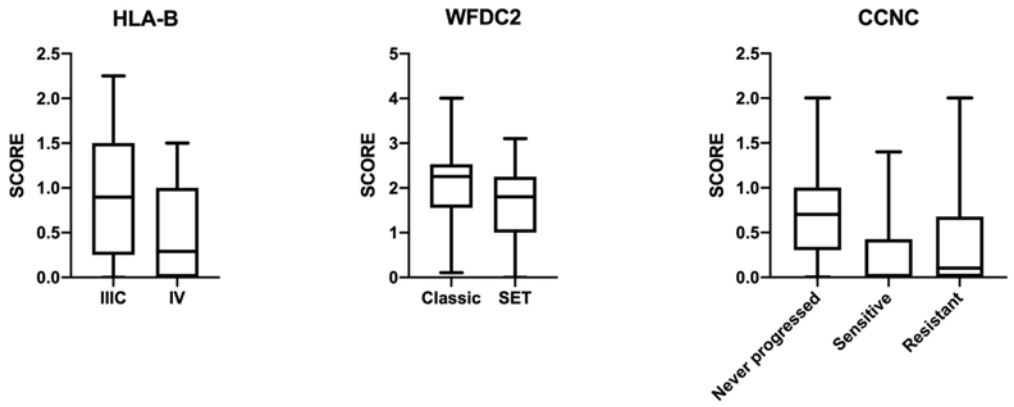

FIGURE 41. Significant association between HLA-B, WFDC2 and CCNC with respectively FIGO stage, tumor morphology and primary platinum response.

Furthermore, CCNC and HLA-B seemed to influence positively overall survival in our cohort (P = 0.01 for CCNC and P = 0.004 for HLA-B) (**Fig. 42**).

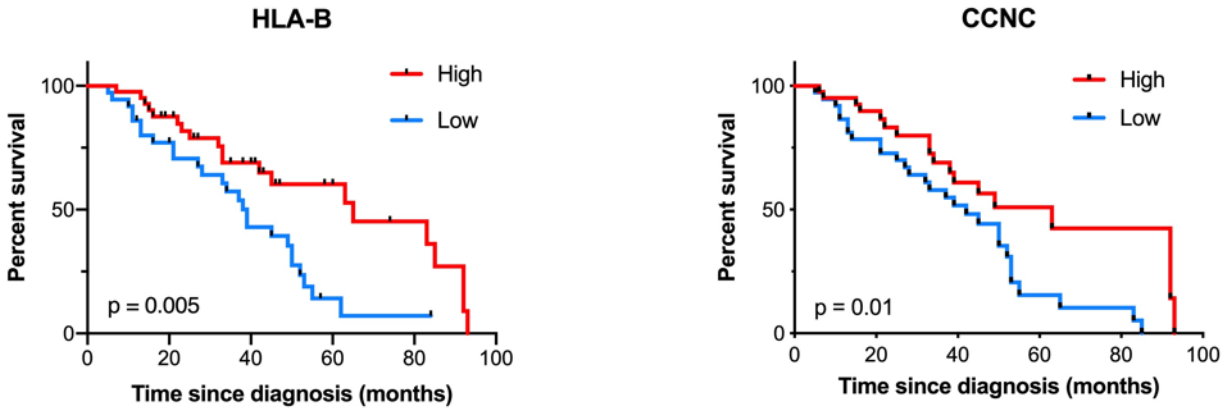

FIGURE 42. Significant association between HLA-B and CCNC scores detected by RNAscope and overall survival.

4.5 Atomic force microscopy

Young's modulus of 19 tissues samples was measured by indentations in one to three different locations within each TMA's tissue spot. HGSOC tissue samples were chosen according to the architectural pattern: in detail, 2 endometrioid-like, 5 micropapillary-like, 5 papillary, 3 solid and 4 transitional-like high grade serous carcinomas were analysed. For each sample, a mean of 141 indentations over the selected locations were performed. Due to tissue morphology, such as in the case of tumors growing in papillae and micropapillae, we cannot avoid performing several indentations in tumor cells near necrotic areas, or at the edge between tumor tissue and underlying glass slide, which can produce biases in tumor stiffness measurements. For this reason, we removed

outlier stiffness values using ROUT (Robust regression and outlier removal) method, before starting the analyses. Stiffness values derived from samples with the same architectural pattern were grouped together and analyzed. The mean elastic modulus, expressed in kPa, was 85 ± 3.3 for endometrioid-like HGSOC, 113 ± 4.4 for transitional-like, 38 ± 2.3 for micropapillary-like, 107 ± 5 for papillary and 136 ± 5.9 for solid HGSOC. Results of t-test comparison between each group showed no differences in the mean elastic modulus between papillary and endometrioid tumors ($P = 0.06$) and between papillary and transitional-like tumors ($P = 0.1$). Nonetheless, a strong difference was found between Young's moduli for all the other architectural patterns ($P < 0.01$) (**Fig. 43**).

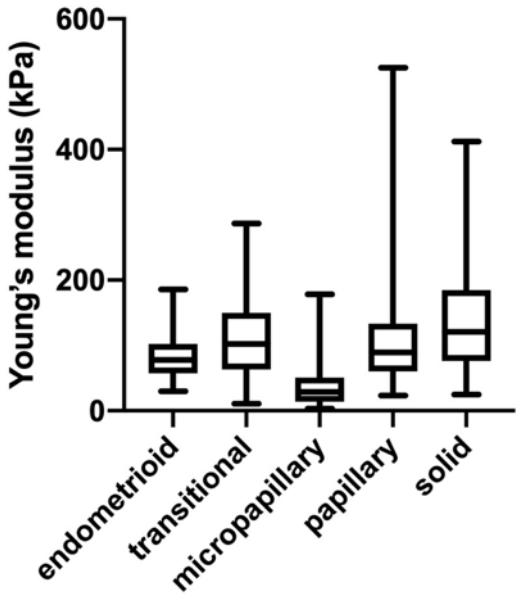

FIGURE 43. Boxplots of Young's moduli for each architectural pattern of high grade serous ovarian carcinoma.

Each morphological pattern was then analyzed for the distribution of elastic moduli. Among the five patterns, solid and transitional displayed a very broad gaussian distribution compared to the other three patterns, with gaussian peaks between 100 and 120 kPa. Endometrioid-like tumors also exhibited a flat distribution of Young's moduli, but gaussian peak was shifted to lower level of stiffness, around 70 kPa. Papillary and micropapillary patterns exhibited almost the same trend, with one gaussian peak centered at lower level of stiffness followed by a gradual decrease toward higher values of Young's moduli. For papillary pattern, the mean peak, which accounted for almost 40% of force values, was centered at 50 kPa while in the case of micropapillary pattern the peak was at 10 kPa, resulting the softest among the morphological patterns. The quantitative analysis of stiffness distribution is presented as histograms in **Fig. 44**.

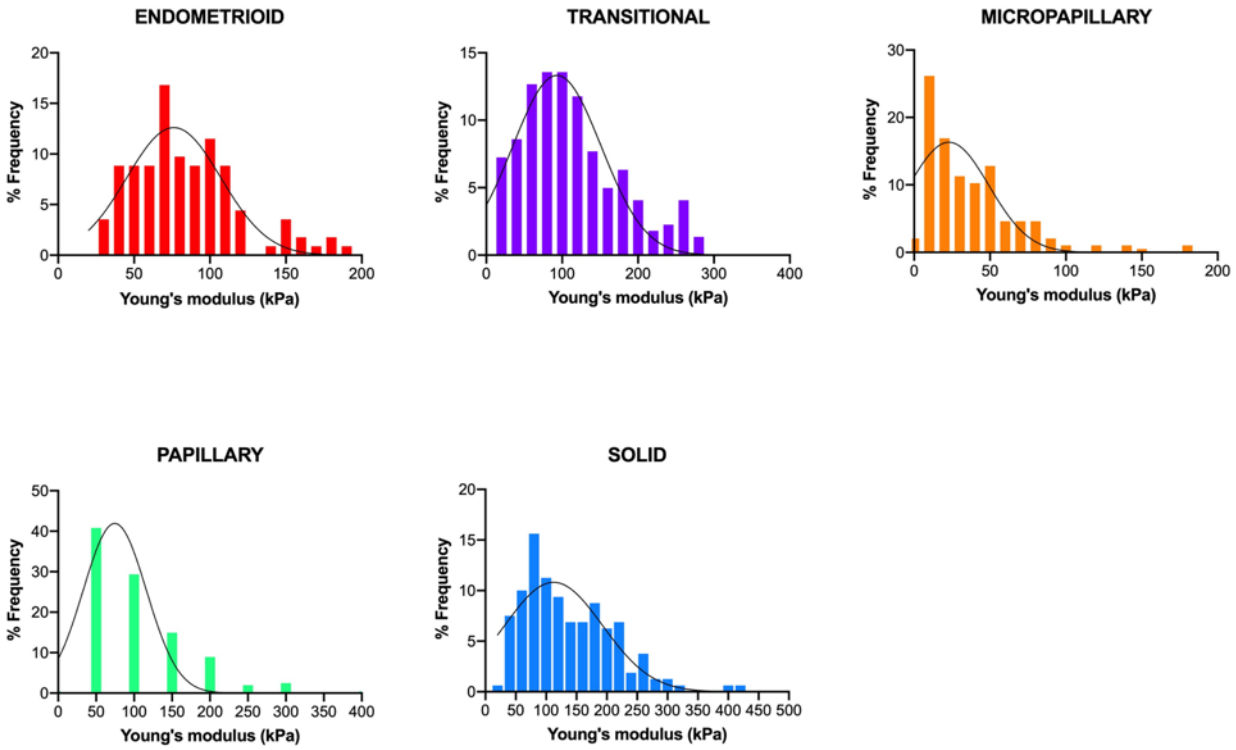

FIGURE. 44 Frequency distribution of stiffness values from AFM measurements among five HGSOC morphological patterns.

In order to relate sample's stiffness with clinicopathological variables the mean Young's modulus of each sample was also calculated. No significant associations between tissue stiffness and overall or progression free survival were found; although samples from patients with FIGO stage IV were softer than those from stage IIIC patients (P = 0.03).

4.6 Molecular analyses – effect of fixation

4.6.1 Yield and purity

Total RNA and miRNA isolated from fifteen pairs of matched samples by Maxwell® RSC, were quantified and assessed for purity using Nanodrop ND 1000. No significant difference with respect to total RNA and miRNA yield was found between formalin and Bouin's specimens ($P = 0.21$), but RNA purity, as defined by and A260/280 ratio, resulted significantly lower in Bouin's group ($P = 0.02$). Also purity by A260/230 ratio was significantly lower in Bouin's samples with respect of total RNA ($P < 0.0001$), but not of miRNA.

4.6.2 Integrity

Agilent 2100 Bioanalyzer was used to generate RNA profiles for formalin and Bouin's matched pairs of samples. Ribosomal peaks, corresponding to the 18S and 28S rRNAs, were lost in both FFPE and Bouin's samples with generally low RIN values (mean RIN = 2.4), which did not differ between formalin and Bouin's fixed samples ($p = 0.3$). The RIN values obtained, although low, are in agreement with those reported in literature by many groups which have performed molecular analyses on fixed and paraffin embedded material [138]. Bioanalyzer outputs were submitted to smear analysis for 5 five smear regions: 1-59, 60-149, 150-299, 300-449, 450-600 nucleotides. The overall size distribution of RNA was similar when comparing electropherograms obtained from formalin and Bouin's samples, with most fragments included in the range of 60 - 300 nucleotides. Nevertheless, RNAs generated from FFPE samples had significant higher number of fragments in the smear regions of 60-149 nt and 150-299 nt ($p = 0.01$ and $p = 0.008$, respectively). The same results were obtained on RNA samples derived from miRNA extraction. The miRNA content was measured as the relative abundance in comparison to the total small RNA fraction and no differences were detected between Bouin's-fixed samples and formalin ones ($p = 0.2$)

4.6.3 Nanostring®

Among the fifteen matched pairs tested for RNA quality and integrity, seven were selected for their good quality by BioAnalyzer, Nanodrop and RT-qPCR analyses, while one pair (385) was selected as it exhibited good quality by Nanodrop and Bioanalyzer platforms, but not by RT-qPCR. Following, the gene expression of the eight matched pairs was analyzed by Nanostring nCounter® using the custom CodeSet used for the validation of HERCULES biomarkers.

Raw and normalized data obtained by NanoString were log2 transformed, and values derived from the eight paired formalin-Bouin's samples were compared in order to determine potential differences

in gene expression between the two groups. The assessment of gene expression was successful for all gene targets in all 16 samples and no quality control or normalization flags were encountered. Differential expression (DE) analysis performed by Nanostring software nSolver, and expressed as log2 fold change, returned no differences between the two fixatives after Benjamini-Yukutieli correction. Without adjusting the p-value, six transcripts (KLF16_b, ZNF444, KLF16, INTS5, ITGA5, COL6A1_b) were found being highly expressed in Bouin's compared to formalin (**Fig. 45**).

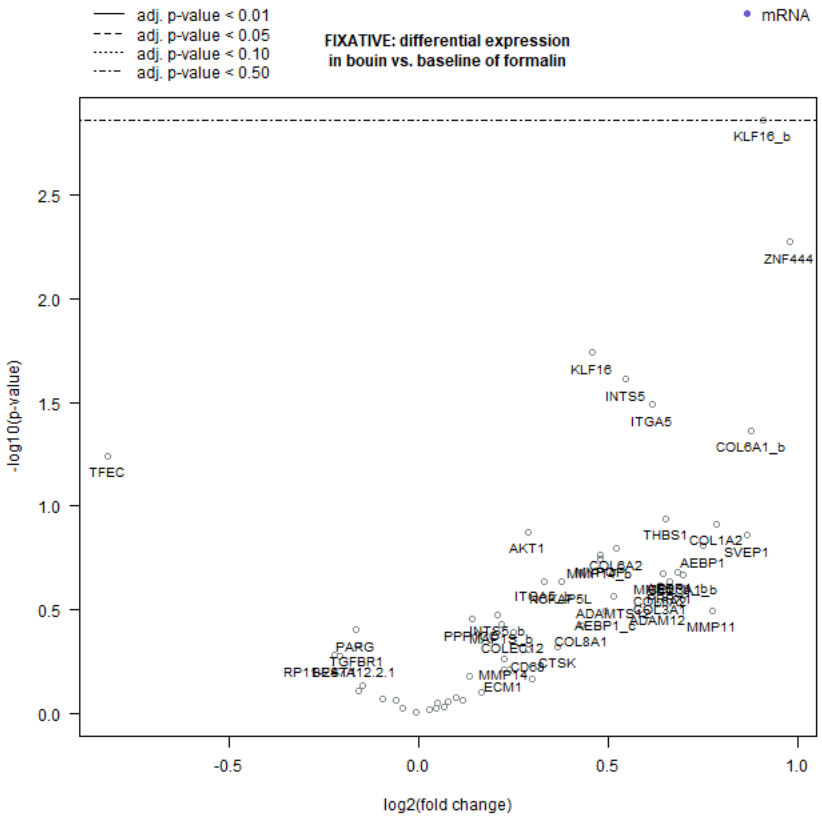

FIGURE 45. Volcano plot of differentially expressed (DE) genes identified by nSolver analysis.

To further investigate on that result, as nearly 40% of adenines are reported to acquire monomethylol addition after fixation with formalin [93], we hypothesized that the difference in the total signal counts of the six differentially expressed gene elements identified by nSolver analysis could be related to higher content of modified adenines in the target RNA sequences in formalin tissues. As a consequence, Nanostring probes should bind with more efficiency to RNA of Bouin-fixed specimens. To verify our hypothesis, we calculated the adenine content in the target RNA of the top twenty differentially expressed genes identified by nSolver. The resulted analysis showed a trend ($p = 0.08$) toward a higher percentage of adenines content in the six gene elements that were differentially expressed in the two fixatives (**Fig. 46**).

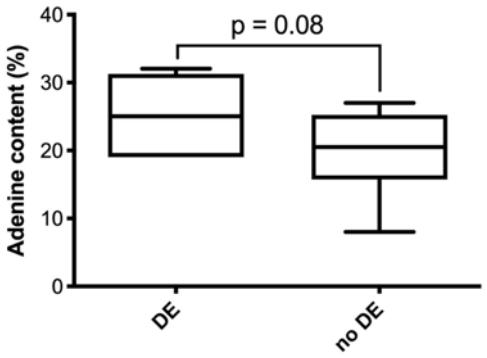

FIGURE 46. Boxplot of adenine content in differentially expressed genes (DE) and no differentially expressed genes (no DE) identified by nSolver analysis.

A Spearman rank test between normalized data of matched pairs was also calculated for each target and the resulting coefficients are plotted on the histogram shown in **Fig**. **47** The mean gene-wise correlation was 0.45, with a minimum value of 0.21 and a maximum of 0.88, indicating a medium level of concordance between formalin and Bouin's group. Among the transcripts analyzed, eight (ATP1A1-AS1, CD68, COL6A1_b, COL6A2, KDM4A-AS1, PARG, RP11-247A12.2.1) were significantly correlated between the two fixatives while three (ITGA5_b, AKT2, AC083884.8) had a p-value slightly higher than the threshold of significance.

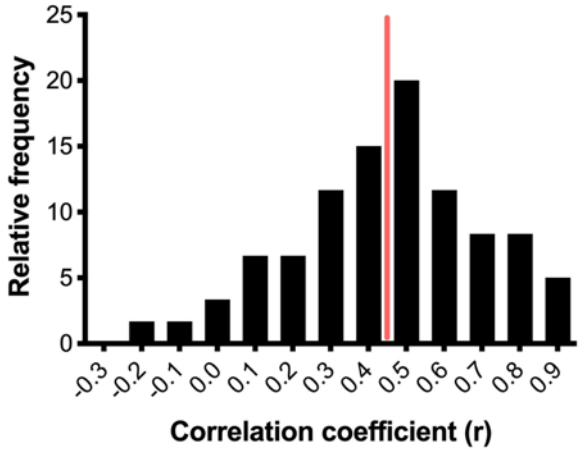

FIGURE 47. Histogram of gene-wise correlation with mean correlation reported as a red line.

In order to validate Nanostring results with RT-qPCR and ddPCR, the transcripts levels of GAPDH, ACTB, AKT1 and KLF16 were retrieved from raw data counts and compared in formalin and Bouin's material. The results showed that RNA expression in the two fixatives were significantly different for AKT1 (P = 0.04), borderline for GAPDH (P = 0.05) and for ACTB (P = 0.06) and no significant for KLF16 (P = 0.37). A Spearman analysis was also performed, but it resulted in no significant correlation between formalin and Bouin-fixed tissues for any of the genes analyzed. Rho coefficients

were: 0.21 (P = 0.6) for ACTB, 0.34 (P = 0.4) for GAPDH, 0.35 (P = 0.4) for AKT1 and 0.13 (P = 0.8) for KLF16.

4.6.4 RT-qPCR

mRNA

Gene expression analysis was performed by RT-qPCR using GAPDH, ACTB, AKT1 and KLF16 genes in order to validate Nanostring results. Along with these targets, ERR marker gene was analyzed as well for its reported resistance to RNAses activity.

Overall, the expression level of the five genes was higher in formalin-fixed compared to Bouin's matched samples for every stretch analyzed. In particular, paired t-test on the four amplicon lengths used to validate Nanostring results, returned a p-value of 0.008 for ACTB (95 bp) and GAPDH (100 bp), 0.005 for AKT1 (77 bp) and 0.02 for KLF16 (77 bp) (**Fig. 48**), while in the case of ERR marker gene at 100 bp and 200 bp, the p-values were respectively 0.003 and 0.004.

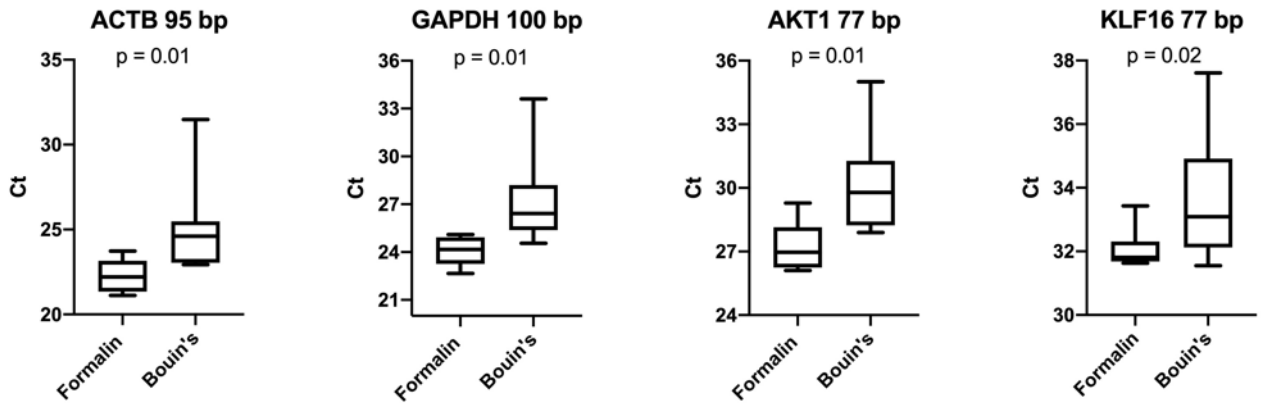

FIGURE 48. Boxplots representing RT-qPCR in matched formalin/Bouin's samples for the four gene lengths used to validate Nanostring results.

We also analyzed the correlation between formalin and Bouin's tissues in ACTB (95 bp), GAPDH (100 bp), AKT1 (77 bp) and KLF16 (77bp) stretches, but Pearson's did not return any significant results. Rho values were 0.60 (p = 0.16) for ACTB, 0.43 (P = 0.30) for GAPDH, 0.63 (P = 0.13) for AKT1 and 0.71 (P = 0.06) for KLF16, respectively.

Using the same amount of RNA in each assay, ΔAMP analysis showed a significant difference between the two fixatives for all differential amplicons of GAPDH and ERR marker genes, with ΔAmp values notably higher in RNA samples isolated from Bouin's material, but not for ACTB. In addition, ΔAmp in the two groups increased with increasing difference of amplicon lengths, suggesting the increment in RNA degradation.

miRNA

Real-time PCR was successful in all 30 samples for all miRNAs analyzed. The expressions of let-7e-5p, miR-423-3p, and miR-92a-1-5p were closely comparable in FFPE and matched Bouin's specimens (P = 0.3, p = 0.5, and P = 0.9, respectively) but significant differences were found for miR-30d-5p (P = 0.04), miR-155-5p (P = 0.03), miR-200a-3p (P = 0.04), and miR-429 (P = 0.01), where Bouin's-fixed samples exhibited higher Ct values (**Fig. 49** and **Fig. 50).** Moreover, pairwise Spearman's rank analysis showed a significant correlation between formalin and Bouin's specimens for miR-423-3p (P = 0.003), miR-92a-1-5p (P = 0.0002), miR-30d-5p (P = 0.01) and miR-200a-3p, but not for let-7e-5p (P = 0.8) or miR-155-5p (P = 0.4).

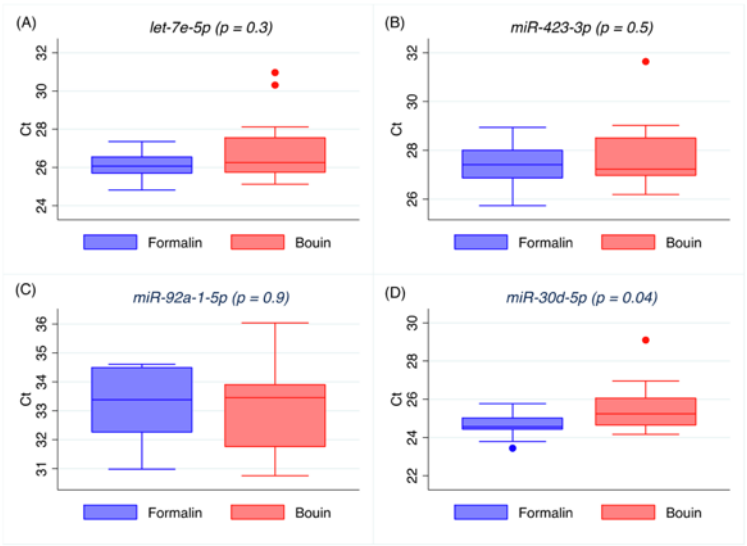

FIGURE 49. Boxplots representing RT-qPCR in matched formalin/Bouin's samples for let-7e-5p (A); miR-423-3p (B); miR-92a-1-5p (C); miR-30d-5p (D).

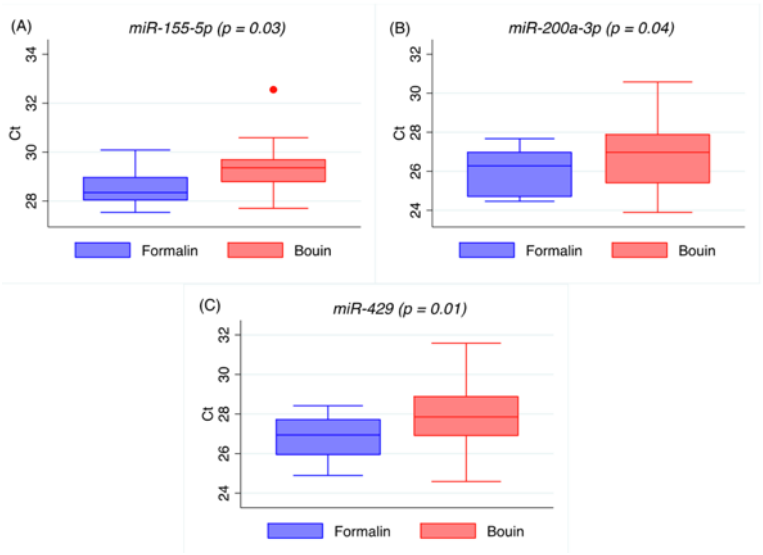

FIGURE 50. Boxplots representing RT-qPCR in matched formalin/Bouin's samples for miR-155-5p (A); miR-200a-3p (B); miR-429 (C).

4.6.5 Droplet digital PCR

mRNA

The expression levels of GAPDH (100 bp), ACTB (95 bp), AKT1 (77 bp) and KLF16 (77 bp) were further validated by ddPCR using the log2 nominal copies/µl at 24 ng (ACTB and GAPDH) and 70 ng (AKT1) of cDNA input obtained from each sample using the standard curve method. Comparing mRNAs expression in formalin and Bouin's fixed samples, a significant difference between the two groups was found for GAPDH ($P < 0.008$), ACTB ($P = 0.008$), AKT1 ($P = 0.008$) and KLF16 ($P = 0.008$) as shown in **Fig. 51**. The expression of KLF16 in one degraded sample fixed in BS (385) was too low for being detected at 24 ng of total RNA input, therefore linear model returned a negative absolute count. For GAPDH the median log2 copies/µl was 9.1 in formalin fixed samples and 6.6 in Bouin's fixed, for ACTB was respectively 10.5 and 8.3, for AKT1 9.6 in formalin and 7.5 in Bouin's and for KLF16 2.3 and 0.92 in formalin and Bouin's respectively. Pairwise Pearson's analysis showed no significant correlation between matched pairs for all the four genes analyzed.

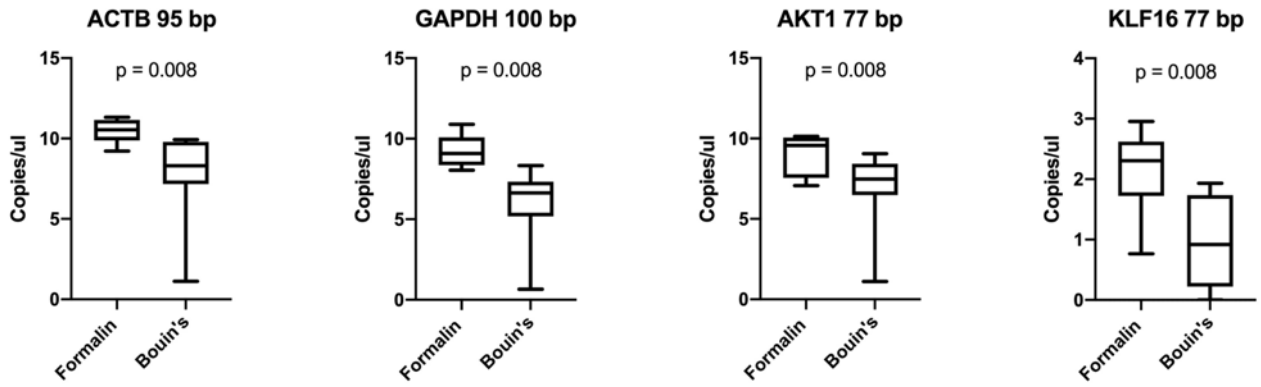

FIGURE 51. Boxplots representing droplet digital PCR quantification in matched formalin/Bouin's sampels for the four gene lengths used to validate Nanostring results. Only ther positive values of sample 385 fixed in Bouin's were included in KLF16 77 bp boxplot.

miRNA

The expression of the seven miRNAs was further assessed by ddPCR. Comparing miRNA expression in formalin- and Bouin's-fixed samples, we found a significant difference in expression between the two groups for let-7e-5p (P = 0.04), miR-30d-5p (P= 0.0004), miR-155-5p (P = 0.02), and miR-429 (P = 0.03), but not for miR-423-3p (P = 0.09), miR-92a-1-5p (P = 0.4), or miR-200a-3p (P = 0.09), as shown in **Fig. 52** and **Fig. 53**. Pairwise correlation analysis was significant for miR-92a-1-5p (P = 0.007), miR-30d-5p (P = 0.005), miR-200a-3p (P = 0.008) and miR-429 (P = 0.01), but not for the other miRNAs analyzed.

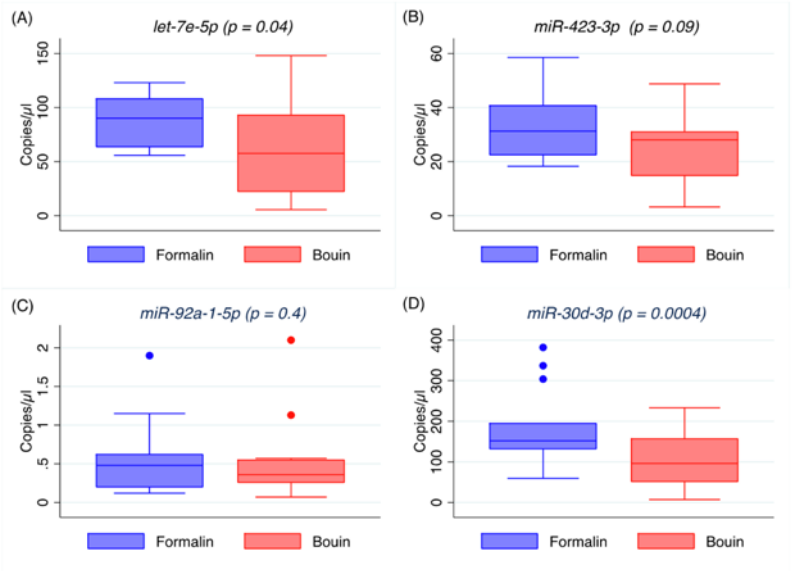

FIGURE 52. Boxplots representing ddPCR quantification in matched formalin/Bouin's samples for let-7e-5p (A); miR-423-3p (B); miR-92a-1-5p (C); miR-30d-5p (D).

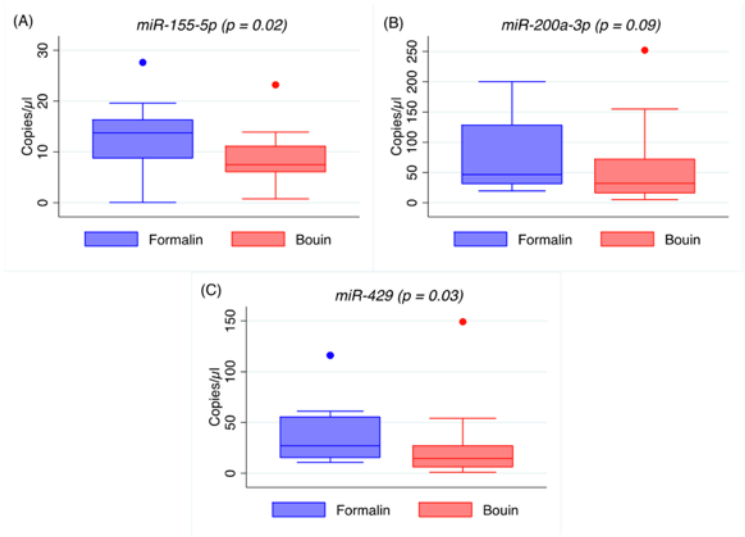

FIGURE 53. Boxplots representing ddPCR quantification in matched formalin/Bouin's samples for miR-155-5p (A); miR-200a-3p (B); miR-429 (C).

4.6.6 RT-qPCR and ddPCR data normalization

mRNA

In order to evaluate if the expression levels of AKT1 and KLF16 on RT-qPCR and ddPCR were comparable in formalin and Bouin's group after normalization, the geometric mean of the housekeeping genes ACTB and GAPDH, was used as reference. Moreover, ERR marker 100 bp expression was also evaluated after RT-qPCR normalization for its high expression. Normalized formalin and Bouin's ratios were submitted to paired t-test and no differences were detected between

the two groups only for AKT1 and ERR marker gene on RT-qPCR platform (P = 0.08 and P = 0.8 respectively), while KLF16 expression was significantly different after normalization in both RT-qPCR and ddPCR (p = 0.01 and p = 0.008 respectively) (**Fig. 54**). The same analysis made excluding the highly degrade sample fixed in Bouin's (385), gave the same results.

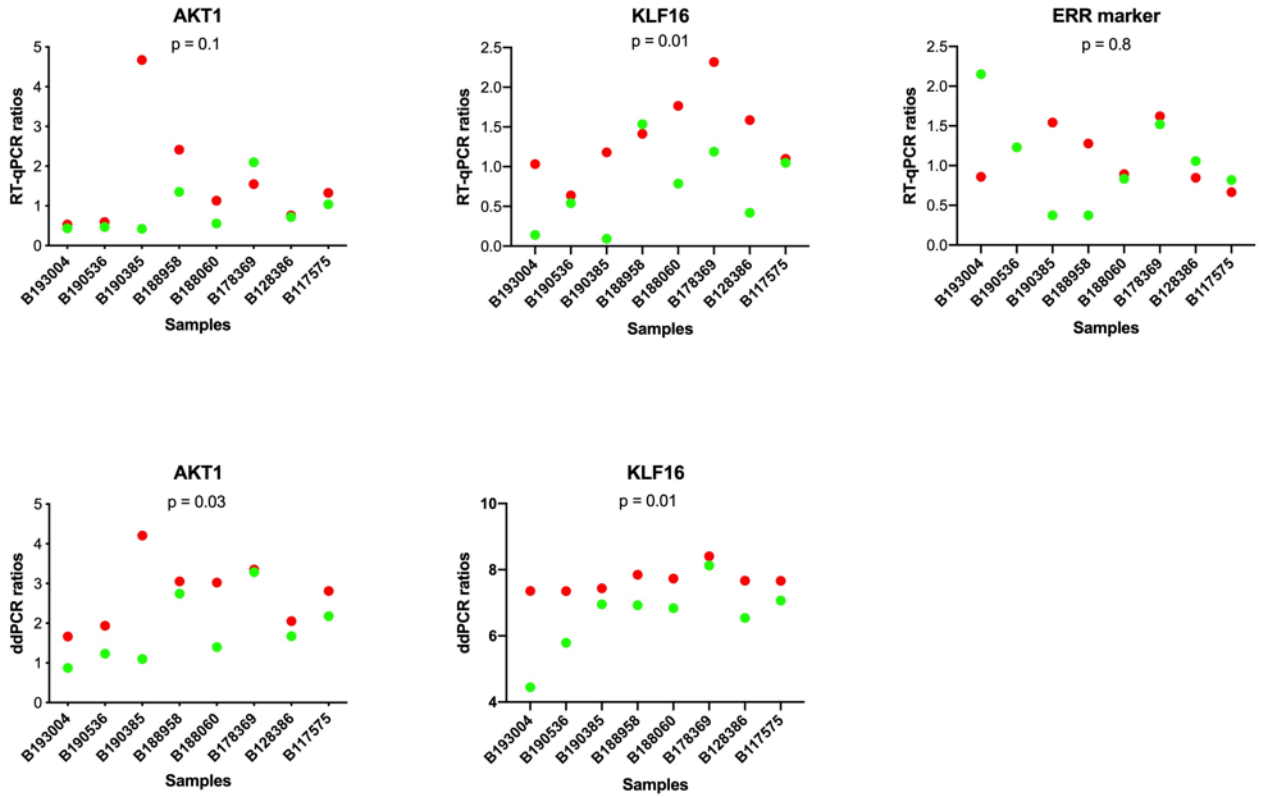

FIGURE 54. Scatterplots of RT-qPCR ratios (above) and ddPCR ratios (below) for AKT1 77 bp, KLF16 77 bp and ERR marker 100 bp in matched formalin/Bouin's samples. Red dots = Bouin's samples; Green dots = formalin samples.

miRNA

In order to normalize qRT-PCR data, the geometric mean of the most stable miRNAs, namely let-7e-5p and miR-423-3p, was used as reference miRNA. Normalized qRT-PCRs were submitted to Wilcoxon's matched-pairs signed-ranks test, which did not return any significant difference between formalin and Bouin's ratios as shown in **Fig. 55**.

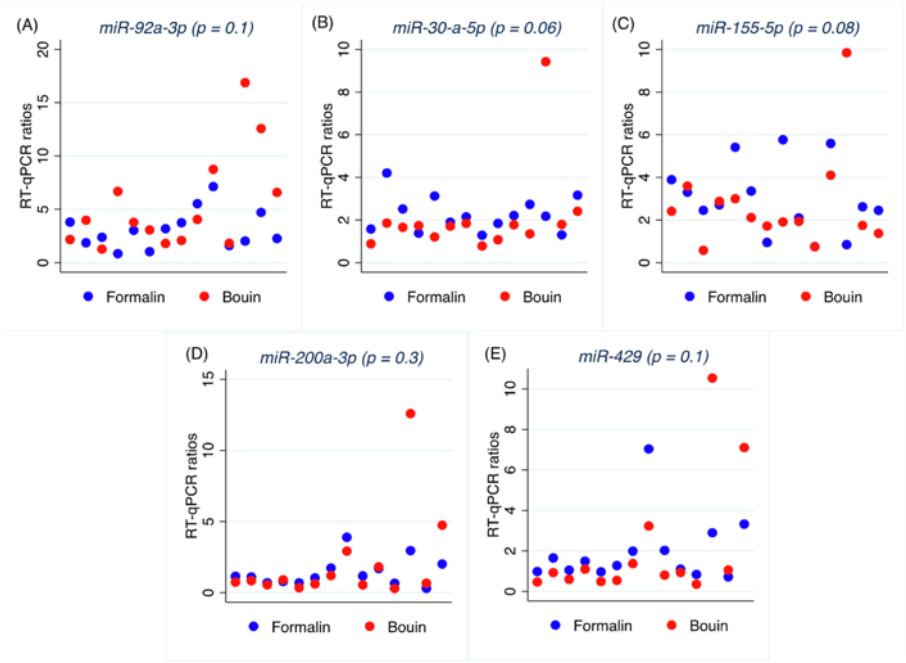

FIGURE 55. Scatter plot of real-time RT-qPCR ratios for miR-92a-1-5p (A), miR-30d-5p (B), miR-155-5p (C), miR-200a-3p (D), and miR-429 (E) in formalin- and Bouin's-fixed tissues.

4.6.7 Nanostring® vs ddPCR

The standard curves obtained from each sample by ddPCR were used also to compare the platform with Nanostring. The ddPCR log2 nominal copies/µl at 300 ng for GAPDH, ACTB, AKT1 and KLF16 genes were obtained by interpolation from the standard curves for each sample and compared with the respective log2 transformed copies obtained by Nanostring raw data at the same amount of RNA input.

Overall, the results obtained showed that nominal copies obtained by ddPCR were lower compared to those detected by Nanostring at the same quantity in both formalin and Bouin's groups. With respect to GAPDH gene, the linear regression analysis gave a significant correlation between the two platforms in both fixatives. The R-square value was 0.82 in formalin group ($p = 0.002$) and 0.74 in Bouin's ($p = 0.006$). Similarly, for ACTB the correlation between ddPCR and Nanostring was 0.53 ($p = 0.04$) in formalin and 0.84 ($p = 0.001$) in Bouin's material. With regard to AKT1 gene, linear regression analysis returned no correlation between the two platforms in formalin fixed tissues, but in Bouin's material a significant level of concordance was found. The R-square value was 0.22 ($p = 0.24$) in formalin samples and 0.59 ($p = 0.03$) in Bouin's. Conversely, for KLF16 Bouin's samples no correlation was detected between the two platforms, but formalin samples were significantly correlated. The R-square was 0.16 ($p =0.33$) in Bouin's material and 0.50 ($p = 0.05$) in formalin. Regression curves are reported in Fig.

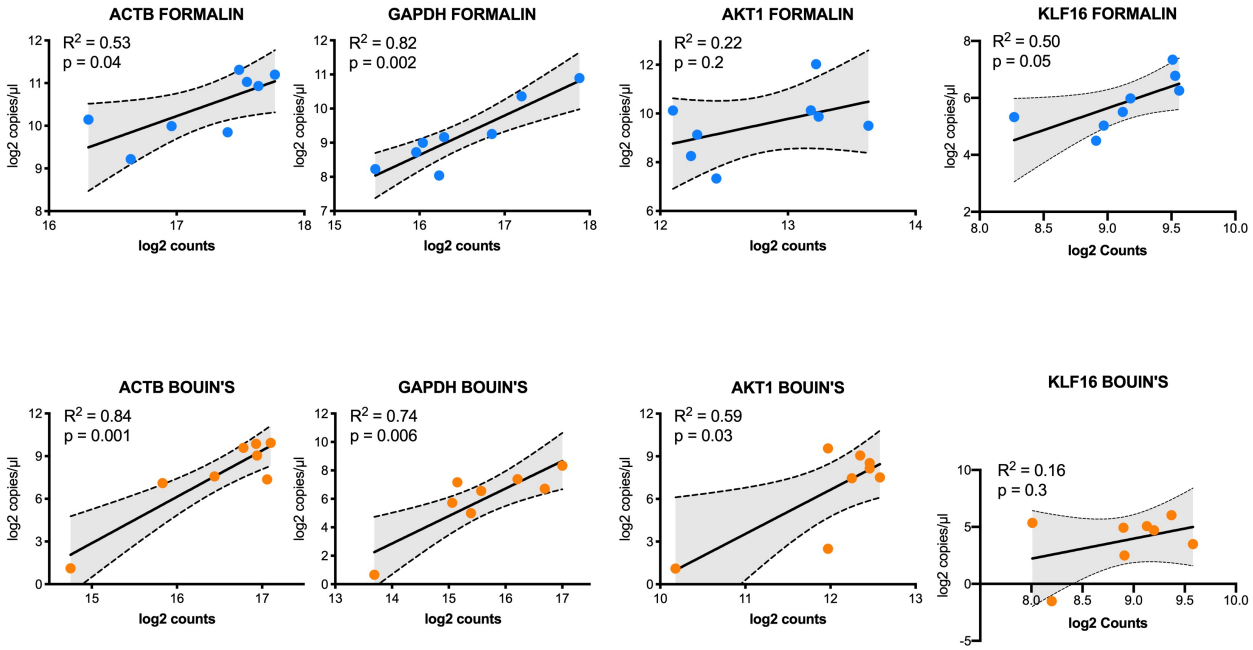

FIGURE 56. Scatter plot and linear prediction with 95% confidence interval of Nanostring and ddPCR results for ACTB, GAPDH, AKT1 and KLF16 in formalin (above) and Bouin's-fixed tissues (below).

4.6.8 RT-qPCR vs ddPCR

mRNA

In order to compare data obtained by qRT-PCR and ddPCR, for each sample the Ct values were compared with the nominal log2 copies/µl using the same amount of cDNA. The comparisons were made by the use of the linear regression model and Pearson's correlation test for both formalin and Bouin's fixed specimens. A strong correlation between qRT-PCR and ddPCR was found for ACTB and GAPDH genes in both fixatives, but for AKT1 a significant correlation was found only in Bouin's fixed samples (**Fig. 57**). The regression coefficient for ACTB amplicon of 95 bp was 0.93 in formalin fixtive ($p = 0.0001$) and 1 in Bouin's ($p < 0.0001$), similarly for GAPDH amplicon at 100 bp the coefficient was 0.92 in formalin ($p < 0.0001$) and 1 in Bouin's ($p < 0.0001$). For AKT1, the regression coefficient was 0.37 ($p = 0.11$) for formalin samples and 0.84 for BS samples ($p = 0.001$). With regard to KLF16, for both formalin and Bouin's samples a significant correlation was found between the two platforms, having R-square of respectively 0.81 ($P = 0.002$) and 0.84 ($P = 0.001$).

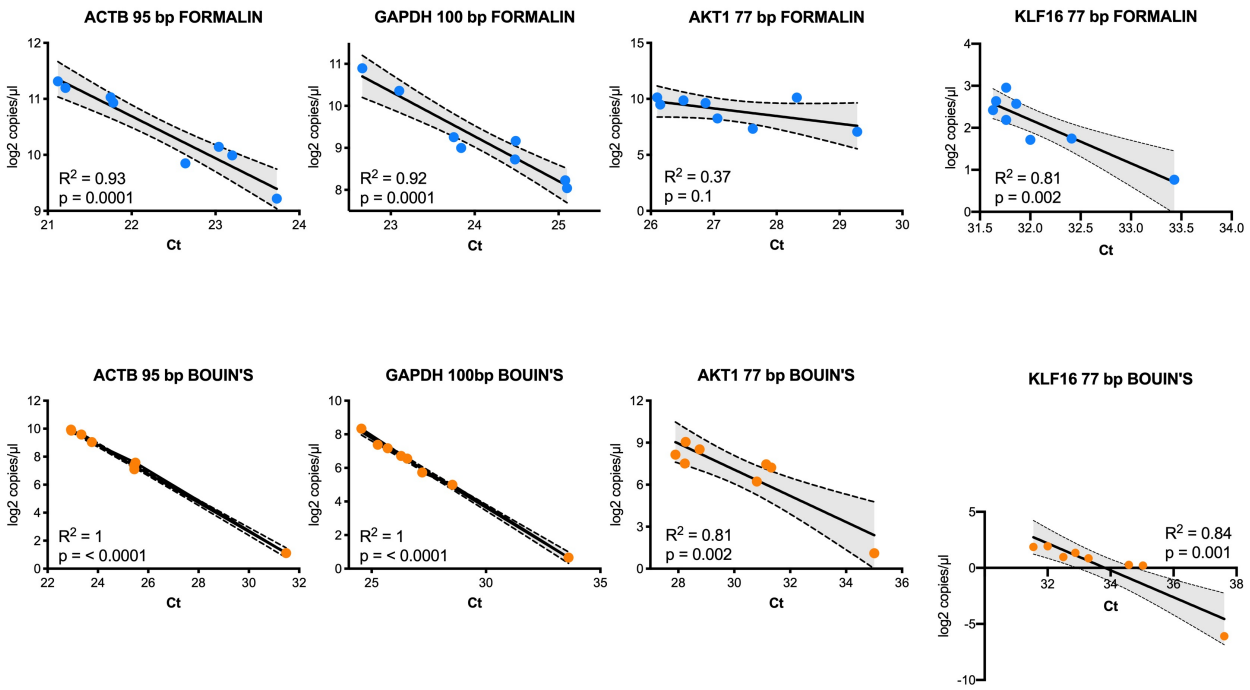

FIGURE 57. Scatter plot and linear prediction with 95% confidence interval of real-time and ddPCR results for ACTB, GAPDH, AKT1 and KLF16 in formalin (above) and Bouin's-fixed tissues (below).

miRNA

In order to correlate qRT-PCR and ddPCR measurements, the same amount of cDNA (0.4 ng) was submitted to PCR in each assay on both platforms. The resulting data, expressed as cycle (Ct) and the log2 of the number of target copies/µL, were compared by linear regression for both formalin- and Bouin's-fixed samples. Our results clearly show that there is a linear correlation between ddPCR results and real-time PCR for both formalin- and Bouin's-fixed samples regarding miR-92a-1-5p, miR-30d-5p, miR-200a-3p, and miR-429. For let-7e-5p, miR-423-3p, and miR-155-5p, real-time and ddPCR results were significantly correlated only in Bouin's-fixed samples. Linear regression analysis produced a R-square value of 0.46 ($P = 0.005$) for let-7e-5p, 0.91 ($P < 0.0001$) for miR-423-3p, and 0.9 ($P < 0.0001$) for miR-155-5p in Bouin's fixed tissues. Similarly, results from qPCR and ddPCR for miR-92a-1-5p were significantly correlated in both formalin- ($P = 0.01$) and Bouin's-fixed tissues ($p = 0.0002$). These results were also confirmed for the other microRNAs analyzed in this study (**Fig. 58 - 61**).

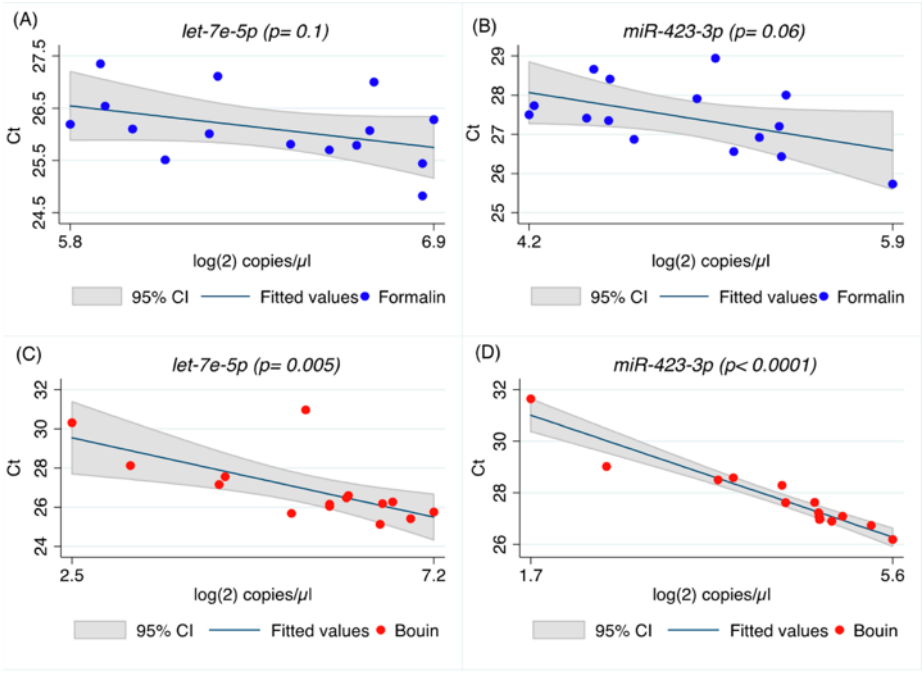

FIGURE 58. Scatter plot and linear prediction with 95% confidence interval of real-time and ddPCR results for let-7e-5p and miR-423-3p in formalin- (A, B) and Bouin's-fixed tissues (C, D), respectively.

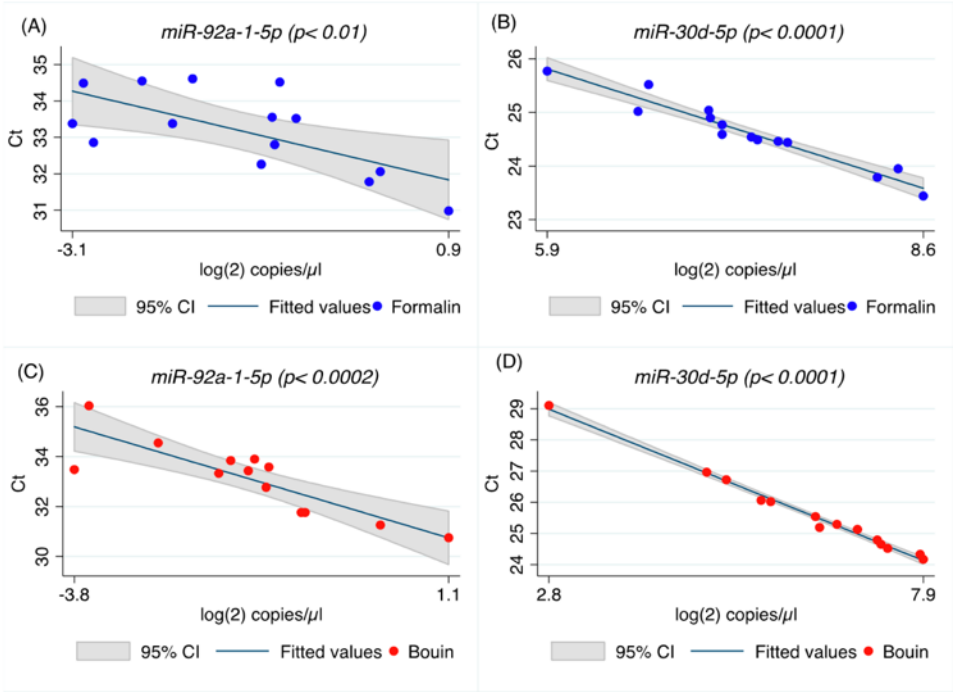

FIGURE. 59 Scatter plot and linear prediction with 95% confidence interval of real-time and ddPCR results for miR-92a-1-5p and miR-30d-5p in formalin- (A, B) and Bouin's-fixed tissues (C, D)

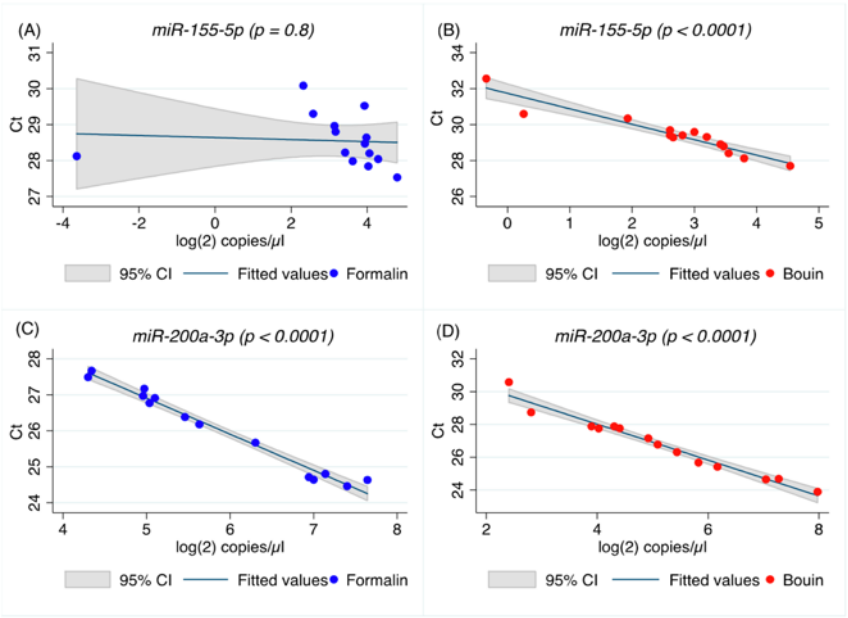

FIGURE 60. Scatter plot and linear prediction with 95% confidence interval of real-time and ddPCR results for miR-155-5p and miR-200a-3p in formalin (A, B) and Bouin's (B, D) fixed tissues.

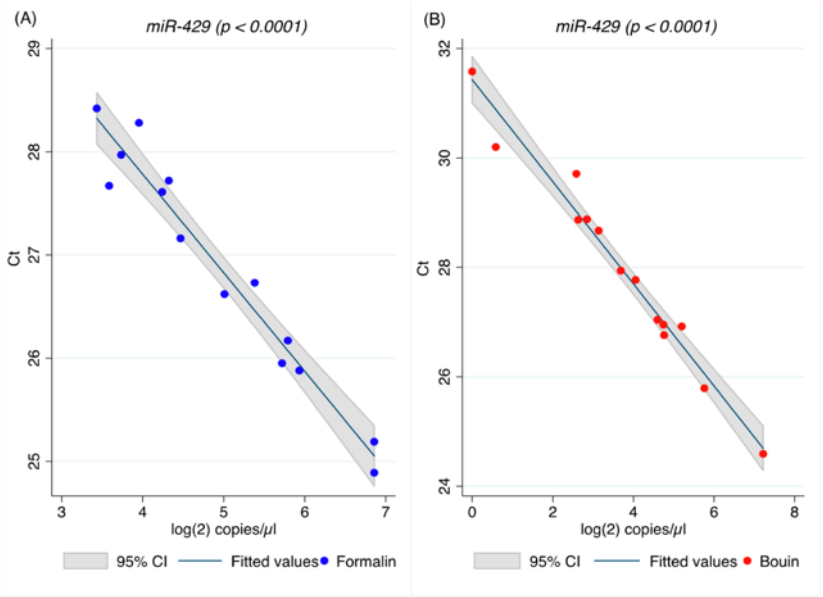

FIGURE 61. Scatter plot and linear prediction with 95% confidence interval of real-time and ddPCR results for miR-429 in formalin (A) and Bouin's (B) fixed tissues.

4.6.9 Measurement of RT efficiency

As previously showed, the results obtained from qRT-PCR and ddPCR pointed out that expression levels of GAPDH, ACTB, AKT1 and KLF16 were constantly lower in Bouin's samples compared to formalin. To investigate whether this difference was related to the higher degradation of RNA in Bouin's fixative or to an inefficient cDNA synthesis, we measured the amount of cDNA generated by reverse transcription starting from the same amount of input RNA derived from five matched formalin/Bouin's samples. The results clearly showed a lower amount of cDNA from Bouin's fixed samples. The mean cDNA generated was significantly higher in formalin samples compared to those fixed in BS ($p = 0.003$) (**Fig. 62**) although a significant and good correlation was found between the amount of cDNA generated from matched tissues (Pearson's $r = 0.87$; $p = 0.045$).

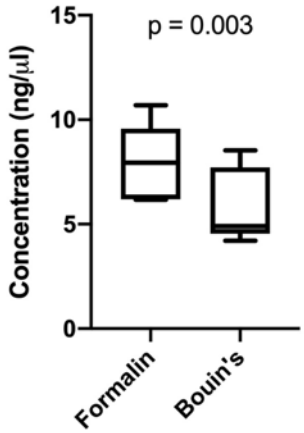

FIGURE 62. Boxplot representing RNA concentration measured with Quantus™ fluorometer after reverse transcription, in formalin and Bouin's samples.

5 DISCUSSION

Although at low incidence, high grade serous ovarian cancers (HGSOC) are the deadliest form of gynaecological malignancy, with 295.000 new cases diagnosed annually worldwide and 185.000 related deaths [3]. The 5-year survival for high grade serous carcinomas is approximately 40% and hasn't significantly changed over the past twenty years. These tumors are difficult to detect in early stage and thus diagnosis is frequently performed when tumor has already spread in the peritoneal cavity. Currently, the standard treatment consists on primary debulking surgery followed by six cycles of platinum-based chemotherapy, but its efficiency is lower than 20% of patients. Nevertheless, although in almost 80% of women the disease recurs and patients eventually die within five years, some patients have significantly better outcomes [2, 79, 139]. HERCULES is a research project founded by the European Horizon 2020 program with the aim to comprehensive characterize HGSOC tumor subpopulations, identifying those resistant to chemotherapy and selecting the proper combinatorial therapy to control tumors. As participant group of this project, our goal is to validate in a retrospective cohort of fixed and paraffin embedded HGSOC tissues, the prognostic and predictive biomarkers identified within the HERCULES project. As commonly known, fixed and paraffin embedded material is broadly available in hospitals and repositories and constitutes an important resource for cancer research; nevertheless, pre-analytical processes and in particular fixation lead to the degradation of biomolecules rendering this type of material hardly suitable for molecular analyses [140]. The aim of this thesis is to validate the biomarkers retrieved within the HERCULES project in a retrospective cohort of HGSOC archive tissues evaluating also the effects of fixation in this type of material as well as its suitability for molecular analyses, in particular for RNA expression.

5.1 Morphological, immunohistochemical and biomechanical analyses

In our cohort of study, clinicopathological parameters were retrieved for 294 HGSOC patients. Among the clinical features analyzed, the mean age at diagnosis (59 years), the median progression-free and overall survival, the relative frequency of patients progressing after first line treatment as well as the response to platinum-based chemotherapy were in agreement with those reported in many epidemiological studies on HGSOC [37, 141-143]. According to our results, higher FIGO stage (stage IV), suboptimal primary cytoreduction and high blood levels of both CA125 (>301 U/ml) and LDH (>326 U/l) were all associated with worse outcome. These data are in line with those reported in literature and they constitute consolidated and commonly shared evidences in HGSOC. Instead, the effect of other clinical parameters such as surgical strategy (PDS vs NACT) and secondary surgery are still now a matter of contention in the scientific community. Our results clearly showed a dramatic

decrease in OS in patients treated with neoadjuvant chemotherapy compared to simple primary debulking surgery. This is in disagreement with data reported by Kehoe *et al.[27]*and Vergote *et al*.[28] where no significant differences were observed between the two strategies. Nevertheless, the decrease in OS in NACT patients of our cohort is partially supported by the significant association found between the number of mitoses and progression to primary chemotherapy and between expression level of Ki67 and PFS, discussed later on in this thesis. In our cohort, slow growing tumors seemed to be more resistant to standard chemotherapy agents and therefore we can speculate that the use of neoadjuvant chemotherapy can favor the selection of aggressive tumor subpopulation with low rate of proliferation. With regard to the clinical usefulness on secondary debulking surgery, our results agree with those obtained by Gockley *et al*. [36] by which secondary cytoreduction confers better OS, although our data are based on the survival of only 50 patients undergoing secondary debulking.

Besides clinical parameters, we showed that also a detailed morphological characterization of HGSOC tumors can be of prognostic and predictive significance. In our analysis of 884 H&E slides, we divided tumors having SET features from those having Classic features based on the classification proposed by Soslow and colleagues [51] and then we correlated the two groups with histocytological parameters, such as the number of mitoses and lymphocytes, the presence of giant cells or atypical mitoses and the presence or not of TILs in tumor epithelium. In addition, we further stratified Classic tumors considering micropapillary pattern as a single entity, since for other type of cancers, such breast, this particular morphology has been associated with a more aggressive behavior [135]. Based on our results, the morphological subdivision in SET and Classic tumor is of relevant importance in determining cancer behavior and response to treatment and therefore they should be considered as two different entities in HGSOC spectrum. Compared to Classic features, SET tumors have higher number of mitoses, higher number of lymphocytes (especially those infiltrating tumor epithelium) and lower BRCA1 H-score. Moreover, these tumors are characterized by having a relevant amount of atypical mitotic figures as well as a lower frequency of psammoma bodies. At prognostic and predictive level, the presence of SET morphology in our cohort was associated with better outcome since patients with higher level of SET features didn't progress after primary chemotherapy. Even a higher number of mitoses (> 21 x 10 HPF), a feature of SET tumor, were significantly associated with primary platinum response and this further confirms the important role of tumor morphology in prognosis. Survival curve analysis, instead, displayed how, in patients with SET tumors, significant better outcomes were achieved only in women submitted to primary debulking surgery and not those treated with NACT. It's reasonable to think that one of the main effects of NACT treatment, the decrease of mitotic activity, lead also to the loss of sensitivity of SET tumors against chemotherapy, with consequent no improvement in overall survival. As previously mentioned, we also analyzed

micropapillary pattern as a single group of tumors and compared it with both Classic and SET features, but we didn't detect any significant difference in both OS and PFS, although patients with micropapillary pattern had worse outcome. Interestingly, we found that, among the three groups, micropapillary tumors had significant lower number of mitoses, a particular feature that we suppose favoring tumor aggressiveness and progression because an improved stemness. This point was also supported by our results on atomic force microscopy. The biomechanical characterization of cell stiffness in each architectural pattern, identified micropapillary-like tumors as those with the lowest Young's modulus of lower stiffness, a feature associated in several studies with higher metastatic potential [111-113].

Among the 884 tissues samples of our case study, 373 derived from 187 patients were also characterized at immunophenotypical level using a panel of seven biomarker: p53, p16, WT1, Ki67, PR, HNF1β and BRCA1. Our IHC results confirmed that high expression levels of p53, p16, WT1 and Ki67 are characteristic features of HGSOC. Overall, the frequency of positive cases and the distribution of staining patterns detected for each biomarker were in agreement with those reported by other authors [144] and, additionally, our panel in association with morphological analysis has proven to be a useful tool in identifying cases that were not HGSOC. As shown by staining pattern analysis, around 30 to 60 percent of the tissues analyzed, exhibited a heterogeneous expression depending of the biomarker; for WT1, P16 and BRCA1, where both positive and negative tumor areas coexist. The discrimination between positive and negative cases for WT1 and P16 is crucial for a differential diagnosis between HGSOC and other types of ovarian cancer. Furthermore, negative staining for BRCA1 is highly indicative of homologous recombination deficiency (HDR) status and therefore useful in stratifying patients who respond to PARP inhibitors from those that do not. For those reasons, IHC analysis made using the entire tissue sections, as done in this study, should be the proper method to characterize HGSOCs and accurately detect tumor heterogeneity, while the evaluation of few representative spots on tissue microarray could lead to an underestimation of positive cases. In this study, staining pattern was significantly associated with OS only for BRCA1 expression in ovarian tumour sites, but not in the peritoneal implants. This discrepancy can be related to the significant decrease in BRCA1 H-score values that we detected in peritoneal implants compared to both ovaries. High grade serous ovarian cancer is characterized by high level of copy number variations with frequent loss of heterozygosis (LOH) and gene deletion. Therefore, we can only hypothesize that during tumor evolution, late stage dissemination of tumor cells on peritoneal cavity can be related to a clonal selection with loss of BRCA1 alleles at least in some patients. This could also partially explain why therapy with PARPs inhibitors is more efficient in some cases, but not in others due to clonal heterogeneity. It's worth to mention that the major difference in OS was

detected between patients with BRCA1 homogenous staining (likely HR proficient) and patients with negative expression (likely HR deficient). For stochastic and heterogeneous patterns, homologous recombination proficiency is clearly undeterminable by means of a simple IHC staining. In those cases, mutational analysis on BRCA1 gene and other genes involved in DNA-repair mechanisms is the elective method to further stratify patients with proficient or deficient HR system.

Another biomarker found significantly associated with survival in our cohort was Ki67. From our results, it was significantly more expressed in patients who didn't progress after primary chemotherapy and its high expression was also associated with longer PFS. This is consistent with the result obtained by Feng et al.[145] and by Chen at al. [146] where women with Ki67 indices greater than respectively 50% and 40% had a longer PFS compared to women with lower Ki67 index ($P = 0.021$ and $P < 0.0001$ respectively). The main agents used in first line treatment of HGSOC, carboplatin and paclitaxel, preferentially kill highly proliferative cells; therefore, tumors with low rate of proliferation might survive from chemotherapy, contributing to a negative outcome. Immunostaining is a cost-effective approach in clinical practice and our data clearly confirm the usefulness of Ki67 as predictive indicator to determine response to first line chemotherapy and identify HGSOC with more aggressive behavior.

Tumor spatial heterogeneity, measured by IHC analysis as staining pattern variation among different anatomical sites, was not associated with OS or PFS, nevertheless the biomarkers used in this study were mainly diagnostic and therefore we cannot exclude that heterogeneity for other selected biomarkers such as driver genes, markers of stemness or epithelial to mesenchymal transition (EMT) could be of more prognostic significance.

5.2 Molecular analyses

In addition to the biomarkers analyzed by immunohistochemistry, other biomarkers retrieved within the HERCULES project were also validated at RNA level. Nanostring platform was used for its high level of multiplexing and the ability to identify prognostic and predictive subgroups of patients. Nevertheless, the custom-made panel used in our study failed to identify specific subgroups of HGSOC since all the 32 samples analyzed shared almost the same expression profile. Among the 71 target transcripts of our panel, suggested by the results of the HERCULES study, seven were significantly associated with clinicopathological parameters. In detail, BEST1, PPP1CC and TFEC were differentially expressed in patients submitted to NACT or PDS while AC083884.8, a lncRNA, and NCKAP5L were found being related with the primary platinum response. The expression of Chemokine (C-X-C motif) ligand 3 (CXCL3), which has been associated with pro-inflammatory reactions [147], was instead significantly higher in patients with no residual tumor after primary

cytoreduction. Since CXCL3 is involved in the recruitment of tumor associated neutrophils (TAF) [148], it's reasonable to think that optimal cytoreduction can favor also the response of immune system. Interestingly, we also found that AKT isoforms can play different roles in AKT signaling and have different impact on patient's outcome. According to our results, the high expression of AKT1 was closely associated with shorter OS while AKT2 high expression conferred significant better outcomes. Our data are in line with previous results of our group in breast cancers, where the three highly homologous AKT isoforms (i.e., AKT1, AKT2, and AKT3) were shown to play different or even functional opposing roles in breast cancer patients [149]. In agreement even in Breast cancer AKT1 was related to shorter survival [149]. Our findings are also in agreement with Petrik et al [150], who found in a mouse model of HGSOC that the selective inhibition of AKT2 isoform resulted in significant decrement of OS while the inhibition AKT1 led to more favorable outcomes. To support those results, we also found that AKT2 was notably higher in patients with FIGO stage III compared to stage IV and lower levels of AKT2 were highly indicative of shorter PFS. The evaluation of AKT isoforms expression is clinically important also in light of the findings of Bowtell et al [59] for the synergy between CCNE1 amplification and AKT2 expression. According to their results, the high expression of AKT2 in combination with CCNE1 amplification should lead to tumor outgrowth and clonogenic colony formation. Therefore, in these tumors the combinatorial inhibition of AKT2 and CCNE1 could constitute important therapeutic targets.

In this study, Nanostring demonstrated its great advantage for its multiplexing capability. Nevertheless, our results performed on matched samples fixed in formalin and Bouin's solution showed how pre-analytical procedures and in particular fixation can lead to analytical concerns. We analyzed 8 matched primary tumors of our cohort on Nanostring using the same custom-made panel previously described. Because of the different pre-analytical conditions we have also validated Nanostring results by ddPCR and conventional real time PCR. The analysis with nSolver returned comparable levels of expression between formalin and Bouin's samples after correcting p-value for multiple comparisons, but the amount of RNA in six transcripts were significantly different without p-value correction. Moreover, among the 71 transcripts analyzed, only eight were significantly correlated in the two fixatives. The comparable level of expression in formalin and Bouin's samples is in disagreement with the results we obtained on ddPCR and RT-qPCR. In these platforms, the RNA expression in Bouin's samples was constantly lower compared to formalin and no correlation between the two fixatives were found for any of the targets analyzed. Data in literature report on a higher degradation level in RNA extracts obtained by Bouin's fixed samples in comparison to formalin [83, 116, 151]. The analyses by Nanodrop and Agilent BioAnalyzer, agreed with previous results, showing that Bouin's samples have significant lower RNA quality and higher level of fragmentation

compared to formalin, as RNA fragments between 60 and 300 nucleotides were significantly less represented in Bouin's specimens. Also our results on reverse transcription efficiency showed that in Bouin's samples the amount of cDNA was significantly lower if compared to formalin. In our analysis we choose to validate, by ddPCR and real-time the expression levels found by Nanostring of one target gene that resulted differently expressed in formalin and Bouin's samples (KLF16) and one target gene that was similarly expressed in the two fixatives (AKT1). Our results by PCR based methods showed that the amounts of transcripts in the two fixatives were not comparable after normalization with two housekeeping genes (GAPDH, ACTB), both by real-time PCR and ddPCR. That finding was even more evident for KLF16, which has very low expression level, in HGSOC. Therefore, variation in its expression cannot be mirrored by RT-PCR, especially real-time, because of the Monte Carlo effect [152] and normalization by the use of well-expressed HSK genes could be a matter of discussion. Overall, ddPCR in our experiments resulted more sensitive in analyzing RNA expression in high degraded samples. Its high resilience to PCR inhibitors has been well reported in literature [133] and this can explain the better performance than real-time in our study. By comparing raw data, ddPCR and qPCR resulted to have a good level of correlation in both fixatives, showing in Bouin's samples a lower deviation from the linear model and a tighter confidence interval compared to formalin.

Our results highlight that one of the main factors accounting for the discrepancies forum between Nanostring and PCR-based methods in formalin and Bouin's material is the reverse-transcription step, which is absent in Nanostring hybridization. As shown in other studies [153, 154], the fragmentation and the modification of nucleic acids caused by fixation procedures can impede processing steps like the reverse transcription of RNA to cDNA. In addition, the effect can be more severe in Bouin's tissues since they are more fragmented, resulting in possible inhibitory effect during amplification. Therefore, we can speculate that, on Nanostring platform, the higher fragmentation in Bouin's material is balanced by the higher chemical modification of formalin tissues, resulting in comparable gene expression levels between the two fixatives, while, in ddPCR and RT-qPCR, the presence of a reverse-transcription step inhibits to a major extent Bouin's samples, rendering the amount of transcripts not comparable. We acknowledge that Bouin's fixative has a high percentage of formalin, but no data are available at present on the modification rate of adenine residues in Bouin's-fixed nucleic acids. Given the composition of Bouin's fixative, it is likely that the activity of formalin, including its ability to modify adenine residues by CH_2OH addition, could be inhibited by the low pH due to the presence of picric acid [82]. In Bouin's solution, indeed, the effects of formalin and picric and acetic acids balance each other: (i) Formalin fixes cytoplasm, hardens tissues, and prevents paraffin penetration; (ii) picric acid leaves tissue soft and coagulates cytoplasm,

compensating for most the unduly effects of formalin; (iii) the tissue shrinking effect of picric acid is compensated by acetic acid [115, 155].
As consequence, Nanostring results could not be properly compared to those obtained by ddPCR and qRT-PCR, neither after a proper normalization

To further investigate on the impact of the fixatives in RNA analyses, we also analyzed seven miRNA targets in 30 matched formalin/Bouin's samples, by means of ddPCR and RT-qPCR. Micro RNA are single-stranded non-coding RNAs comprised of 18 to 24 nucleotides that have gained more and more importance in clinical research also for their reported resistance to fixed and paraffin embedding procedures. Similar to mRNA analyses, our results indicate that microRNAs from Bouin's-fixed tissues have higher fragmentation compared to formalin; nevertheless, contrary to what detected on mRNA analysis, the effect of RNA degradation in formalin and Bouin's samples was evident only in several targets while in other both ddPCR and RT-qPCR displayed comparable level of expression, supporting for the higher resistance of microRNAs to fixation procedures respect to messenger RNAs. Overall, a good level of correlation was found between ddPCR and RT-qPCR in both fixatives, although R-square values in formalin were generally lower if compared to Bouin's material. This was possibly due to lower level of nitrogenous bases modification in Bouin's samples as we hypothesized in the case of mRNA. Globally, our results show that by choosing the proper reference miRNAs with a calibrator that includes both formalin- and Bouin's-fixed samples, it is possible to eliminate differences in the expression profiles of miRNAs and analyze in the same cohort samples processed with both fixatives. Thus, miRNA expression studies can be reliably performed by real-time PCR or, better, by ddPCR in routinely obtained pathological material fixed in formalin or Bouin's solution, considering proper data normalization in order to correct sample-to-sample degradation.

Another RT-free, hybridization method used in this study was RNascope. The latter was used as an alternative method to validate in situ HLA-B, WFDC2, CCNC and CCNE1 biomarkers in HGSOC. The method allows detecting tumor heterogeneity because it is in situ and preserves tissue morphology. Among the four targets analyzed, only CCNE1 displayed no significant association with clinicopathological variables although its role as oncogene in HGSOC [156]. The other markers were associated with survival, response to therapy or histological features.
Along with HLA-A and HLA-C, HLA-B gene encodes the major histocompatibility molecules of class I whose function is to present antigens to the immune system, thus regulating immune surveillance. The lower expression of this marker in our samples was significantly associated with late stage disease and shorter overall survival. These results are in agreement with those reported by

other groups in ovarian and lung cancer [157, 158], where down-regulation or loss of heterozygosity in HLA-class I molecules during late stage diseases seem to reflect the escape of tumor cells from immune recognition and destruction. Therefore, the selection of tumor clones with low expression of HLA-B can in turn favor tumor growth and progression.

Also Cyclin C (CCNC) was positively associated with patient's outcome, as its higher expression was related to better overall survival and response to primary platinum therapy. This cyclin acts as a regulator of RNA polymerase II and several studies have also indicated its possible role in mitochondrial stress mediated apoptosis and Notch signaling pathway [159]. Since Notch pathway has been found frequently altered in HGSOC [159] and CCNC acts as its indirect inhibitor, it's reasonable to think that its down expression can lead to neoplastic growth and favor cancer progression.

Lastly, WAP Four-Disulfide Core Domain 2 exhibited higher expression in Classic tumors compared to SET tumors in our cohort. WFDC2 is known to be highly expressed in ovarian cancer cells, but its role in the development of HGSOC is still controversial. A recent work by Chen and colleagues [160] have shown how overexpression of WFDC2 can contribute to epithelial to mesenchymal transition and favor tumor invasion and metastasis. Accordingly, Classic tumors which overexpressed WFDC2 may have higher metastatic potential. These results are in agreement with data obtained by biomechanical measurement using atomic force microscopy where classic tumors (papillary and micropapillary patterns) had Gaussian peaks at lower level of stiffness compared to the other patterns, suggesting a pro-metastatic behavior.

Overall, RNAscope signal was assessable for all the RNA targets analyzed, nevertheless, we found marked reductions in signals across the different targets, such as for CCNC and CCNE1, and especially across the different spots present in each TMA blocks. These findings were also reported by another group that found an inverse correlation between RNAscope signal and blocks age and marked variability among tissues blocks fixed in different institutions [161]. This raises the question of RNA stability and consequent reliability of RNAscope analyses, especially in light of our results obtained on RNA expression on Nanostring, ddPCR and real-time PCR. Pre-analytical factors could result in biased data and lead to inappropriate conclusions about RNA expression in clinical and research FFPE specimens.

6 CONCLUSIONS

In this thesis, we validated new candidate biomarkers in association to the classical pathological features in a cohort of 294 HGSOC patients. Furthermore, we analyzed the impact of fixation on the reliability of molecular analyses. According to our finding we can conclude that:

- FIGO stage, optimal cytoreduction, CA125 and LDH levels are consolidated parameters for determining patient's prognosis.
- Patients treated with neoadjuvant chemotherapy (NACT) in our cohort have shorter overall survival.
- Detailed morphological analyses of HGSOC tumors and stratification in SET and Classic groups can have predictive and prognostic values since SET features are related to better outcome. Moreover, micropapillary pattern could represent a more aggressive entity in the spectrum of HGSOCs.
- With respect to morphological and immunophenotypical characterization, the analysis made on the entire slide in comparison to TMA resulted to be paramount for highly heterogeneous tumors, such as HGSOC.
- AFM can be used in FFPE tissues to characterize their biomechanical properties and give complementary information on tumor behavior.
- Ki67 and BRCA1 stains are cost effective methods that can be used as predictive biomarkers of response to first line chemotherapy and overall survival in HGSOC patients.
- AKT isoforms can play different roles in HGSOC prognosis, tumor progression and response to therapy.
- High expression of HLA-B and CCNC are prognostic as they are indicative of longer overall survival
- Fixation can have a deep impact on molecular analyses, especially in RNA expression. Tissues with highly fragmented RNA such those fixed in Bouin's can lead to analytical bias in both ddPCR, RT-qPCR, Nanostring and RNAscope technologies.
- A careful selection of samples with proper nucleic acids quality and integrity is of paramount importance before starting any molecular analyses. Also in that case, to minimize the effect of sample to sample variability a proper sample size should be used.
- Bouin's fixed samples are not recommended for mRNA expression analyses, especially for low expressed targets, because of their high level of nucleic acids fragmentation.

- MicroRNAs, giving their length, are more resistant to fixation procedures and can be used for RNA expression analyses in both formalin and Bouin's tissues after a proper method of normalization.

7 BIBLIOGRAPHY

References

1. Lheureux, S., M. Braunstein, and A.M. Oza, *Epithelial ovarian cancer: Evolution of management in the era of precision medicine.* CA Cancer J Clin, 2019. **69**(4): p. 280-304.
2. Reid, B.M., J.B. Permuth, and T.A. Sellers, *Epidemiology of ovarian cancer: a review.* Cancer Biol Med, 2017. **14**(1): p. 9-32.
3. Bray, F., et al., *Global cancer statistics 2018: GLOBOCAN estimates of incidence and mortality worldwide for 36 cancers in 185 countries.* CA Cancer J Clin, 2018. **68**(6): p. 394-424.
4. Coburn, S.B., et al., *International patterns and trends in ovarian cancer incidence, overall and by histologic subtype.* Int J Cancer, 2017. **140**(11): p. 2451-2460.
5. Chen, V.W., et al., *Pathology and classification of ovarian tumors.* Cancer, 2003. **97**(10 Suppl): p. 2631-42.
6. Sankaranarayanan, R. and J. Ferlay, *Worldwide burden of gynaecological cancer: the size of the problem.* Best Pract Res Clin Obstet Gynaecol, 2006. **20**(2): p. 207-25.
7. Meinhold-Heerlein, I., et al., *The new WHO classification of ovarian, fallopian tube, and primary peritoneal cancer and its clinical implications.* Arch Gynecol Obstet, 2016. **293**(4): p. 695-700.
8. Singh, N., W.G. McCluggage, and C.B. Gilks, *High-grade serous carcinoma of tubo-ovarian origin: recent developments.* Histopathology, 2017. **71**(3): p. 339-356.
9. Berek, J.S., et al., *Cancer of the ovary, fallopian tube, and peritoneum.* Int J Gynaecol Obstet, 2018. **143 Suppl 2**: p. 59-78.
10. Young, R.C., et al., *Adjuvant therapy in stage I and stage II epithelial ovarian cancer. Results of two prospective randomized trials.* N Engl J Med, 1990. **322**(15): p. 1021-7.
11. Pennington, K.P. and E.M. Swisher, *Hereditary ovarian cancer: beyond the usual suspects.* Gynecol Oncol, 2012. **124**(2): p. 347-53.
12. Castilla, L.H., et al., *Mutations in the BRCA1 gene in families with early-onset breast and ovarian cancer.* Nat Genet, 1994. **8**(4): p. 387-91.
13. Moslehi, R., et al., *BRCA1 and BRCA2 mutation analysis of 208 Ashkenazi Jewish women with ovarian cancer.* Am J Hum Genet, 2000. **66**(4): p. 1259-72.
14. Alsop, K., et al., *BRCA mutation frequency and patterns of treatment response in BRCA mutation-positive women with ovarian cancer: a report from the Australian Ovarian Cancer Study Group.* J Clin Oncol, 2012. **30**(21): p. 2654-63.
15. Kauff, N.D., et al., *Risk-reducing salpingo-oophorectomy in women with a BRCA1 or BRCA2 mutation.* N Engl J Med, 2002. **346**(21): p. 1609-15.
16. Rebbeck, T.R., et al., *Prophylactic oophorectomy in carriers of BRCA1 or BRCA2 mutations.* N Engl J Med, 2002. **346**(21): p. 1616-22.
17. Falconer, H., et al., *Ovarian cancer risk after salpingectomy: a nationwide population-based study.* J Natl Cancer Inst, 2015. **107**(2).
18. Buys, S.S., et al., *Effect of screening on ovarian cancer mortality: the Prostate, Lung, Colorectal and Ovarian (PLCO) Cancer Screening Randomized Controlled Trial.* JAMA, 2011. **305**(22): p. 2295-303.
19. Jacobs, I.J., et al., *Ovarian cancer screening and mortality in the UK Collaborative Trial of Ovarian Cancer Screening (UKCTOCS): a randomised controlled trial.* Lancet, 2016. **387**(10022): p. 945-956.

20. Wu, L., et al., *Diagnostic value of serum human epididymis protein 4 (HE4) in ovarian carcinoma: a systematic review and meta-analysis.* Int J Gynecol Cancer, 2012. **22**(7): p. 1106-12.
21. Norquist, B.M., et al., *Inherited Mutations in Women With Ovarian Carcinoma.* JAMA Oncol, 2016. **2**(4): p. 482-90.
22. Prakash, R., et al., *Homologous recombination and human health: the roles of BRCA1, BRCA2, and associated proteins.* Cold Spring Harb Perspect Biol, 2015. **7**(4): p. a016600.
23. Penninkilampi, R. and G.D. Eslick, *Perineal Talc Use and Ovarian Cancer: A Systematic Review and Meta-Analysis.* Epidemiology, 2018. **29**(1): p. 41-49.
24. Mutch, D.G. and J. Prat, *2014 FIGO staging for ovarian, fallopian tube and peritoneal cancer.* Gynecol Oncol, 2014. **133**(3): p. 401-4.
25. Bristow, R.E., et al., *Survival effect of maximal cytoreductive surgery for advanced ovarian carcinoma during the platinum era: a meta-analysis.* J Clin Oncol, 2002. **20**(5): p. 1248-59.
26. Harter, P., et al., *A Randomized Trial of Lymphadenectomy in Patients with Advanced Ovarian Neoplasms.* N Engl J Med, 2019. **380**(9): p. 822-832.
27. Kehoe, S., et al., *Primary chemotherapy versus primary surgery for newly diagnosed advanced ovarian cancer (CHORUS): an open-label, randomised, controlled, non-inferiority trial.* Lancet, 2015. **386**(9990): p. 249-57.
28. Vergote, I., et al., *Neoadjuvant chemotherapy or primary surgery in stage IIIC or IV ovarian cancer.* N Engl J Med, 2010. **363**(10): p. 943-53.
29. Karam, A., et al., *Fifth Ovarian Cancer Consensus Conference of the Gynecologic Cancer InterGroup: first-line interventions.* Ann Oncol, 2017. **28**(4): p. 711-717.
30. van Driel, W.J., et al., *Hyperthermic Intraperitoneal Chemotherapy in Ovarian Cancer.* N Engl J Med, 2018. **378**(3): p. 230-240.
31. Perren, T.J., et al., *A phase 3 trial of bevacizumab in ovarian cancer.* N Engl J Med, 2011. **365**(26): p. 2484-96.
32. Konstantinopoulos, P.A., et al., *Homologous Recombination Deficiency: Exploiting the Fundamental Vulnerability of Ovarian Cancer.* Cancer Discov, 2015. **5**(11): p. 1137-54.
33. Moore, K., et al., *Maintenance Olaparib in Patients with Newly Diagnosed Advanced Ovarian Cancer.* N Engl J Med, 2018. **379**(26): p. 2495-2505.
34. Ledermann, J., et al., *Olaparib maintenance therapy in platinum-sensitive relapsed ovarian cancer.* N Engl J Med, 2012. **366**(15): p. 1382-92.
35. Kim, G., et al., *FDA Approval Summary: Olaparib Monotherapy in Patients with Deleterious Germline BRCA-Mutated Advanced Ovarian Cancer Treated with Three or More Lines of Chemotherapy.* Clin Cancer Res, 2015. **21**(19): p. 4257-61.
36. Gockley, A., et al., *Outcomes of secondary cytoreductive surgery for patients with platinum-sensitive recurrent ovarian cancer.* Am J Obstet Gynecol, 2019.
37. Matulonis, U.A., et al., *Ovarian cancer.* Nat Rev Dis Primers, 2016. **2**: p. 16061.
38. Fathalla, M.F., *Incessant ovulation--a factor in ovarian neoplasia?* Lancet, 1971. **2**(7716): p. 163.
39. Labidi-Galy, S.I., et al., *High grade serous ovarian carcinomas originate in the fallopian tube.* Nat Commun, 2017. **8**(1): p. 1093.
40. Klotz, D.M. and P. Wimberger, *Cells of origin of ovarian cancer: ovarian surface epithelium or fallopian tube?* Arch Gynecol Obstet, 2017. **296**(6): p. 1055-1062.
41. Gwin, K., R. Wilcox, and A. Montag, *Insights into selected genetic diseases affecting the female reproductive tract and their implication for pathologic evaluation of gynecologic specimens.* Arch Pathol Lab Med, 2009. **133**(7): p. 1041-52.
42. Kurman, R.J. and M. Shih Ie, *Molecular pathogenesis and extraovarian origin of epithelial ovarian cancer--shifting the paradigm.* Hum Pathol, 2011. **42**(7): p. 918-31.
43. Kurman, R.J. and M. Shih Ie, *The Dualistic Model of Ovarian Carcinogenesis: Revisited, Revised, and Expanded.* Am J Pathol, 2016. **186**(4): p. 733-47.

44. Medeiros, F., et al., *The tubal fimbria is a preferred site for early adenocarcinoma in women with familial ovarian cancer syndrome.* American Journal of Surgical Pathology, 2006. **30**(2): p. 230-236.
45. Meserve, E.E.K., J. Brouwer, and C.P. Crum, *Serous tubal intraepithelial neoplasia: the concept and its application.* Modern Pathology, 2017. **30**(5): p. 710-721.
46. Bowtell, D.D.L., *The genesis and evolution of high-grade serous ovarian cancer.* Nature Reviews Cancer, 2010. **10**(11): p. 803-808.
47. Reade, C.J., et al., *The fallopian tube as the origin of high grade serous ovarian cancer: review of a paradigm shift.* J Obstet Gynaecol Can, 2014. **36**(2): p. 133-140.
48. Vang, R., et al., *Validation of an algorithm for the diagnosis of serous tubal intraepithelial carcinoma.* Int J Gynecol Pathol, 2012. **31**(3): p. 243-53.
49. Prat, J., E. D'Angelo, and I. Espinosa, *Ovarian carcinomas: at least five different diseases with distinct histological features and molecular genetics.* Human Pathology, 2018. **80**: p. 11-27.
50. Gilks, C.B., et al., *Tumor cell type can be reproducibly diagnosed and is of independent prognostic significance in patients with maximally debulked ovarian carcinoma.* Hum Pathol, 2008. **39**(8): p. 1239-51.
51. Soslow, R.A., et al., *Morphologic patterns associated with BRCA1 and BRCA2 genotype in ovarian carcinoma.* Mod Pathol, 2012. **25**(4): p. 625-36.
52. Ritterhouse, L.L., et al., *Morphologic correlates of molecular alterations in extrauterine Mullerian carcinomas.* Mod Pathol, 2016. **29**(8): p. 893-903.
53. Howitt, B.E., et al., *Evidence for a dualistic model of high-grade serous carcinoma: BRCA mutation status, histology, and tubal intraepithelial carcinoma.* Am J Surg Pathol, 2015. **39**(3): p. 287-93.
54. Kobel, M., et al., *Ovarian carcinoma histotype determination is highly reproducible, and is improved through the use of immunohistochemistry.* Histopathology, 2014. **64**(7): p. 1004-13.
55. Cancer Genome Atlas Research, N., *Integrated genomic analyses of ovarian carcinoma.* Nature, 2011. **474**(7353): p. 609-15.
56. Kuhn, E., et al., *TP53 mutations in serous tubal intraepithelial carcinoma and concurrent pelvic high-grade serous carcinoma-evidence supporting the clonal relationship of the two lesions.* Journal of Pathology, 2012. **226**(3): p. 421-426.
57. Kondrashova, O. and C.L. Scott, *Clarifying the role of EMSY in DNA repair in ovarian cancer.* Cancer, 2019. **125**(16): p. 2720-2724.
58. Hollis, R.L., et al., *High EMSY expression defines a BRCA-like subgroup of high-grade serous ovarian carcinoma with prolonged survival and hypersensitivity to platinum.* Cancer, 2019. **125**(16): p. 2772-2781.
59. Au-Yeung, G., et al., *Selective Targeting of Cyclin E1-Amplified High-Grade Serous Ovarian Cancer by Cyclin-Dependent Kinase 2 and AKT Inhibition.* Clin Cancer Res, 2017. **23**(7): p. 1862-1874.
60. Kuhn, E., et al., *CCNE1 amplification and centrosome number abnormality in serous tubal intraepithelial carcinoma: further evidence supporting its role as a precursor of ovarian high-grade serous carcinoma.* Mod Pathol, 2016. **29**(10): p. 1254-61.
61. Wang, Y.K., et al., *Genomic consequences of aberrant DNA repair mechanisms stratify ovarian cancer histotypes.* Nat Genet, 2017. **49**(6): p. 856-865.
62. Tothill, R.W., et al., *Novel molecular subtypes of serous and endometrioid ovarian cancer linked to clinical outcome.* Clin Cancer Res, 2008. **14**(16): p. 5198-208.
63. Wang, C., et al., *Pooled Clustering of High-Grade Serous Ovarian Cancer Gene Expression Leads to Novel Consensus Subtypes Associated with Survival and Surgical Outcomes.* Clinical Cancer Research, 2017. **23**(15): p. 4077-4085.
64. Macintyre, G., et al., *Copy number signatures and mutational processes in ovarian carcinoma.* Nat Genet, 2018. **50**(9): p. 1262-1270.

65. Bonin, S. and G. Stanta, *Pre-analytics and tumor heterogeneity.* N Biotechnol, 2019. **55**: p. 30-35.
66. Stanta, G. and S. Bonin, *A Practical Approach to Tumor Heterogeneity in Clinical Research and Diagnostics.* Pathobiology, 2018. **85**(1-2): p. 7-17.
67. Swanton, C., *Intratumor Heterogeneity: Evolution through Space and Time.* Cancer Research, 2012. **72**(19): p. 4875-4882.
68. Turajlic, S., et al., *Resolving genetic heterogeneity in cancer.* Nat Rev Genet, 2019. **20**(7): p. 404-416.
69. McQuerry, J.A., et al., *Mechanisms and clinical implications of tumor heterogeneity and convergence on recurrent phenotypes.* J Mol Med (Berl), 2017. **95**(11): p. 1167-1178.
70. Stanta, G. and S. Bonin, *Overview on Clinical Relevance of Intra-Tumor Heterogeneity.* Front Med (Lausanne), 2018. **5**: p. 85.
71. McPherson, A., et al., *Divergent modes of clonal spread and intraperitoneal mixing in high-grade serous ovarian cancer.* Nat Genet, 2016. **48**(7): p. 758-67.
72. Bashashati, A., et al., *Distinct evolutionary trajectories of primary high-grade serous ovarian cancers revealed through spatial mutational profiling.* J Pathol, 2013. **231**(1): p. 21-34.
73. Castellarin, M., et al., *Clonal evolution of high-grade serous ovarian carcinoma from primary to recurrent disease.* J Pathol, 2013. **229**(4): p. 515-24.
74. Lambrechts, S., et al., *Genetic heterogeneity after first-line chemotherapy in high-grade serous ovarian cancer.* Eur J Cancer, 2016. **53**: p. 51-64.
75. Jimenez-Sanchez, A., et al., *Heterogeneous Tumor-Immune Microenvironments among Differentially Growing Metastases in an Ovarian Cancer Patient.* Cell, 2017. **170**(5): p. 927-+.
76. Zhang, A.W., et al., *Interfaces of Malignant and Immunologic Clonal Dynamics in Ovarian Cancer.* Cell, 2018. **173**(7): p. 1755-1769 e22.
77. Iwase, H., et al., *Clinical features of long-term survivors of recurrent epithelial ovarian cancer.* Int J Clin Oncol, 2015. **20**(1): p. 143-9.
78. Hamilton, C.A., et al., *Clinicopathologic characteristics associated with long-term survival in advanced epithelial ovarian cancer: an NRG Oncology/Gynecologic Oncology Group ancillary data study.* Gynecol Oncol, 2018. **148**(2): p. 275-280.
79. Hilal, Z., et al., *What Characterizes Long-term Survivors of Recurrent Ovarian Cancer? Case Report and Review of the Literature.* Anticancer Research, 2016. **36**(10): p. 5365-5371.
80. Gonzalez, V.D., et al., *Commonly Occurring Cell Subsets in High-Grade Serous Ovarian Tumors Identified by Single-Cell Mass Cytometry.* Cell Rep, 2018. **22**(7): p. 1875-1888.
81. *HERCULES project*. Available from: http://www.project-hercules.eu/.
82. Howat, W.J. and B.A. Wilson, *Tissue fixation and the effect of molecular fixatives on downstream staining procedures.* Methods, 2014. **70**(1): p. 12-9.
83. Tanca, A., et al., *Evaluation of the suitability of archival Bouin-fixed paraffin-embedded tissue specimens to proteomic investigation.* Electrophoresis, 2012. **33**(9-10): p. 1375-84.
84. Farragher, S.M., et al., *RNA expression analysis from formalin fixed paraffin embedded tissues.* Histochem Cell Biol, 2008. **130**(3): p. 435-45.
85. Kokkat, T.J., et al., *Archived Formalin-Fixed Paraffin-Embedded (FFPE) Blocks: A Valuable Underexploited Resource for Extraction of DNA, RNA, and Protein.* Biopreservation and Biobanking, 2013. **11**(2): p. 101-106.
86. Gaffney, E.F., et al., *Factors that drive the increasing use of FFPE tissue in basic and translational cancer research.* Biotechnic & Histochemistry, 2018. **93**(5): p. 373-386.
87. Xie, R., et al., *Factors influencing the degradation of archival formalin-fixed paraffin-embedded tissue sections.* J Histochem Cytochem, 2011. **59**(4): p. 356-65.
88. Thompson, S.M., et al., *Impact of pre-analytical factors on the proteomic analysis of formalin-fixed paraffin-embedded tissue.* Proteomics Clinical Applications, 2013. **7**(3-4): p. 241-251.

89. Shi, S.R., M.E. Key, and K.L. Kalra, *Antigen Retrieval in Formalin-Fixed, Paraffin-Embedded Tissues - an Enhancement Method for Immunohistochemical Staining Based on Microwave-Oven Heating of Tissue-Sections.* Journal of Histochemistry & Cytochemistry, 1991. **39**(6): p. 741-748.
90. Stumptner, C., et al., *The impact of crosslinking and non-crosslinking fixatives on antigen retrieval and immunohistochemistry.* New Biotechnology, 2019. **52**: p. 69-83.
91. Hoffman, E.A., et al., *Formaldehyde crosslinking: a tool for the study of chromatin complexes.* J Biol Chem, 2015. **290**(44): p. 26404-11.
92. Thavarajah, R., et al., *Chemical and physical basics of routine formaldehyde fixation.* J Oral Maxillofac Pathol, 2012. **16**(3): p. 400-5.
93. Masuda, N., et al., *Analysis of chemical modification of RNA from formalin-fixed samples and optimization of molecular biology applications for such samples.* Nucleic Acids Research, 1999. **27**(22): p. 4436-4443.
94. Groelz, D., et al., *Impact of storage conditions on the quality of nucleic acids in paraffin embedded tissues.* PLoS One, 2018. **13**(9): p. e0203608.
95. Riegman, P.H.J., et al., *How standardization of the pre-analytical phase of both research and diagnostic biomaterials can increase reproducibility of biomedical research and diagnostics.* New Biotechnology, 2019. **53**: p. 35-40.
96. Snead, D.R., et al., *Methodology of immunohistological detection of oestrogen receptor in human breast carcinoma in formalin-fixed, paraffin-embedded tissue: a comparison with frozen section methodology.* Histopathology, 1993. **23**(3): p. 233-8.
97. Beard, R.E., et al., *Gene Expression Profiling using Nanostring Digital RNA Counting to Identify Potential Target Antigens for Melanoma Immunotherapy.* Clinical Cancer Research, 2013. **19**(18): p. 4941-4950.
98. Chatterjee, A., et al., *A cross comparison of technologies for the detection of microRNAs in clinical FFPE samples of hepatoblastoma patients (vol 5, 10438, 2015).* Scientific Reports, 2015. **5**.
99. Zhu, J., et al., *Evaluation of frozen tissue-derived prognostic gene expression signatures in FFPE colorectal cancer samples.* Scientific Reports, 2016. **6**.
100. Dahl, M., et al., *Enzyme-free digital counting of endogenous circular RNA molecules in B-cell malignancies.* Laboratory Investigation, 2018. **98**(12): p. 1657-1669.
101. Reis, P.P., et al., *mRNA transcript quantification in archival samples using multiplexed, color-coded probes.* Bmc Biotechnology, 2011. **11**.
102. Tsang, H.F., et al., *NanoString, a novel digital color-coded barcode technology: current and future applications in molecular diagnostics.* Expert Review of Molecular Diagnostics, 2017. **17**(1): p. 95-103.
103. Rouzier, R., et al., *Denaturing fixatives are compatible with the NanoString nCounter((R)) platform and the Prosigna((R)) assay.* N Biotechnol, 2017. **36**: p. 37-41.
104. Veldman-Jones, M.H., et al., *Evaluating Robustness and Sensitivity of the NanoString Technologies nCounter Platform to Enable Multiplexed Gene Expression Analysis of Clinical Samples.* Cancer Research, 2015. **75**(13): p. 2587-2593.
105. Chen, P., et al., *Identification of Prognostic Groups in High-Grade Serous Ovarian Cancer Treated with Platinum-Taxane Chemotherapy.* Cancer Research, 2015. **75**(15): p. 2987-2998.
106. Sotiriou, C. and M.J. Piccart, *Taking gene-expression profiling to the clinic: when will molecular signatures become relevant to patient care?* Nat Rev Cancer, 2007. **7**(7): p. 545-53.
107. Mahmood, R. and I. Mason, *In-situ hybridization of radioactive riboprobes to RNA in tissue sections.* Methods Mol Biol, 2008. **461**: p. 675-86.
108. Wirtz, D., K. Konstantopoulos, and P.C. Searson, *The physics of cancer: the role of physical interactions and mechanical forces in metastasis.* Nature Reviews Cancer, 2011. **11**(7): p. 512-522.

109. Goetz, J.G., et al., *Biomechanical Remodeling of the Microenvironment by Stromal Caveolin-1 Favors Tumor Invasion and Metastasis.* Cell, 2011. **146**(1): p. 148-163.
110. Paszek, M.J. and V.M. Weaver, *The tension mounts: Mechanics meets morphogenesis and malignancy.* Journal of Mammary Gland Biology and Neoplasia, 2004. **9**(4): p. 325-342.
111. Lekka, M., et al., *Elasticity of normal and cancerous human bladder cells studied by scanning force microscopy.* European Biophysics Journal with Biophysics Letters, 1999. **28**(4): p. 312-316.
112. Lekka, M., et al., *Cancer cell recognition - Mechanical phenotype.* Micron, 2012. **43**(12): p. 1259-1266.
113. Plodinec, M., et al., *The nanomechanical signature of breast cancer.* Nat Nanotechnol, 2012. **7**(11): p. 757-65.
114. Tanca, A., et al., *Evaluation of the suitability of archival Bouin-fixed paraffin-embedded tissue specimens to proteomic investigation.* Electrophoresis, 2012. **33**(9-10): p. 1375-1384.
115. Ortiz-Hidalgo, C., *Pol Andre Bouin, MD (1870-1962). Bouin's fixative and other contributions to medicine.* Arch Pathol Lab Med, 1992. **116**(8): p. 882-4.
116. Bonin, S., et al., *DNA and RNA obtained from Bouin's fixed tissues.* Journal of Clinical Pathology, 2005. **58**(3): p. 313-316.
117. Saikumar, J., K. Ramachandran, and V.S. Vaidya, *Noninvasive micromarkers.* Clin Chem, 2014. **60**(9): p. 1158-73.
118. Bignotti, E., et al., *Circulating Mirna Landscape Identifies Mir-1246 as Promising Diagnostic Biomarker in High-Grade Serous Ovarian Carcinoma: A Validation across Two Independent Cohorts.* International Journal of Gynecological Cancer, 2017. **27**: p. 265-265.
119. Zhang, S., et al., *Clinically relevant microRNAs in ovarian cancer.* Mol Cancer Res, 2015. **13**(3): p. 393-401.
120. Siebolts, U., et al., *Tissues from routine pathology archives are suitable for microRNA analyses by quantitative PCR.* J Clin Pathol, 2009. **62**(1): p. 84-8.
121. Sanchez, I., et al., *RNA and microRNA Stability in PAXgene-Fixed Paraffin-Embedded Tissue Blocks After Seven Years' Storage.* Am J Clin Pathol, 2018. **149**(6): p. 536-547.
122. Peiro-Chova, L., et al., *High stability of microRNAs in tissue samples of compromised quality.* Virchows Arch, 2013. **463**(6): p. 765-74.
123. Nardon, E., et al., *Higher random oligo concentration improves reverse transcription yield of cDNA from bioptic tissues and quantitative RT-PCR reliability.* Exp Mol Pathol, 2009. **87**(2): p. 146-51.
124. Björkman, J., et al., *Differential amplicons (ΔAmp)-a new molecular method to assess RNA integrity.* Biomol Detect Quantif, 2016. **6**: p. 4-12.
125. Bignotti, E., et al., *Identification of stably expressed reference small non-coding RNAs for microRNA quantification in high-grade serous ovarian carcinoma tissues.* J Cell Mol Med, 2016. **20**(12): p. 2341-2348.
126. Chen, S.F., et al., *Identification of core aberrantly expressed microRNAs in serous ovarian carcinoma.* Oncotarget, 2018. **9**(29): p. 20451-20466.
127. Shi, M., et al., *MicroRNA-200 and microRNA-30 family as prognostic molecular signatures in ovarian cancer: A meta-analysis.* Medicine (Baltimore), 2018. **97**(32): p. e11505.
128. Petrillo, M., et al., *Identification of high-grade serous ovarian cancer miRNA species associated with survival and drug response in patients receiving neoadjuvant chemotherapy: a retrospective longitudinal analysis using matched tumor biopsies.* Ann Oncol, 2016. **27**(4): p. 625-34.
129. Diehl, F. and L.A. Diaz, Jr., *Digital quantification of mutant DNA in cancer patients.* Curr Opin Oncol, 2007. **19**(1): p. 36-42.
130. Vogelstein, B., K. Kinzler, and M. Landau, *An interview with Bert Vogelstein and Kenneth Kinzler.* Clin Chem, 2015. **61**(1): p. 9-20.

131. Basu, A.S., *Digital Assays Part I: Partitioning Statistics and Digital PCR.* SLAS Technol, 2017. **22**(4): p. 369-386.
132. Pinheiro, L. and K.R. Emslie, *Basic Concepts and Validation of Digital PCR Measurements.* Methods Mol Biol, 2018. **1768**: p. 11-24.
133. Racki, N., et al., *Reverse transcriptase droplet digital PCR shows high resilience to PCR inhibitors from plant, soil and water samples.* Plant Methods, 2014. **10**(1): p. 42.
134. Livak, K.J. and T.D. Schmittgen, *Analysis of relative gene expression data using real-time quantitative PCR and the 2(-Delta Delta C(T)) Method.* Methods, 2001. **25**(4): p. 402-8.
135. Yang, Y.L., et al., *Invasive Micropapillary Carcinoma of the Breast: An Update.* Arch Pathol Lab Med, 2016. **140**(8): p. 799-805.
136. Nenutil, R., et al., *Discriminating functional and non-functional p53 in human tumours by p53 and MDM2 immunohistochemistry.* J Pathol, 2005. **207**(3): p. 251-9.
137. Cole, A.J., et al., *Assessing mutant p53 in primary high-grade serous ovarian cancer using immunohistochemistry and massively parallel sequencing.* Sci Rep, 2016. **6**: p. 26191.
138. Roberts, L., et al., *Identification of methods for use of formalin-fixed, paraffin-embedded tissue samples in RNA expression profiling.* (1089-8646 (Electronic)).
139. Webb, P.M. and S.J. Jordan, *Epidemiology of epithelial ovarian cancer.* Best Pract Res Clin Obstet Gynaecol, 2017. **41**: p. 3-14.
140. Stanta, G., S. Bonin, and R. Perin, *RNA extraction from formalin-fixed and paraffin-embedded tissues.* Methods Mol Biol, 1998. **86**: p. 23-6.
141. Lheureux, S., et al., *Epithelial ovarian cancer.* Lancet, 2019. **393**(10177): p. 1240-1253.
142. Torre, L.A., et al., *Ovarian cancer statistics, 2018.* CA Cancer J Clin, 2018. **68**(4): p. 284-296.
143. Malvezzi, M., et al., *Global trends and predictions in ovarian cancer mortality.* Ann Oncol, 2016. **27**(11): p. 2017-2025.
144. Kobel, M., et al., *Biomarker expression in pelvic high-grade serous carcinoma: comparison of ovarian and omental sites.* Int J Gynecol Pathol, 2011. **30**(4): p. 366-71.
145. Feng, Z., et al., *A clinically applicable molecular classification for high-grade serous ovarian cancer based on hormone receptor expression.* Sci Rep, 2016. **6**: p. 25408.
146. Chen, M., et al., *The prognostic value of Ki67 in ovarian high-grade serous carcinoma: an 11-year cohort study of Chinese patients.* Oncotarget, 2017. **8**(64): p. 107877-107885.
147. Susek, K.H., et al., *The Role of CXC Chemokine Receptors 1-4 on Immune Cells in the Tumor Microenvironment.* Front Immunol, 2018. **9**: p. 2159.
148. Hiramatsu, S., et al., *Neutrophils in primary gastric tumors are correlated with neutrophil infiltration in tumor-draining lymph nodes and the systemic inflammatory response.* BMC Immunol, 2018. **19**(1): p. 13.
149. Bonin, S., et al., *PI3K/AKT Signaling in Breast Cancer Molecular Subtyping and Lymph Node Involvement.* Dis Markers, 2019. **2019**: p. 7832376.
150. Linnerth-Petrik, N.M., et al., *Akt isoform specific effects in ovarian cancer progression.* Oncotarget, 2016. **7**(46): p. 74820-74833.
151. Gloghini, A., et al., *RT-PCR analysis of RNA extracted from Bouin-fixed and paraffin-embedded lymphoid tissues.* J Mol Diagn, 2004. **6**(4): p. 290-6.
152. Martino, L., V. Elvira, and F. Louzada, *Effective sample size for importance sampling based on discrepancy measures.* Signal Processing, 2017. **131**: p. 386-401.
153. Kashofer, K., et al., *Quality control of RNA preservation and extraction from paraffin-embedded tissue: implications for RT-PCR and microarray analysis.* PLoS One, 2013. **8**(7): p. e70714.
154. Libus, J. and H. Storchova, *Quantification of cDNA generated by reverse transcription of total RNA provides a simple alternative tool for quantitative RT-PCR normalization.* Biotechniques, 2006. **41**(2): p. 156, 158, 160 passim.

155. Srinivasan, M., D. Sedmak, and S. Jewell, *Effect of fixatives and tissue processing on the content and integrity of nucleic acids.* Am J Pathol, 2002. **161**(6): p. 1961-71.
156. Karst, A.M., et al., *Cyclin E1 deregulation occurs early in secretory cell transformation to promote formation of fallopian tube-derived high-grade serous ovarian cancers.* Cancer Res, 2014. **74**(4): p. 1141-52.
157. Le, Y.S., et al., *Alterations of HLA class I and class II antigen expressions in borderline, invasive and metastatic ovarian cancers.* Exp Mol Med, 2002. **34**(1): p. 18-26.
158. McGranahan, N., et al., *Allele-Specific HLA Loss and Immune Escape in Lung Cancer Evolution.* Cell, 2017. **171**(6): p. 1259-1271 e11.
159. Jezek, J., et al., *Cyclin C: The Story of a Non-Cycling Cyclin.* Biology (Basel), 2019. **8**(1).
160. Chen, Y., et al., *WFDC2 contributes to epithelial-mesenchymal transition (EMT) by activating AKT signaling pathway and regulating MMP-2 expression.* Cancer Manag Res, 2019. **11**: p. 2415-2424.
161. Baena-Del Valle, J.A., et al., *Rapid Loss of RNA Detection by In Situ Hybridization in Stored Tissue Blocks and Preservation by Cold Storage of Unstained Slides.* Am J Clin Pathol, 2017. **148**(5): p. 398-415.

8 ACKNOWLEDGEMENTS

I would like to thank my supervisor Prof. Serena Bonin who gave me the possibility to work in her laboratory and improve a lot as a scientist. I thank also Prof. Giorgio Stanta for his help and support. A special thanks to Dr. Ermanno Nardon for his precious help and for all the advices he gave me during these years; and obviously, a big thank you to my colleagues and friends Eleonora and Domenico for the beautiful time shared together.

Surely, I have to thank Dr. Renzo Barbazza and Paola, to whom I will always be grateful for helping me with my project, for their kind hospitality and for the time spent together.

I would like to thank also: Prof. Vincenzo Canzonieri who provided the samples used in this study; all the people working in the Surgical Pathology Unit of the National Cancer Institute of Aviano for their precious help and support and the HERCULES project which founded my PhD.

Once again, I would like to thank Prof. Loredana Casalis and all the members of the NanoInnovation Lab for their sympathy and their willingness, and in particular Nadira for helping me with AFM measurements.